The Decay of a Microsecond Seniority Isomer in ^{155}Hf

Betool Mohammed Alayed

Department of Physics

This dissertation is submitted for the degree of

Doctor in Philosophy

July 2023

Declaration

I hereby declare that the work described in this dissertation is, except where otherwise stated, entirely my own work and has not been submitted as an exercise for a degree at University of Liverpool.

Betool Mohammed Alayed

July 2023

Acknowledgements

I would like to begin by expressing my gratitude to my supervisor, Prof. Robert Page, for his unwavering guidance and support throughout my journey. I feel incredibly lucky to have had the opportunity to work under his mentor ship. Not only because of his vast knowledge of nuclear physics, but also because of his admirable conduct and demeanor as an academic. I am deeply grateful for the calmness and wisdom that he displayed during the unusual circumstances of the Covid-19 pandemic, which had a positive impact on me.

I would like to acknowledge Qassim University, which represents the Ministry of Education in Saudi Arabia, for their financial support and for giving me the opportunity to travel to numerous locations to carry out my research and share my findings.

I would like to express my gratitude to the Nuclear Physics group members at the University of Liverpool for their positive impact on my time here. Specifically, I want to thank Dr. Muneerah Al-Aqeel for helping me settle into a new environment and develop effective study habits, as well as Dr. Andrew Briscoe, Dr. James Smallcomb and Dr. Daniel Judson for their exceptional support.

I express my sincere gratitude to my parents for their continuous care, love and encouragement to pursue my dreams and happiness. My brothers and sisters, whom I was always eager to meet and spend time with. To my friends and colleagues, who enrich my experiences and with my journey has become more enjoyable; Dr. Sarah Kalantan, Adam McCarter and Ahmed Alharbi.

In a dark period in my life, I made the decision to start studying in an attempt to improve my situation. The process was incredibly challenging and I felt overwhelmed, but I had the support of my dearest friend, Dr. Huda Hakami. She was with me every step of the way,

encouraging me to keep going and reminding me of the joys in life. I am deeply grateful for her compassion and support, and a simple thank you doesn't seem like enough to express my gratitude.

Abstract

A search for an isomeric state has been conducted at Jyväskylä Accelerator Laboratory for the even-odd neutron-deficient nuclide ^{155}Hf. The proton-rich $N = 82$ and 83 isotones below $Z = 72$ have been investigated by McNeill et al., who identified seniority isomers with half-lives in the microsecond range and compared their measured properties with shell-model calculations [1]. Even though systematics would suggest such an isomer exists in ^{155}Hf, they found no evidence for such an isomer.

A 1 mg/cm^2 thick target of ^{102}Pd was bombarded by a beam of $(293-315)$ MeV ^{58}Ni ions to produce the nuclei of interest via a $2p3n$ evaporation channel. The Mass Analysing Recoil Apparatus (MARA) was utilized to separate fusion-evaporation reaction products in flight, after which they were implanted into the Double-Sided Silicon Strip Detector (DSSD) at its focal plane. The DSSD was surrounded by germanium detectors to measure delayed gamma rays. The Recoil Decay Tagging (RDT) method was applied using the alpha decays of its daughter ^{155}Lu. An isomeric state, which decay through gamma emissions has been observed for the first time. It has been assigned a spin and parity of $27/2^-$ based on the $\pi h_{11/2} \otimes \nu f_{7/2}$ configuration, seniority $\upsilon = 3$. Using a gamma-gamma coincidence analysis, the decay level scheme was constructed. The isomeric state has an excitation energy of $2764(4)$ keV and a half-life of $509\ (22)$ ns. The $B(E2)$ value was measured for the 105.4 keV $(27/2^- \longrightarrow 23/2^-)$ isomeric transition and was found to be $0.44(4)$ $W.u.$. The value can be attributed to the known hindrance in $N = 83$ and $N = 82$ isotones which is responsible for the parabolic behaviour of $B(E2)$ values as a function of Z.

Table of contents

List of figures

List of tables

Chapter 1

Introduction

The nucleus is a fascinating system that exhibits phenomena that are not observed in any other natural system known to us. The characteristics of this many-body system are determined by the behaviour of its constituent nucleons, which are fermions that interact strongly. On a microscopic level, very little is known regarding the nucleus. In order to gain a better understanding of the nucleus, it is necessary to consider the interactions between nucleons as a multi-body problem that is still unsolved. Additionally, it would be impossible to perform such calculations on all nuclei except for the lightest ones due to the enormous amount of computing time required. Designing nuclear models that reflect the observed phenomena as accurately as possible has provided a solution to this issue. A large part of nuclear physics is currently focusing on the development of such models. Also, it is focusing on the collection of empirical data that will be used to assess their reliability.

Despite the benefits of using nuclear models to simplify the description of nuclei, there are numerous challenges that still need to be addressed in their development. The vast number of known nuclei and the significant impact of a change even in a single nucleon on the properties of the nucleus are among these challenges. Previous models have been based on close-to-stable nuclei. However, advances in accelerator, separator and detector technology have allowed for more extensive testing of these models under extreme conditions, such as those involving isospin, spin, mass, and deformation. These conditions may lead to the observation of new phenomena, which can serve as robust tests for nuclear models.

The nuclei are organized according to their proton number Z and their neutron number N on a Segré chart, as shown in figure (1.1). Colours are assigned to the chart in order to identify the decay mode of each nuclei. The black colour indicates the stable nuclei, which divides the chart into neutron-rich and proton-rich regions. This work is concentrated on proton-rich nuclei, which exhibit a variety of decay mechanisms. Near stability, the β^+ and electron capture (EC) decays are the dominant radioactivity modes, while in heavier nuclei, alpha decay is predominant when energetically favourable. At the extremes of these regions lie the proton and neutron drip lines, which determine the limit of observable nuclei. The boundaries are constantly advancing with new nuclides discovered.

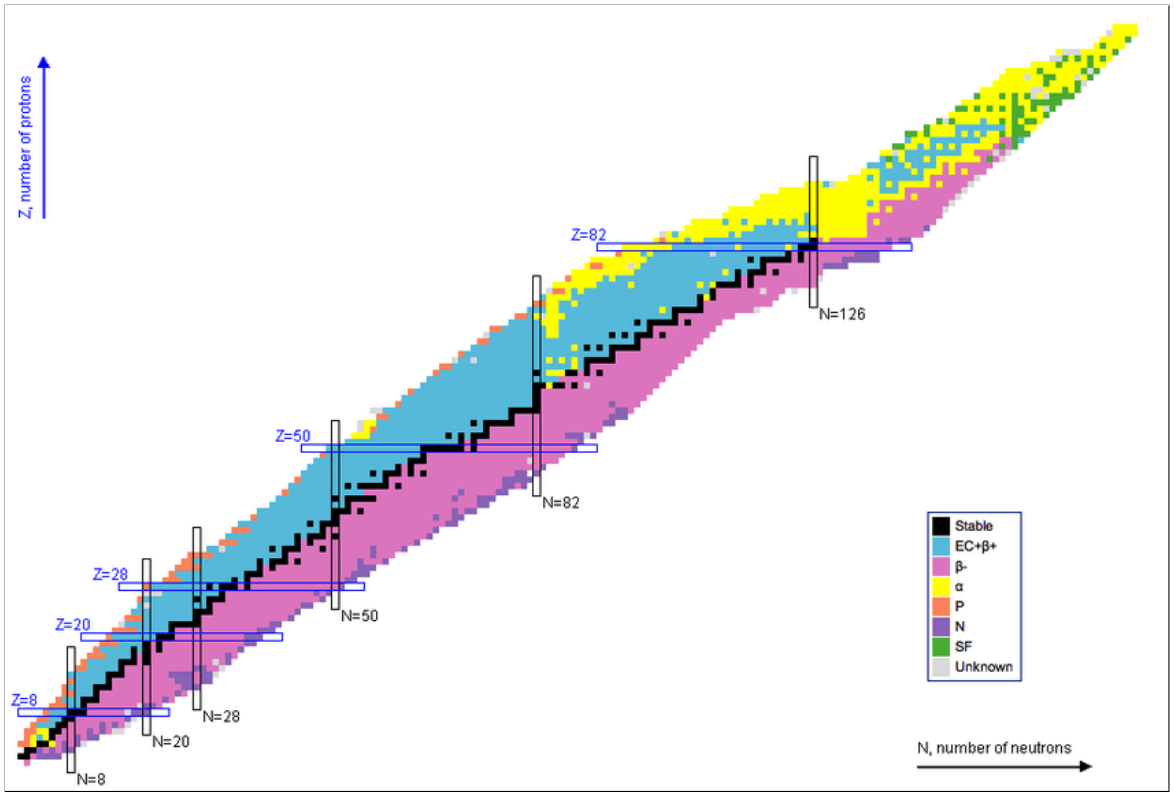

Fig. 1.1 An arrangement of nuclei based on their number of protons Z and neutrons N. The colour coding indicates the decay mode of each nucleus. In N and Z, magic numbers are indicated [2].

Studies of nuclei in these regions is an ideal testing ground for nuclear models. This is because they are far from stable isotopes, which were used as the basis for early nuclear

models. In addition, the wide range of nuclides in these regions enables the examination of systematic trends across chains of nuclei. This demonstrates the effects of adding or removing single nucleons from a system repeatedly.

This work examines nuclei located near the proton drip line and the shell closure at $N = 82$. A nucleus in this region can be considered to be a set of valence nucleons coupled to a semi-magic ^{146}Gd core in which protons can occupy $h_{11/2}$, $d_{3/2}$ and $s_{1/2}$ orbitals, and neutrons can occupy $f_{7/2}$, $h_{9/2}$ and $i_{13/2}$ orbitals. A study of isotonic chains in such proton-rich nuclei can provide insight into how the atomic number Z affects single-particle states through the coupling of only a few valence nucleons.

^{155}Hf nucleus consists of 72 protons and 83 neutrons and decays by beta emission to ^{155}Lu. The lowering in excitation energy of the $27/2^-$ state relative to the $23/2^-$ state across $N = 83$ isotones with increasing Z is considered to be the cause of the formation of isomers. Despite the expectation, this has not yet been demonstrated in ^{155}Hf. Prior to this work, nothing was known about excited states above the beta decaying $7/2^-$ state. Gamma-ray spectroscopy was carried out on excited states in ^{155}Hf in order to investigate the nature of the isomer, identify states above the ground state and determine the progression of the structure towards the proton drip line as Z increases. The comparison with previously studied isotones will provide insight into the influence of the proton valence space on these structures.

Chapter 2 discusses various physics theories that form the foundation for the research presented in this work. In Chapter 3, the experimental methods for producing the nuclei of interest are described, including the newly developed MARA separator. Moreover, it describes the experimental techniques used to analyse the collected data. The main results of the investigation into an isomeric state in ^{155}Hf are presented and discussed in Chapter 4. Conclusion and further work are discussed in chapter 5, within the context of recent discoveries.

Chapter 2

Theoretical Concepts

2.1 Nuclear Binding Energy

Comparing the mass of the nucleus with the mass of its constituents (protons and neutrons) leads to understand the concept of binding energy. It has been found that the sum of the mass of individual nucleons is notably higher than the masses of the nucleus that hold them, this difference in masses Δm is referred to as mass defect. The mass defect is converted to some kind of energy when nuclear species interact with each other. The energy could be represented by Einstein's mass–energy equivalence equation $E = \Delta mc^2 = \Delta m(u)\ 931.49 MeV/u$ where u is the unit of atomic mass, equivalent to one-twelfth of the mass of ^{12}C. The nuclear binding energy B is therefore the energy needed to break an atomic nucleus into its components, protons and neutrons. The binding energy for a nucleus of mass M is given by:

$$B = [\, Zm_p + Nm_n - M \,]\, c^2 \tag{2.1}$$

As the binding energy increases with increasing the mass number, to make a comparative analysis and get an idea of the stability of different nuclear species, the binding energy per nucleon is used. Figure (2.1) shows a graph of the binding energy per nucleon versus the mass number. There are several features that can be observed from the figure, such as the

binding energy ranging from about $6-9\ MeV$, with an average value of $8\ MeV$. In addition, the graph rises at low A, peaks near iron, and then drops off at high A. There are opposing forces, namely the attractive nuclear force, and the repulsive electrostatic force in the nucleus that cause the graph to rise and then fall. Consequently, nuclear reactions involve the fusion of nuclei with atomic numbers lower than the atomic number of Fe and the fission of nuclei with atomic numbers greater than the atomic number of Fe.

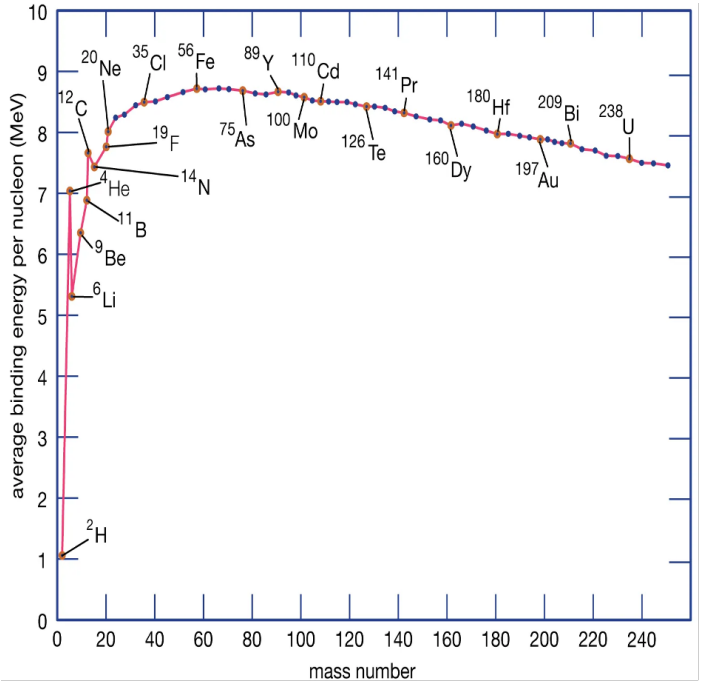

Fig. 2.1 Nuclear binding energies, shown as a function of atomic mass number [3].

2.2 The Drip Lines

The drip lines indicate where bound and unbound nuclei are located in the nuclear chart. The particle separation energy is used to differentiate between bound and unbound nuclei, which refers to the amount of energy required to remove a nucleon from the nucleus. A negative separation energy prevents nucleons from binding to the nucleus, resulting in proton or neutron emission as the nucleus decays. Thus, the drip line can be identified by the point at which the separation energy crosses zero.

For neutron-deficient nuclei, the proton drip line refers to the limit beyond which any additional proton will not be bound "drips from the nucleus". Neutron drip lines can be defined in an analogous manner to proton drip lines. We can calculate the proton and neutron separation energy using:

$$S_n = [m({}^{A-1}_{Z}X_{N-1}) - m({}^{A}_{Z}X_N) + m_n]c^2 \tag{2.2}$$

$$S_p = [m({}^{A-1}_{Z-1}X_N) - m({}^{A}_{Z}X_N) + m({}^{1}H)]c^2 \tag{2.3}$$

Where S_n is the separation energy of the neutron and S_p is the separation energy of the proton. There is a difficulty in studying isotopes beyond the proton drip line as opposed to the neutron drip line. As a result of the proton's charge, many nuclei, especially for heavier nuclei with mass above $A = 100$, exist beyond the proton drip line. This allows for decay by proton emission. The proton must tunnel through the Coulomb barrier in order to be emitted, which results in a half-life of milliseconds to seconds.

2.3 Nuclear Models

There is a great deal of complexity involved in the nature of nuclear force. The nucleons interact not only through reciprocal two-body forces, but also through mutual three-body forces [4, 5, 6]. Mathematical solutions to the many-body problem are therefore challenging. Several equations can be used for describing the interactions between nucleons if we assume the nuclear potential has a very simplified form, such as the form of a square well or that of a harmonic oscillator. Nevertheless, these equations cannot be solved analytically, but instead must be addressed using numerical methods. It is possible to improve that theory by adding additional terms if it has some success in explaining a few nuclear properties. It is possible to simplify the nuclear structure while still preserving its essential properties by implementing a nuclear model. It is necessary for the model to satisfy two requirements; it must be capable

of accounting for nuclear properties previously measured, and it must predict new features that can be observed in future experiments.

To build a nuclear model, analysing experimental data is crucial. Studies such as [7, 8] were able to show evidence that is supportive of the existence of nuclear shells. A plot of measured proton and neutron separation energies is shown in figure (2.2) as a function of proton and neutron numbers. An evidence of shell effects can be seen clearly. It is reasonable to assume that the peaks, which occur at the same number of proton or neutron, in the separation energy correspond (as in the case of the atomic system) to the filling of significant shells. This sudden increase took place when Z or $N = 2, 8, 20, 28, 50, 82, 126$ referred to as magic numbers. It is necessary for any successful theory to be able to account for shell closures at those magic numbers.

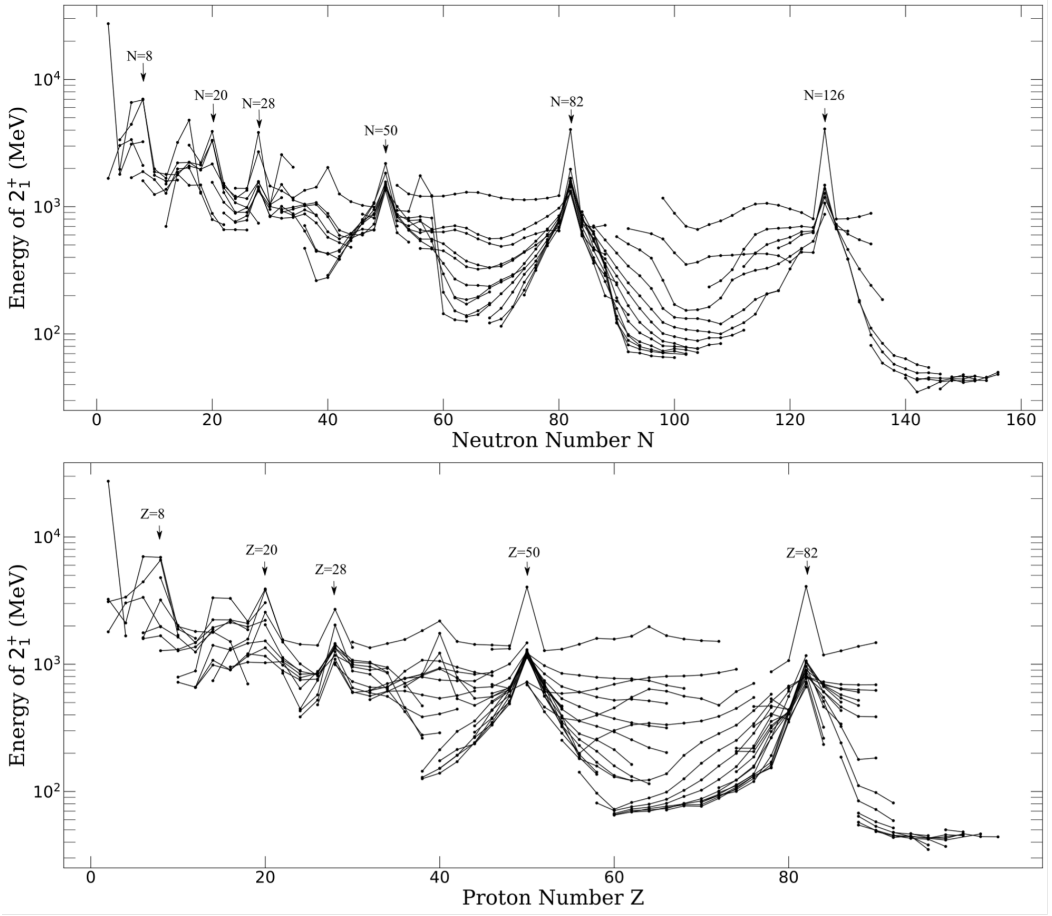

Fig. 2.2 First excited 2^+ states $(E2_1^+)$ plotted for even-even nuclei as a function of proton and a neutron number [9].

2.3.1 The shell model

To develop a shell model, we must solve the Schrodinger equation and select a potential to simulate the nuclear potential which is treated as a mean field. Two potentials were chosen as a start; the infinite square well equation (2.4) and the harmonic oscillator equations (2.5).

$$V(r) = \begin{cases} -V_0 & , r \leqslant R \\ 0 & , r > \end{cases} \tag{2.4}$$

$$V(r) = \frac{1}{2} k r^2 = \frac{1}{2} m w^2 r^2 \tag{2.5}$$

Where r is the distance from the centre of the nucleus, m is mass and ω is the harmonic oscillator frequency and R is the nuclear radius which is equal to $1.25A^{1/3}$ [10]. The two can provide reasonably good solutions to many analytical problems; however, neither could predict the magic numbers above 20 [11]. One explanation for the failure is that the atomic nucleus does not have a sharp edge as in the infinite square well instead, it has what is called a nuclear skin. In contrast, the harmonic oscillator does not possess a sharp enough edge. To account for the thickness of the nuclear skin, we can add a term to the nuclear potential that represents the decline of the potential from 90% to 10%.

It has been found that the Woods-Saxon potential is the best physical description of the nuclear potential. It is somewhere between the square well and the harmonic oscillator in terms of the rounded edges. Due to the proton's positive charge, an extra term is added to account for the Coulomb potential $V_c(r)$, figure (2.3) illustrates the potential difference between the proton and neutron.

The Woods-Saxon potential can be written as follows, where a is the skin thickness or the diffuseness term:

$$V(r) = \frac{-V_0}{1 + \exp(\frac{(r-R)}{a})} \tag{2.6}$$

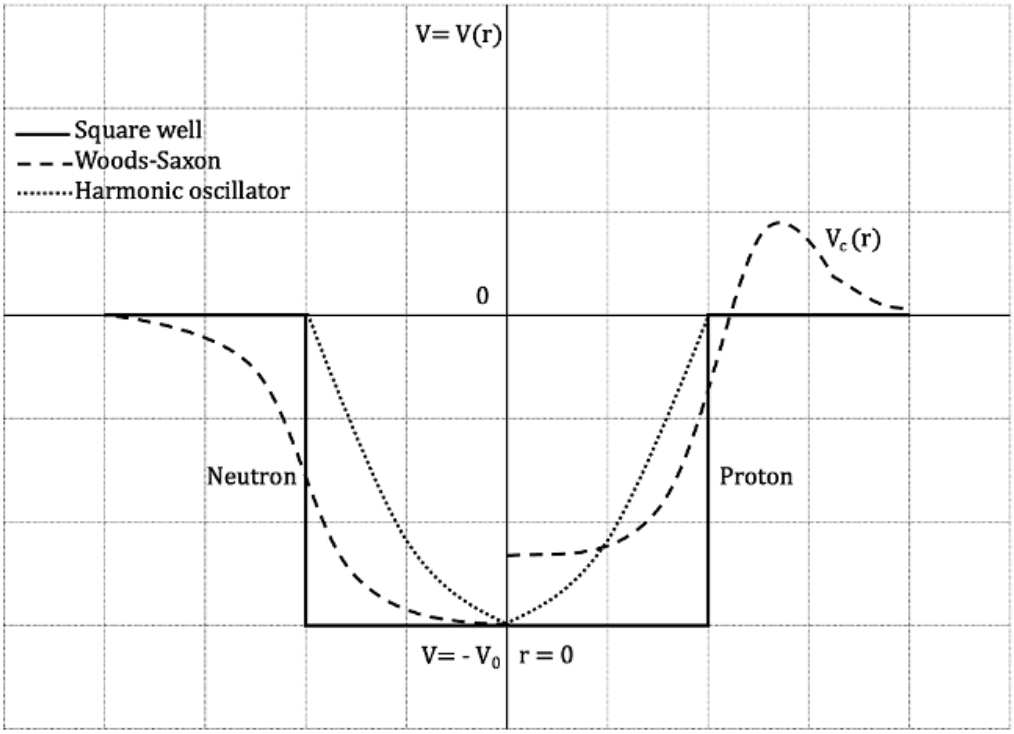

Fig. 2.3 A plot of Square well, Harmonic oscillator, and Woods-Saxon nuclear potentials in relation to r, the distance from the nucleus' centre.

It is also capable of predicting the first three magic numbers but failed to predict the remaining numbers. A modification of the potential is needed to generate the right magic numbers. Hence, it is necessary to add different terms to the equation in order to improve the results, since we do not want to change the physical content of the equation, which provides already a very good estimate of how the nuclear potential is likely to look. It was discovered that a spin-orbit potential could present the necessary correction, resulting in a proper separation of the sub-shells [4, 6]. It occurs as a result of the interaction between the orbital angular momentum L and the intrinsic spin S of the nucleon. Spin-orbit adjustment can be expressed as follows:

$$V(r) \Rightarrow V(r) + V_{so}(r)\,\vec{l}\cdot\vec{s}$$
$$\vec{l}\cdot\vec{s} = \tfrac{1}{2}\left(\vec{j}^{\,2} - \vec{l}^{\,2} - \vec{s}^{\,2}\right) \tag{2.7}$$

where $V_{so}(r)$ is the strength of the interaction, $s = \pm 1/2$ the intrinsic spin, $l = 0,1,2,3,\ldots$ corresponding to the notation $s,d,p,d,f,\ldots$ and $j = l + s$. The single-particle energy levels can be seen in the right hand side of figure (2.4) which were obtained from this potential.

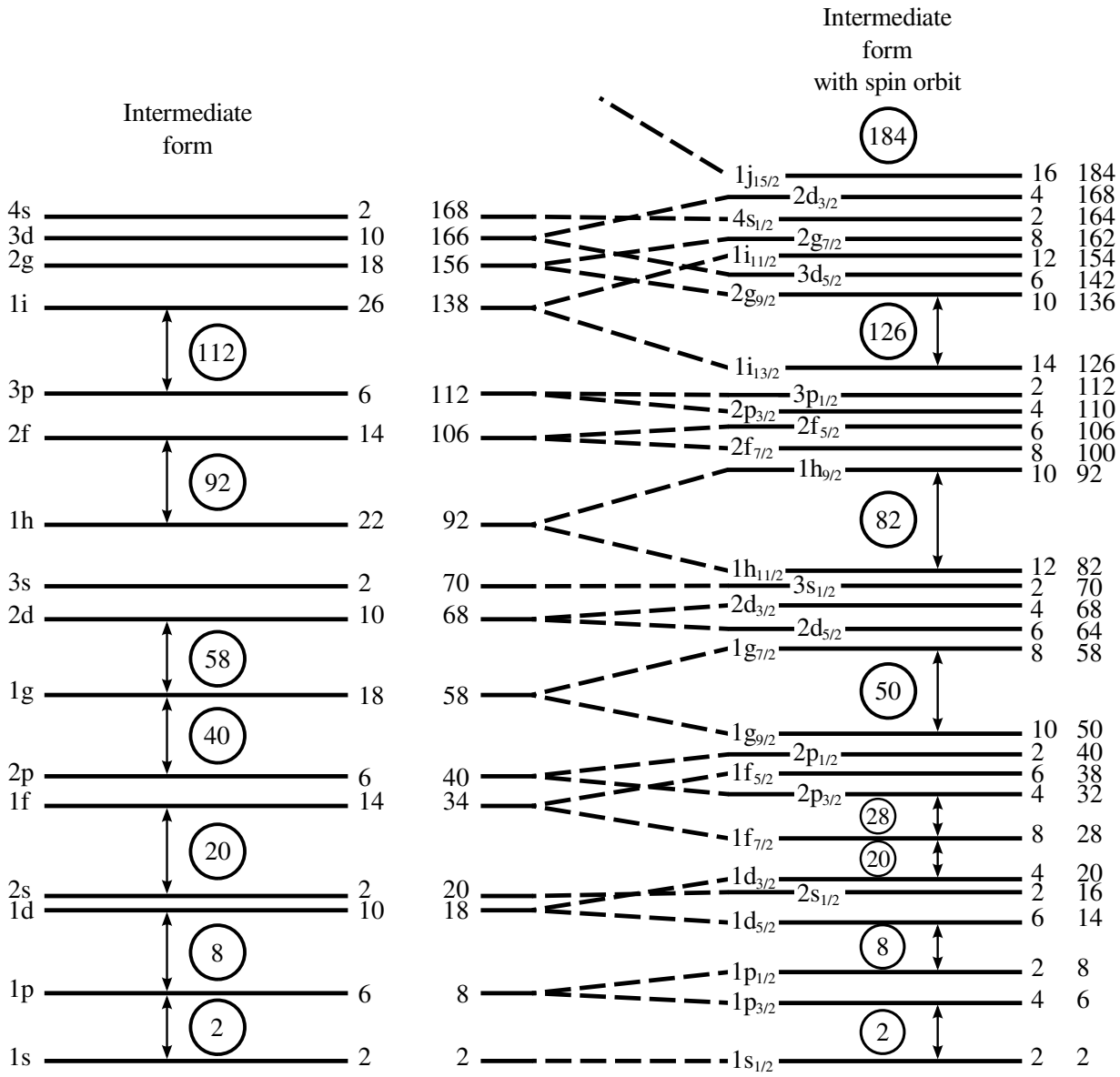

Fig. 2.4 Single-particle shell-model energy levels derived from a Woods Saxon potential without and with spin-orbit $l.S$ correction applied (left and right, respectively) [10].

2.4 Multiparticle Configurations

Most often the nucleons inside the nucleus are viewed as being composed of two structures, a stable core and a valence nucleons. Protons and neutrons that are not contained within the closed shell "core" are called valence nucleons. A consideration of residual interactions between valence nucleons is essential to understanding the behaviour and structures of nuclei with nucleons outside closed shells. In the case of multiparticle configurations ($n > 2$), the Pauli principle constraints must be taken into account in order to calculate the total angular momenta J. The m-scheme is one of the most straightforward methods of addressing any issues related to compliance with Pauli principle. For example assuming that there are three protons in the $h_{\frac{7}{2}}$. The protons are unable to couple to a $J = \frac{21}{2}$, since such a state must have an $M = \frac{21}{2}$ substate and we will have to violate the Pauli principle if we required three protons to be in the $m = \frac{7}{2}$ substates. The m scheme for the configuration $|(\frac{7}{2})^3 J\rangle$ is shown in table (2.1). The maximum angular momentum value of any configuration J^n can be calculated from [12];

$$J_{max} = n\ j - \frac{n\ (n-1)}{2} \tag{2.8}$$

It is also fundamental to understand the concept of seniority when it comes to multiparticle configuration. Due to the fact that it produces many simple, yet effective results when applied to a variety of scenarios. Additionally, several realistic residual interactions conserve seniority, so this scheme yields a reasonable prediction for actual nuclei. In configuration $(j)^n$, seniority"v" is equivalent to the number of unpaired nucleons in the state of angular momentum J. When $v = 0$, this means that all particles are paired, and thus $J = 0$. With increasing v, the number of pairs is given by $(n - v)/2$.

The following example describes this concept in greater detail. Consider the $(f_{7/2})^3$ configuration, based on the m-scheme and from equation (2.8) , $J_{max} = 3*(7/2) - [3(3-1)]/2 = 15/2$. In order to obtain this state, it is necessary to maximize the alignment of all $j = 7/2$ angular moments in accordance with the Pauli principle. As a result, the $J = 15/2$ state has a seniority 3; no particles are coupled in pairs to $J = 0$. Alternatively, it could be possible to couple one

pair of particles to $J = 0$ and then using the remaining $|(7/2)^1 J >$ configuration to produce angular momenta of , $7/2$, or $5/2$, such states have seniority $v = 1$. Finally, any state with $J = 0$ in the $(L_j)^n$ configuration clearly has seniority 0, that is, all particles are coupled in pairs to $J = 0$.

2.5 Radioactive Decay

The elements in nature can be classified into two types, stable and unstable. The unstable species undergo a characteristic loss of energy during the process of radioactive decay in order to reach a more stable state known as the ground state. The energy lost is typically in the form of α decay , β^-decay, protons and neutrons emission or fission process. As defined by the exponential law, the amount of energy released changes exponentially with time:

$$N(t) = N_0 \, e^{-\lambda t} \tag{2.9}$$

Where $N(t)$ and N_0 are the number of radioactive nuclei at time t and $t = 0$ respectively, λ is the decay constant or the disintegration constant which represents the probability of the decay per unit time. The decay constant is related to the half-life of the nuclide (the time required for half of the nuclei to decay) $T_{1/2}$ through : $T_{1/2} = \ln 2/\lambda$. It is possible to derive the radioactive decay law for activity calculations, which is more practical to use. In this case, equation 2.9 can be written as follows:

$$\frac{dN}{dt} = A(t) = \lambda \, N(t) = A_0 \, e^{-\lambda t} \tag{2.10}$$

The spontaneous release of energy occurs through a variety of mechanisms, which are represented by different colours in the nuclear chart shown in figure (1.1).
In beta decay, a nucleon undergoes a transition from one type to another accompanied by electrons or positrons. Other ways of reaching more stable states include proton and neutron

Table 2.1 The m scheme for the configuration $|(\frac{7}{2})^3 J\rangle$.

j_1	j_2	j_3	M	J
$\frac{7}{2}$	$\frac{5}{2}$	$\frac{3}{2}$	$\frac{15}{2}$	
$\frac{7}{2}$	$\frac{5}{2}$	$\frac{1}{2}$	$\frac{13}{2}$	
$\frac{7}{2}$	$\frac{5}{2}$	$-\frac{1}{2}$	$\frac{11}{2}$	
$\frac{7}{2}$	$\frac{5}{2}$	$-\frac{3}{2}$	$\frac{9}{2}$	$\frac{15}{2}$
$\frac{7}{2}$	$\frac{5}{2}$	$-\frac{5}{2}$	$\frac{7}{2}$	
$\frac{7}{2}$	$\frac{5}{2}$	$-\frac{7}{2}$	$\frac{5}{2}$	
$\frac{7}{2}$	$\frac{3}{2}$	$\frac{1}{2}$	$\frac{11}{2}$	
$\frac{7}{2}$	$\frac{3}{2}$	$-\frac{1}{2}$	$\frac{9}{2}$	
$\frac{7}{2}$	$\frac{3}{2}$	$-\frac{3}{2}$	$\frac{7}{2}$	$\frac{11}{2}$
$\frac{7}{2}$	$\frac{3}{2}$	$-\frac{5}{2}$	$\frac{5}{2}$	
$\frac{7}{2}$	$\frac{3}{2}$	$-\frac{7}{2}$	$\frac{3}{2}$	
$\frac{7}{2}$	$\frac{1}{2}$	$-\frac{1}{2}$	$\frac{7}{2}$	
$\frac{7}{2}$	$\frac{1}{2}$	$-\frac{3}{2}$	$\frac{5}{2}$	
$\frac{7}{2}$	$\frac{1}{2}$	$-\frac{5}{2}$	$\frac{3}{2}$	$\frac{7}{2}$
$\frac{7}{2}$	$\frac{1}{2}$	$-\frac{7}{2}$	$\frac{1}{2}$	
$\frac{7}{2}$	$-\frac{1}{2}$	$-\frac{3}{2}$	$\frac{3}{2}$	
$\frac{7}{2}$	$-\frac{1}{2}$	$-\frac{5}{2}$	$\frac{1}{2}$	$\frac{15}{2}$
$\frac{5}{2}$	$\frac{3}{2}$	$\frac{1}{2}$	$\frac{9}{2}$	
$\frac{5}{2}$	$\frac{3}{2}$	$-\frac{1}{2}$	$\frac{7}{2}$	
$\frac{5}{2}$	$\frac{3}{2}$	$-\frac{3}{2}$	$\frac{5}{2}$	
$\frac{5}{2}$	$\frac{3}{2}$	$-\frac{5}{2}$	$\frac{3}{2}$	$\frac{9}{2}$
$\frac{5}{2}$	$\frac{3}{2}$	$-\frac{7}{2}$	$\frac{1}{2}$	
$\frac{3}{2}$	$\frac{1}{2}$	$-\frac{1}{2}$	$\frac{3}{2}$	$\frac{3}{2}$
$\frac{3}{2}$	$\frac{1}{2}$	$-\frac{3}{2}$	$\frac{1}{2}$	

emission; nevertheless, almost all radioactive decay is accompanied by gamma decay, which is an electromagnetic wave. As can be seen from the figure above, the dominant decay mode in heavy nuclei is alpha decay. The following sections provide further details on these types of decay.

2.5.1 Alpha decay

During alpha decay, a nucleus spontaneously releases energy by forming alpha particles (two protons and two neutrons), which are equivalent to the helium nucleus. The reaction can be described in the following manner:

$$^{A}_{Z}X \longrightarrow ^{A-4}_{Z-2}X' + ^{2}_{4}He \tag{2.11}$$

Where X is the mother nucleus, Z is the proton number, A is the mass number, and X' is the daughter nuclide with a proton number of $Z-2$ and a mass number of $A-4$. According to equation (2.11), spontaneous decay occurs due to the difference in mass between the two sides, where the alpha particle has a more tightly bound structure than the components of the separate particle. The difference in masses is expressed as the kinetic energy of the emitted alpha particles. This explains why many heavy nuclei prefer to decay via alpha emission since it provides the opportunity to release the maximum amount of energy. In neutron-deficient nuclei, alpha emission occurs primarily after $Z = 52$ and becomes more common above $N = 82$ when the nucleus has a neutron deficiency.
Assuming that X is at rest, the total amount of energy released in the decay is determined by applying the conservation of energy law before and after the decay. This result leads to the quantity of Q being the difference in the masses of the mother particle M_x and the daughter particle $M_{X'}$. It is written as follows:

$$Q = (M_x - M_{X'} - M_\alpha)\, c^2 \tag{2.12}$$

It is believed that, the emitted particles are formed within the mother before they emit, and the possibility of them emitting depends upon the rate of particle formation and the probability of an alpha particle tunnelling through the nuclear potential barrier to reach the daughter. When an alpha particle is emitted from a nucleus, it causes the mother nucleus to recoil. As a result, the detected energies of alpha particles actually represent both the energies of the alpha particles and the energy of their recoil daughters [13]. The detected energy E_d can be calculated as follows:

$$E_d = E_\alpha + E_R * K \tag{2.13}$$

Where E_α is alpha's energy, K is the detection efficiency, which depends on the recoiling energies for light nuclides, whereas K is almost constant for heavy nuclides $(A > 100)$, and E_R is the recoil energy calculated from:

$$E_R = \frac{4E_\alpha}{A-4} \tag{2.14}$$

2.5.2 Beta decay

The process of β decay occurs when a neutron transforms into a proton or a proton converts into a neutron and accompany by the emission of an electron e^-or a positron e^+respectively, as shown in equation (2.15). It can be seen from the nuclear chart that the two types of decay occur above and below the line of maximum beta stability, where nuclei with excess protons experience β^+ decay, while proton-deficient nuclei undergo β^- decay. A nuclide undergoing β decay can slide down the mass line of constant A towards the stable isobar.

$$\begin{aligned} {}^{A}_{Z}X_N &\rightarrow {}^{A}_{Z-1}X'_{N+1} + e^+ + \nu_e \ , \qquad \beta^+ \\ {}^{A}_{Z}X_N &\rightarrow {}^{A}_{Z+1}X'_{N-1} + e^- + \bar{\nu}_e \ , \qquad \beta^- \end{aligned} \tag{2.15}$$

v_e and $\bar{v}_e$ represent the neutrino and anti-neutrino, respectively. There is substantial evidence that electrons are not nuclear constituents, and so we must consider the β decay process to be a process that generates an electron from the available decay energy during the decay process, which is then ejected from the nucleus immediately after. In contrast to alpha decay, in which α particle existed in a nucleus before it was released.

Figure (2.5) shows an illustrative energy spectrum generated by the decay of ^{137}Cs, where beta particle energies appear as a continuous distribution, in contrast to alpha particle energies that are sharp and well defined. The energy of beta decay is representative of the difference in energies between the initial and final levels. Based on the distribution of electron energies, the conservation of energy law would be violated if only electrons were released in such a decay. It is this fact that leads to the discovery of the emitted neutrino and antineutrino during this process. The neutrino and anti-neutrino carry the energies that are missing from the ejected electron's energies. Conservation of electric charge dictates the neutrino to be uncharged, and angular momentum conservation requires the neutrino to have a spin of $1/2$. It is possible to formulate the relevant Q-value for both process as follows:

$$\begin{aligned} Q_{\beta^+} &= \left\{ m\left({}^{A}_{Z}X_N\right) - m\left({}^{A}_{z-1}X'_{N+1}\right) - 2m_e \right\} c^2 \\ Q_{\beta^-} &= \left\{ m\left({}^{A}_{Z}X_N\right) - m\left({}^{A}_{z+1}X'_{N-1}\right) \right\} c^2 \end{aligned} \tag{2.16}$$

In some cases, β decay may not be energetically feasible when the calculated Q-value is given a negative number. The decay may proceed via electron capture when such conditions are present and is described by the following formula;

$${}^{A}_{Z}X_N + e^- \rightarrow {}^{A}_{Z-1}X'_{N+1} + v_e \tag{2.17}$$

In this process a bound electron is captured by the nucleus during the transformation process, because of which there is no need for positron formation and thereby lowering the energy

threshold. The probability of electron capture decreases with increasing orbital quantum number, so it is more likely that the nucleus will capture a K-shell electron. In the event that this occurs, an electron will jump from a higher energy level to fill the hole that has been left by the ejected electron. This results in the emission of a characteristic X-ray of the element. The electron capture Q-value can be calculated from;

$$Q_{EC} = \left\{ m\left({}^{A}_{Z}X_{N}\right) - m\left({}^{A}_{z-1}X'_{N+1}\right) \right\} c^2 - B_e \tag{2.18}$$

Where B_e is the binding energy of the captured electron.

2.5.3 Proton decay

Among decay types, proton emission is relatively uncommon, taking place only in proton-rich nuclei or in highly excited states that undergo a β-decay. The rate at which these protons are emitted following a beta decay is primarily governed by beta decay. This emission is therefore referred to as beta-delayed proton emission. Furthermore, this type of decay occurs more often near the proton drip line, where the proton's separation energy approaches negative values. An unstable nucleus emitting a proton can be represented by the following formula.

$${}^{A}_{Z}X \longrightarrow {}^{A-1}_{Z-1}X' + n\,{}^{1}_{1}P \tag{2.19}$$

Where X is the mother nucleus, $X\prime$ is the daughter nuclide with a proton number of $Z-1$ and a mass number of $A-1$ and n is equal to 1 or 2. Some nuclides prefer to decay through the emission of double protons and not by the emission of a single proton such as ^{45}Fe [14]. It can be explained by the fact that the separation energy of two protons is lower than the separation energy of a proton. Due to this, even-Z nuclei usually undergo two proton emissions, whereas odd-Z nuclei are more likely to decay by emitting a single proton. Equation (2.3) can be used to calculate the proton separation energy.

There are many similarities between the proton decay and alpha decay processes. The proton

decay process can also be viewed as a quantum tunnelling process. A proton must penetrate a potential barrier in order to be emitted. If the proton separation energy is negative, the proton is unbound and tunnels out of the nucleus within a specific time period. Proton decay half-lives are highly dependent upon the spin of the emitting nucleus, and can be used to determine the spin of emitting states.

2.5.4 Gamma decay

Alpha and beta decays, as well as most nuclear reactions, can leave the final nucleus in an excited state. From these excited states, certain electromagnetic photons, similar to X-rays and visible light, are emitted known as gamma radiation. A gamma ray can have an energy between $\sim 40\,keV$ and $10,000\,keV$, which is characteristic of the energy difference between nuclear states, and corresponding wavelengths between 1.4 to 100 fm. In comparison to visible light, these wavelengths are 10^6 times shorter.

Studying gamma-ray emission has become a standard method of nuclear spectroscopy because it gives us detailed information about the excited states. Additionally, this method is popular and useful because it is relatively easy to observe gamma rays in which there is no significant absorption or scattering in air, contrary to the behaviour of alpha and proton decays as well as the precision for measuring their energies (and therefore the excited states energies). Furthermore, we can determine the spins and parities of excited states by examining gamma emission in conjunction with its competing process, internal conversion.

Assuming an excited state E_i in nucleus of mass M at rest decays to a final excited nucleus E_f. In order to conserve energy and linear momentum, the final nucleus will have a recoil momentum P_R and a corresponding recoil kinetic energy T_R. Thus the energy of the emitted gamma ray E_γ is written as :

$$E_\gamma \simeq \Delta E - \frac{\Delta E^2}{2Mc^2} \tag{2.20}$$

Where $\Delta E = E_f - E_i$. It is usually not necessary to correct the energy due to recoil, and any correction to the energy is usually very small, in the order of 10^{-5}, when compared to the

amount of uncertainty associated with experimental measurements. Therefore, the second term in equation (2.20) is often neglected thus it is expressed as:

$$E_\gamma = E_i - E_f \tag{2.21}$$

Positively charged protons distributed within the nucleus produces an electric field and the movement of the nucleons causes a current which, in turn, creates a magnetic field. We can generalize the properties of dipole radiation by defining the coefficient L of the radiation so that 2^L represents the order of the multipoles where $L = 1$ for dipoles, $L = 2$ for quadruples, etc. with E for electric and M for magnetic. The emitted radiation's electric or magnetic nature is determined by the parity selection rule given below:

$$\begin{aligned} (EL)\ \pi_i \cdot \pi_f &= (-1)^L \\ (ML)\ \pi_i \cdot \pi_f &= (-1)^{L+1} \end{aligned} \tag{2.22}$$

Where π_i is the parity of the initial state and π_f is the parity of the final state. As the emission of gamma ray is subject to the law of angular momentum conservation, the angular momentum L of the emitted gamma ray will follow the following relationship for initial and final states with angular momentum I_i and I_f, respectively.

$$\left|I_i - I_f\right| \leq L \leq I_i + I_f \tag{2.23}$$

As a way to convert classical theory to quantum theory, we just need to quantify the classical multipole moments, which constitute the radiation field. The amount of energy radiated per unit time is given by $\hbar\omega$ hence, the decay constant which is the probability per unit time for photon emission is

$$\lambda(\sigma L) = \frac{P(\sigma L)}{\hbar\omega} = \frac{2(L+1)}{\varepsilon_0 \hbar L[(2L+1)!!]^2} \left(\frac{\omega}{c}\right)^{2L+1} [m_{\text{fi}}(\sigma L)]^2 \tag{2.24}$$

Table 2.2 Weisskopf estimates for electric and magnetic γ-ray transition rates (s^{-1}) in terms of mass number A and transition energy E_γ (MeV) [10].

Electric Transitions	Magnetic Transitions
$\lambda(E1) = 1.0\times10^{14}A^{2/3}E_\gamma^3$	$\lambda(M1) = 3.1\times10^{13}E_\gamma^3$
$\lambda(E2) = 7.3\times10^{7}A^{4/3}E_\gamma^5$	$\lambda(M2) = 2.2\times10^{7}A^{2/3}E_\gamma^5$
$\lambda(E3) = 34A^{2}E_\gamma^7$	$\lambda(M3) = 10A^{4/3}E_\gamma^7$
$\lambda(E4) = 1.1\times10^{-5}A^{8/3}E_\gamma^9$	$\lambda(M4) = 3.3\times10^{-6}A^{2}E_\gamma^9$
$\lambda(E5) = 2.4\times10^{-12}A^{10/3}E_\gamma^{11}$	$\lambda(M5) = 7.4\times10^{-13}A^{10/3}E_\gamma^{11}$

where σ denotes either magnetic or electric gamma ray. In order to calculate the matrix element $m_{fi}(\sigma L)$, initial and final wave functions must be known. By assuming that the transition between shell-model states is the result of a single proton changing state, we are able to simplify the calculation and estimate the probability of emission of gamma rays. The following equations are used to determine the probability of electric and magnetic transitions.

$$\lambda(EL) \simeq \frac{8\pi(L+1)}{L[(2L+1)!!]^2}\frac{e^2}{4\pi\varepsilon_0\hbar c}\left(\frac{E}{\hbar c}\right)^{2L+1}\left(\frac{3}{L+3}\right)^2 cR^{2L} \tag{2.25}$$

$$\begin{aligned}\lambda(ML) \simeq \frac{8\pi(L+1)}{L[(2L+1)!!]^2}&\left(\mu_\mathrm{p}-\frac{1}{L+1}\right)^2\left(\frac{\hbar}{m_\mathrm{p}c}\right)^2\left(\frac{e^2}{4\pi\varepsilon_0\hbar c}\right)\\ &\times\left(\frac{E}{\hbar c}\right)^{2L+1}\left(\frac{3}{L+2}\right)^2 cR^{2L-2}\end{aligned} \tag{2.26}$$

Where $R = R_0\,A^{1/3}$ is the radius of the potential well and R_0 is a constant value equal to 1.2 fm. The previous estimation is known as Weisskopf estimate of transition rates [15]. These are used as a guide to check the experimental assignment of a gamma transition and not an actual calculation. Consequently, if there is a disagreement between the measured and calculated values this might be explained by investigating the possibility that the state is formed from multi-particle configuration and not from a single nucleon in contrast to what Weisskopf estimation assumed. In Table (2.2), the Weisskopf estimates are presented for lower multipolarities.

Table 2.3 The decay data of ^{137}Cs Half-Life: $(4943 \pm 5)d$ to ^{137m}Ba by beta decay [16, 17].

Radiation type	Energy (kev)	Intensity $(\%)$
Auger-L	5.9	7.28 (12)
Auger-K	37.41	0.76 (4)
IC e^-_K	624.22	7.62 (19)
IC e^-_L	656	1.42 (19)
$\beta^-_{\max}$	513.97	94.36 (28)
$\beta^-_{\max}$	1175.6	5.64 (28)
γ	661.66	85 (20)

2.5.5 Internal conversion

The process of internal conversion can be thought of as an electromagnetic process which competes with the process of gamma emission. Here, instead of emitted photons from the nucleus, the electromagnetic multipole fields of the nucleus interact with the atomic electrons and make one of the electrons leave the atom. This is in contrast to beta decay where the electron is physically created inside the nucleus and is then emitted. Furthermore, what is important to understand is that this is not a two-step process, in which the nucleus first emits a photon and then the photon knocks out an orbiting electron similar to how the photoelectric effect operates. The emitted electron or what we usually refer to as the conversion electron has a kinetic energy T_e equal to the energy difference between the initial state and the final state ΔE minus the binding energy of the electron B, this can be written as:

$$T_e = \Delta E - B_e \tag{2.27}$$

As the electrons arranged around nucleus in a specific states or shells $K, L, M...$, the binding energy of the conversion electron will differ depending on which state the electron emitted from. This will lead to discrete peaks appear on the top of the beta continuum separated by values that express the difference in energy between the electron orbitals. If dealing with a radioactive decay, the binding energies of electrons represent the values of the

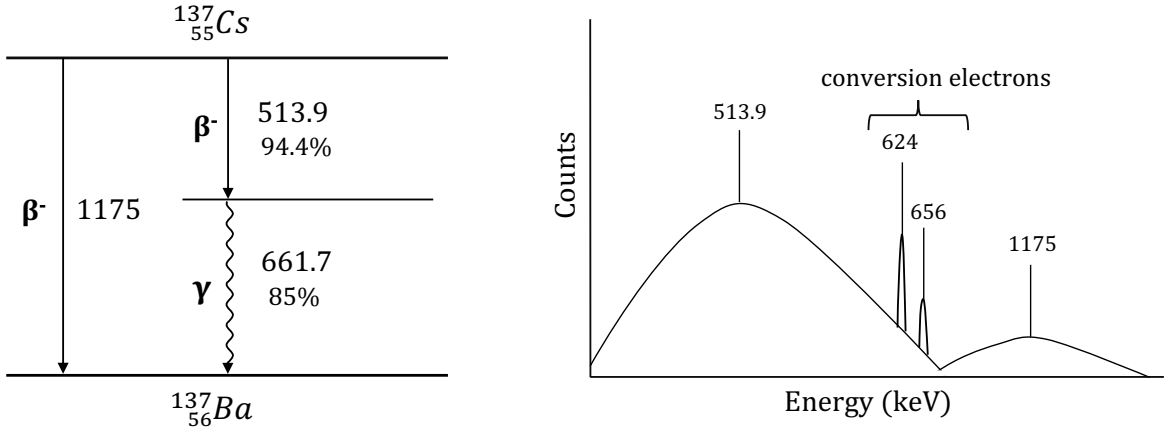

Fig. 2.5 The decay scheme of ^{137}Cs to ^{137m}Ba (left). An approximate energy spectrum represents the decay of ^{137}Cs nucleus (right). On the continuous background of β decay discrete conversion electron peaks are shown.

daughter nuclei and not the mother nucleus. Looking at the decay scheme in figure (2.5), ^{137}Cs decays to ^{137}Ba trough emitting beta particles. The state at 661.7 keV has a 85% chance to decay through gamma and 15% by emitting the conversion electrons, the peaks at 624.22 $(661.66 - 37.41)$ keV and 656 $(661.66 - 5.9)$ keV in the spectrum corresponding of the emission of electrons from the K and L shell respectively.

A more recent example that has been discovered using data from the same experiment as that used in this study involves conversion electrons depopulating the high-spin $(25/2^-)$ isomeric state in ^{155}Lu [9]. The relevant part of the level scheme that illustrates the electro-magnetic branch is shown in figure (2.6, a) while the energy spectrum containing the electron peaks is shown in figure (2.6, b). The difference in energy between the two peaks corresponds to the difference between the K and L levels, which are about 63 and 10 keV respectively.

As the electrons being ejected from the atom, another electron from higher energy orbit jumped to fill the vacancy left behind it, this leads to the characteristic X-ray emission. The X-ray peaks usually appear in the low energy region of gamma spectrum. Auger electrons can also be detected in a charge particle detector as it is competed with the emission of X-ray. Both of these, X ray and Auger electrons, are useful in identifying decaying species based on the Z-dependent energies.

For electric and magnetic transitions, the internal conversion coefficients $(ICCs)$ α can

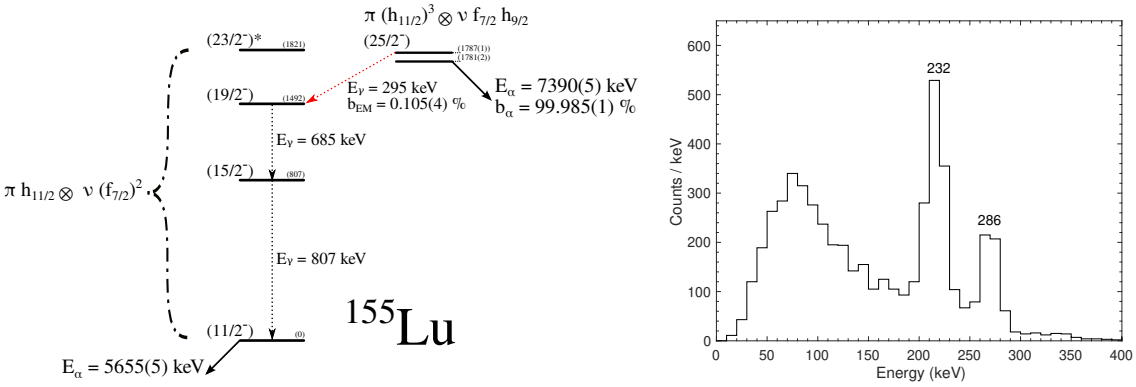

(a) (b)

Fig. 2.6 (a) The level scheme of ^{155}Lu, the red arrows show the electro-magnetic branch of the decay of the $h_{11/2}$ state, recently discovered [9]. The energy spectrum in (b) shows the conversion electrons appear on the continuous background of beta decay.

be approximated roughly with a simple, non-relativistic image, in which the nucleus is considered as a point and energies exceed a threshold. With n being the principle quantum number, this is written for electric and magnetic multipoles as:

$$\alpha(EL) \simeq \frac{Z^3}{n^3}\left(\frac{L}{L+1}\right)\left(\frac{e^2}{4\pi\varepsilon_0\hbar c}\right)^4\left(\frac{2m_ec^2}{E}\right)^{L+5/2}$$
$$\alpha(ML) \simeq \frac{Z^3}{n^3}\left(\frac{e^2}{4\pi\varepsilon_0\hbar c}\right)^4\left(\frac{2m_ec^2}{E}\right)^{L+3/2} \tag{2.28}$$

BRICC program, which uses the Dirac-Fock method to calculate the internal conversion coefficients values, is currently available to give the best estimation [18]. For a given decay energy, the internal conversion coefficient measures the ratio between electrons emission and gamma-rays emission, and defined as:

$$\alpha = \frac{\lambda_e}{\lambda_\gamma} \tag{2.29}$$

Accordingly, the total probability of a state to decay is consist of two components as:

$$\begin{aligned} \lambda_t &= \lambda_e + \lambda_\gamma \\ &= \lambda_\gamma(1+\alpha) \\ &= \lambda_\gamma(1+\alpha_K+\alpha_L+\alpha_M+...) \end{aligned} \tag{2.30}$$

Where $\alpha = \alpha_K + \alpha_L + \alpha_M + ...$ and each individual atomic shell represents the total coefficient of sub-shells. Although the total conversion electrons coefficient is usually used when gamma intensity correction is done, the main contribution is from the K-shell emission. Furthermore, the correction becomes essential for low energy gamma ray transition in nuclei with higher Z, these features could be noticed from equation (2.28). Additionally, the coefficient value is highly dependent on the multipole order, as the multipole order increases, the conversion coefficients rise rapidly. Consequently, the conversion electron emission probability is likely to be greater than the gamma emission for the higher multipole values. Lastly, a major advantage that allows us to determine the relative parities of nuclear states is using the fact that the coefficients differ significantly for electric and magnetic transitions. All the previous features are illustrated in figure (2.7).

2.6 Nuclear Isomers

A nuclear isomer is a state of an atomic nucleus that has a longer lifetime than other states of the same nucleus. These isomers are often called nuclear metastable states or simply nuclear isomeric states. Nuclear isomers have been observed in a wide range of nuclei across the nuclei chart [19]. Typically, isomers are denoted with a superscript 'm' after the atomic mass number (e.g., ^{156m}Hf). In general, when an excited nucleus transitions from a higher energy state to a lower energy state, it emits a gamma ray and quickly decays to its ground state. However, in the case of nuclear isomers, the transition to the ground state is hindered by a relatively long half-life. This occurs because the isomeric state has certain properties that

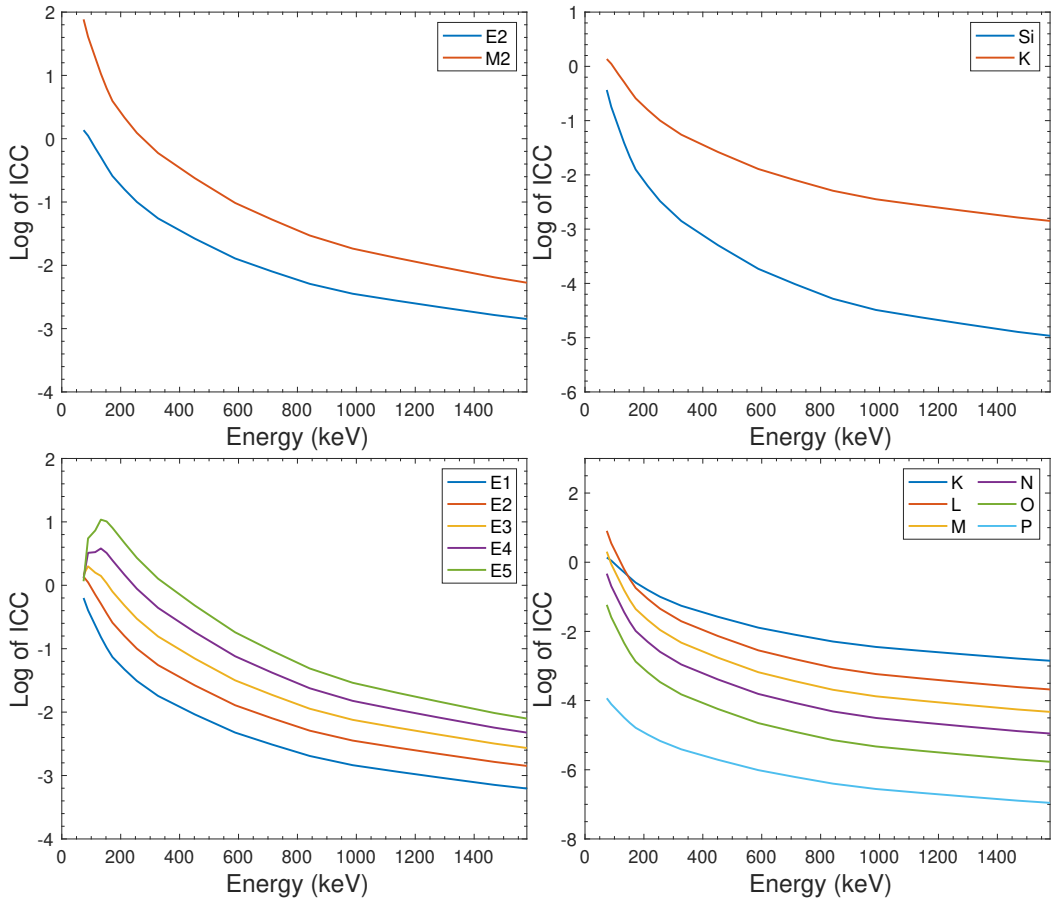

Fig. 2.7 Characteristics of the internal conversion coefficients as a function of energy. The electric and magnetic coefficients of transitions of multipole order 2 in ^{155}Hf (top left). A comparison of the effects of atomic number on the $E2$ transitions for $Si(Z = 14)$ and $K(Z = 19)$ (top right).The coefficient for multipole orders $1,2,3,4$ and 5 of electric transitions in ^{155}Hf (bottom left). A comparison of the different contributions of atomic shells (bottom right). In each case values were calculated using BRICC [18].

make spontaneous transitions less likely.

A variety of factors contribute to the stability of nuclear isomers. The arrangement of nucleons within the nucleus is a major contributor to the formation of the energy barriers. These barriers make it difficult for the system to transition to a lower energy state. The conservation of angular momentum and parity is another factor that leads to the long lifetime of nuclear isomers. Certain combinations of these properties prevent isomeric states from decaying by fast gamma-ray emission. Isomers can be classified into different types. The following are some common types of nuclear isomers:

- Alpha isomers: these are characterized by an excited state that decays by emitting an alpha particle. These isomers are less common and typically occur in heavy nuclei.
- Beta isomers: these isomers contain an excited state which decays via the emission of beta particles. Depending on precise details such as energy, spin, and parity, the half-lives of isomers can be shorter or longer than the ground-states half-lives.
- Proton isomers: in proton isomers, an excited state decays by emitting a weakly bound proton. These isomers are common in neutron-deficient nuclei near the proton drip line.
- Gamma isomers: this type involve an excited nuclear state that decays to the ground state by emitting one or more gamma rays. These isomers are distinguished by an isomeric transition where the nucleus undergoes a change in energy level through gamma ray emission. Among the different types of isomers, gamma isomers are the most common.
- Internal conversion Isomers: it occur when an excited state decays by transferring its energy directly to the orbital electron rather than emitting gamma rays. The suppression of gamma-ray emission increases the lifetime of the excited state.

These classifications are not mutually exclusive, and some isomers may possess characteristics of several types. Depending on the nucleus' properties, including its atomic number, neutron-to-proton ratio, and the arrangement of nucleons within the nucleus, a specific type

of isomer is observed. Furthermore, there are a few more distinct categories of nuclear isomers that are of particular importance:

- Spin-trap isomers:

  The half-life of an excited state is highly influenced by the decay pathways available. The half-lives will be longer for gamma emmission with high multipolarity and low energy. Consequently, states decaying through low energy and/or high multipolarity transitions are often isomeric. There is no structure-related hindrance required for these isomers to be isomeric; hence, the term spin isomer is used.

- Shape isomers:

  It has been found that different nuclear excitations can exhibit different shapes, and that changes in shape can result in hindered decays. There is a specific type of shape isomer called a super deformed isomer, in which the nucleus is highly elongated. These isomers occur in certain light and medium-mass nuclei and exhibit very high angular momentum. A further type of shape isomer is the fission isomer, in which a highly excited state undergoes spontaneous fission.

- K isomers:

  This type refers to a particular kind of isomer characterized by the K quantum number. The K quantum number is determined by the projection of the total angular momentum of a nucleus I onto the symmetry axis. An electromagnetic transition with a large change in K is associated with a long half-life of a state. For prolate shape nuclei, K isomers dominate in the mid-to-upper shell regions, particularly when both protons and neutrons occupy these regions at the same time.

- Seniority isomers:

  Seniority isomers represent a specific type of spin isomers. A high-j single particle orbital containing two identical nucleons is the simplest and most predictable case for the seniority isomers $v = 2$. These configurations form even-spin states with spins between $I = 0$ and $I = 2j - 1$. As a result of the short range of residual interaction, in the case of high-j orbitals the energy gap between the highest spin $2j - 1$ and

$2j-3$ states is small, leading to isomeric states decaying by $E2$ transitions with a lifetime typically between 10 ns and 100 μs [20]. The presence of seniority isomers is common in the chart of nuclides. As one moves away from semi-magic nuclei and as seniority increases, their properties become more unpredictable. The lifetime of these states depends on the order in which they are excited and on how their wave functions are mixed. Consequently, parabolic behaviour is expected for the reduced transition probability $B(E2)$ as a function of the number of particles on the j orbital.

These additional categories provide further insights into nuclear isomers' diverse behaviors and properties. The study of these isomers continues to be an active area of research in nuclear physics, as they offer a variety of fascinating phenomena for investigation and possible applications.

2.7 Interaction of Radiation

Radiation detectors work based on how the radiation that is to be detected interacts with the detector's material. Thus, it is necessary to understand the fundamental mechanisms by which radiation interacts with matter and loses its energy in order to understand the response of a particular type of detector. In terms of detection systems, we can classify radiation into two categories: ionizing radiation, including heavy ions, alpha and beta particles, and uncharged radiation, including neutrons and gamma rays.

2.7.1 Heavy charged particle interactions

The interactions between heavy charged particles and matter are mainly caused by Coulomb forces between their charge and the negative charge of orbital electrons in the absorbing atoms. Despite the fact that charged particles may also interact with nuclei, these interactions are not common and are unlikely to greatly affect radiation detectors' responses, which rely heavily on electron interactions.

Any charged particle that enters an absorbing medium immediately interacts with a large number of electrons simultaneously. As the charged particle passes within the vicinity of

an electron, the electron feels an impulse from the coulomb force. Depending on how close the encounter is, this impulse may be sufficient to either excite or ionize the electron within the absorbing atom. By transferring energy to the electron, the charged particle's energy is reduced, causing its velocity to be decreased. It is estimated that in a single collision, approximately 2×10^{-3} of the particle's energy per nucleon can be transferred from a charged particle to an electron. Due to the fact that this represents only a fraction of the total energy of the particle, the charged particle must lose its energy over a number of interactions in order to be detected. Therefore, it continues to travel through the absorber and interact with their electrons, losing energy with each step until it is stopped. Different factors determine the rate of energy loss of a charged particle in a medium. The Bethe-Bloch formula is a mathematical description of the relationship between the mass and energy of a charged particle passing through matter [21], the formula can be written as;

$$-\frac{dE}{dx} = \left(\frac{e^2}{4\pi\varepsilon_0}\right)^2 \frac{4\pi z^2 N_A Z\rho}{mc^2\beta^2 A}\left[\ln\left(\frac{2m_e c^2\beta^2}{I}\right) - \ln\left(1-\beta^2\right) - \beta^2\right] \tag{2.31}$$

where $\beta c = v$ the velocity of the particle and z its proton number whereas Z, A and ρ are the, atomic number, mass and the density of the material it is moving through and $N_A = 6.022 \times 10^{23} mol^{-1}$ is Avogadro's number. The variable I is used to estimate the average ionization and excitation energies of the atoms in the medium. It can theoretically be calculated but is usually used as an empirical constant with the value $I = 10\,Z\,eV$. The energy loss per unit distance in silicon for different ions has been calculated using SRIM program, Stopping and Range of Ions in Matter [22], the results are shown in figure (2.8).

From the Bethe-Bloch formula, we can highlight some features for the interaction of charged particles in a matter;

- The amount of energy deposited decreases with a rise in the energy of the incident charged particle.

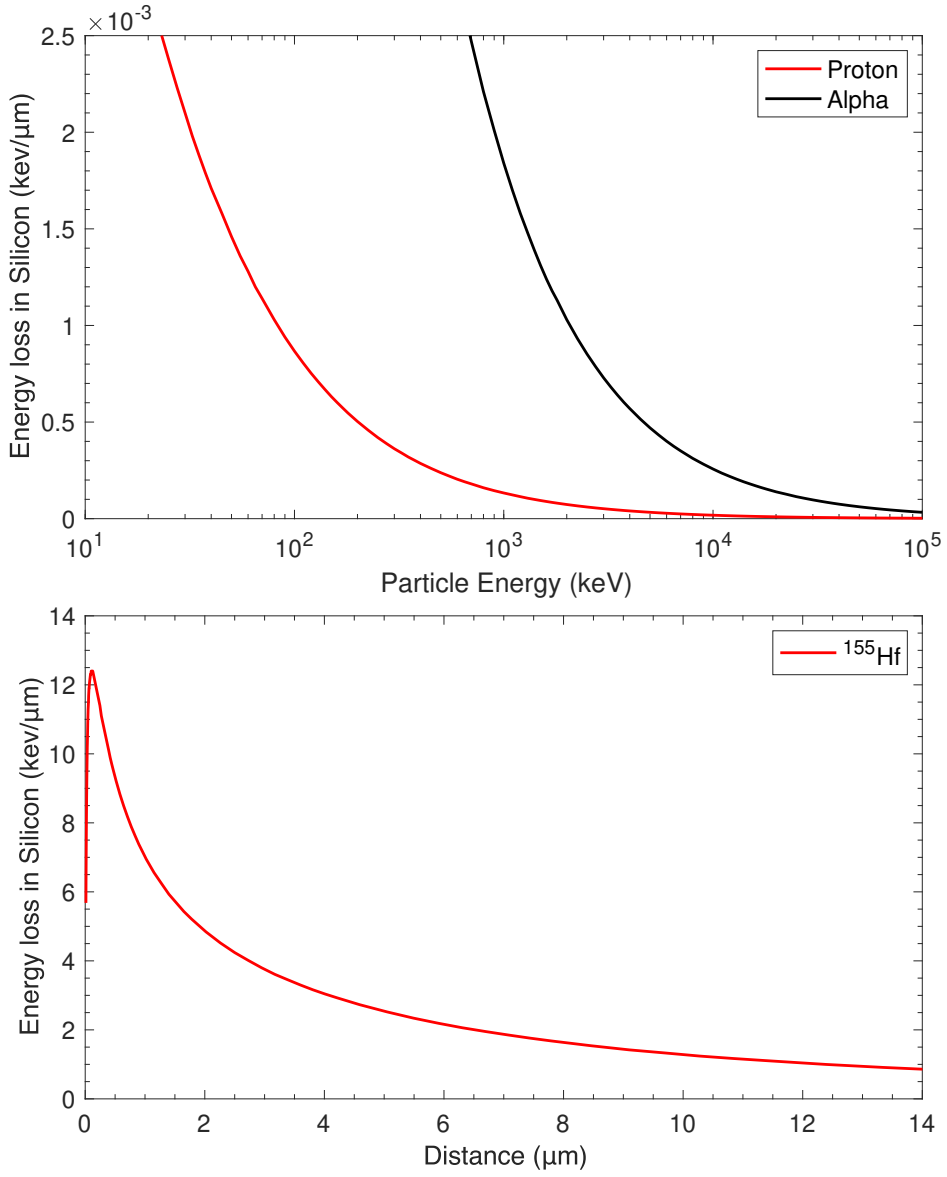

Fig. 2.8 A plot of the specific energy loss in silicon in relation to the energy of the charged particles (proton, alpha) in the top. The range of ^{155}Hf ion plot as a function of the specific energy loss in Silicon in the bottom. In each case values were calculated using SRIM [22].

- A high atomic number Z of the absorbtion medium increases the interaction probability and, consequently, the energy loss per unit distance.
- The range of the charged particles is also affected by the atomic number of the incident particle. Considering that light ions and heavy ions possess the same energy, the latter tend to stop within a few micrometers of the absorber.

2.7.2 Gamma ray interactions

It is known that gamma rays interact with matter through a wide variety of mechanisms, but only three major types have significant effects on radiation measurements: photoelectric absorption, Compton scattering, and pair production. A portion or all of the gamma-ray energy is converted into electron energy during all of these processes. As a result of these interactions, gamma-ray either vanishes or is scattered through a wide angle. This behaviour differs greatly from the behaviour of charged particles, which slow down steadily through continuous interactions with atomic electrons of the absorber. The energy of the incident gamma ray is the main factor determining which of these interactions will take place. As a function of absorber atomic number, the left line in figure (2.9) indicates the energy at which photoelectric absorption and Compton scattering have equal probability. While the right line shows the energy at which pair production and Compton scattering have equal chances of occurring.

Photoelectric absorption

The photoelectric absorption process occurs when a photon interacts with a medium atom, resulting in the complete disappearance of the photon and the emission of an energetic photo-electrons from an atom's bound electronic shells. A photo electron will most commonly be generated by the atom's most bound shell, K shell, if gamma rays have sufficient energy. If E_b is the electron's binding energy and E_γ is the energy of the incident gamma ray, then the

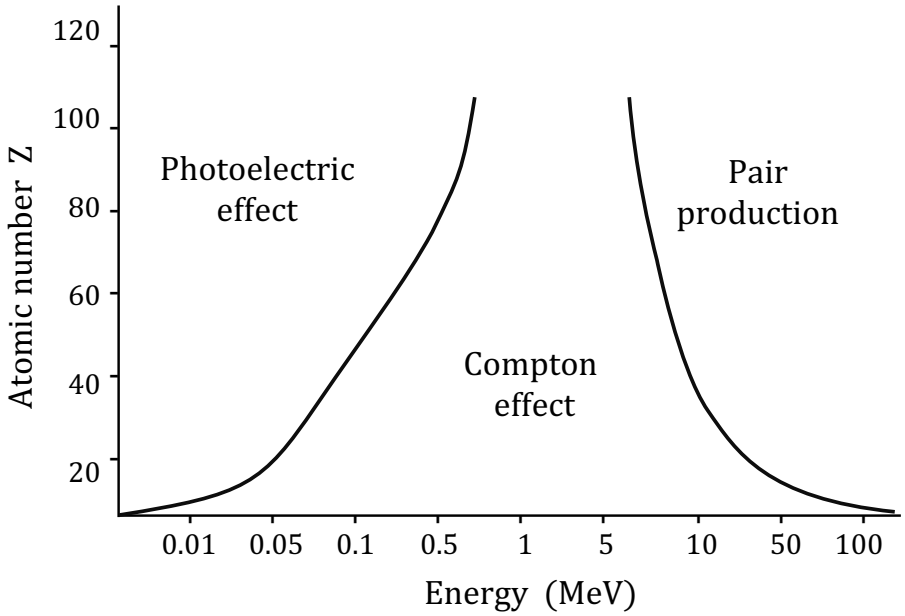

Fig. 2.9 The mechanism of gamma-ray interactions, photoelectric absorption, Compton scattering, and pair production are illustrated in relation to the absorber's atomic number and the energy of gamma ray. The sketch was derived from reference [23].

photo electron's energy can be written as follows;

$$E_e = E_\gamma - E_b \tag{2.32}$$

When gamma-ray energies are less than 100 keV, the photo-electron of a germanium detector ($Z = 32$), for example, carries most of the photon energy away due to the high interaction probability. As a result of the ejection of the electron, an ionized absorber atom is created behind it with an electron vacancy in one of its bound shells. One or more characteristic X-ray photons may also be generated through the transfer of electrons from higher shells of the atom to fill the hole. A secondary photoelectric absorption process may take place involves less tightly bound electrons and absorb these X rays. An Auger electron may, in some cases, replace the characteristic X-ray emission as a means of removing the excitation energy. In the case of gamma rays of relatively low energy, the photoelectric process is the most common method of interaction. In addition, the photoelectric process is more effective

when the gamma rays interact with a material with higher atomic number. Based on the energy of the gamma ray and the detection material's atomic number, the probability of this process taking place can be estimated as follows

$$P \propto \frac{Z_{\gamma}^{3.5}}{E^{n}} \tag{2.33}$$

Over the region of gamma-ray energy of interest, n is a constant that vary from 4 to 5.

Compton scattering

Compton scattering process occurs when an incident gamma-ray interacts with an atomic electron in the absorbing material. This interaction results in knockout of an atomic electron "recoil electron" as well as deflection of the traveling gamma ray. The angle θ at which gamma ray is diverted by can vary from zero to 180° relative to its original direction based on the amount of energy transferred to the electron. The large scattering angle indicates that the incident gamma ray lost a large amount of energy to the electron. Based on the conservation of energy and momentum laws, the scattered gamma ray's energy $E_{\gamma}^{'}$ can be expressed as follows;

$$E_{\gamma}^{'} = \frac{E_{\gamma}}{1 + \frac{E_{\gamma}}{m_e c^2}(1 - cos\theta)} \tag{2.34}$$

Typically, Compton scattering is the dominant interaction process, especially for gamma-ray energies above $100\,keV$ and up to $6,000\,keV$ in a germanium detector. Since it covers a large range of the most common gamma ray energies, the features of this reaction process can be easily seen in the energy spectrum. As there are no restrictions on the scattering angle, some of the incident gamma energy will not be fully absorbed, contributing to the rise of the background, and this background is known as the Compton continuum. Furthermore, a backscattering peak may also appear as a result of the interaction between gamma ray and the surroundings materials of the absorbing medium. Similarly, the interaction mechanism contributes to the emission of X-rays in the same manner as described in the previous section.

Pair production

In the pair production process, the gamma-ray photon disappears when it passes close to the coulomb field of a nucleus and contributes to the production of an electron-positron pair. In order to satisfy the conservation of energy law, the energy of the incident photon must be at least equal to the rest-mass energy of the emitted electron and positron $(2 \times 511\ keV)$. Any excess energy that the photon brings in above the $1.02\ MeV$ will be converted into kinetic energy that is shared between the electron and positron. As a consequence, this type of reaction can only occur if the gamma-ray energy is greater than twice the rest-mass energy of an electron, or it will not occur. Due to this, the probability of gamma-ray interactions through pair production is significant when the energy of the gamma ray is between 5 and $100\ MeV$, a range that is irrelevant to nuclear structure studies.

The emitted positron interacts with atomic electrons in the medium and loses some of its energy as a result. Eventually, it encounters an electron and both disappear and are replaced by two $511\ keV$ photons called annihilation radiations. Depending on the size of the detector, either one or both of these can escape, resulting in an escape peak in the gamma ray spectrum equal to the energy of the gamma ray minus either $511\ keV$ or $1022\ keV$ for single or double-escape peak respectively.

Chapter 3

Experimental Methodology and Apparatus

3.1 Fusion-evaporation Reaction

An artificial production of nuclei is required to study the structure of nuclides that lie in the neutron-deficient region and near the proton drip line. The heavy-ion fusion-evaporation reaction is the most common method to have been used in experiments to produce the nuclei of interest. The result of this reaction is a compound nucleus that is formed when heavy and light nuclei are fused together. As a target, the heavy nuclei are usually used, whereas the light nuclei are used as the high energy incident beam. It is necessary for the beam to be energetic enough to overcome the Coulomb barrier between the incident particle and the target. The beam and the target will fuse only if the energy of the beam is greater than the calculated energy of the Coulomb barrier E_C from the following equation:

$$E_C \approx \frac{Z_B Z_T}{A_B^{1/3} + A_T^{1/3}} \tag{3.1}$$

where Z_B represents the beam atomic number, Z_T represents the target atomic number, A_B represents the beam particle's atomic mass, and A_T represents the target's atomic mass [24].

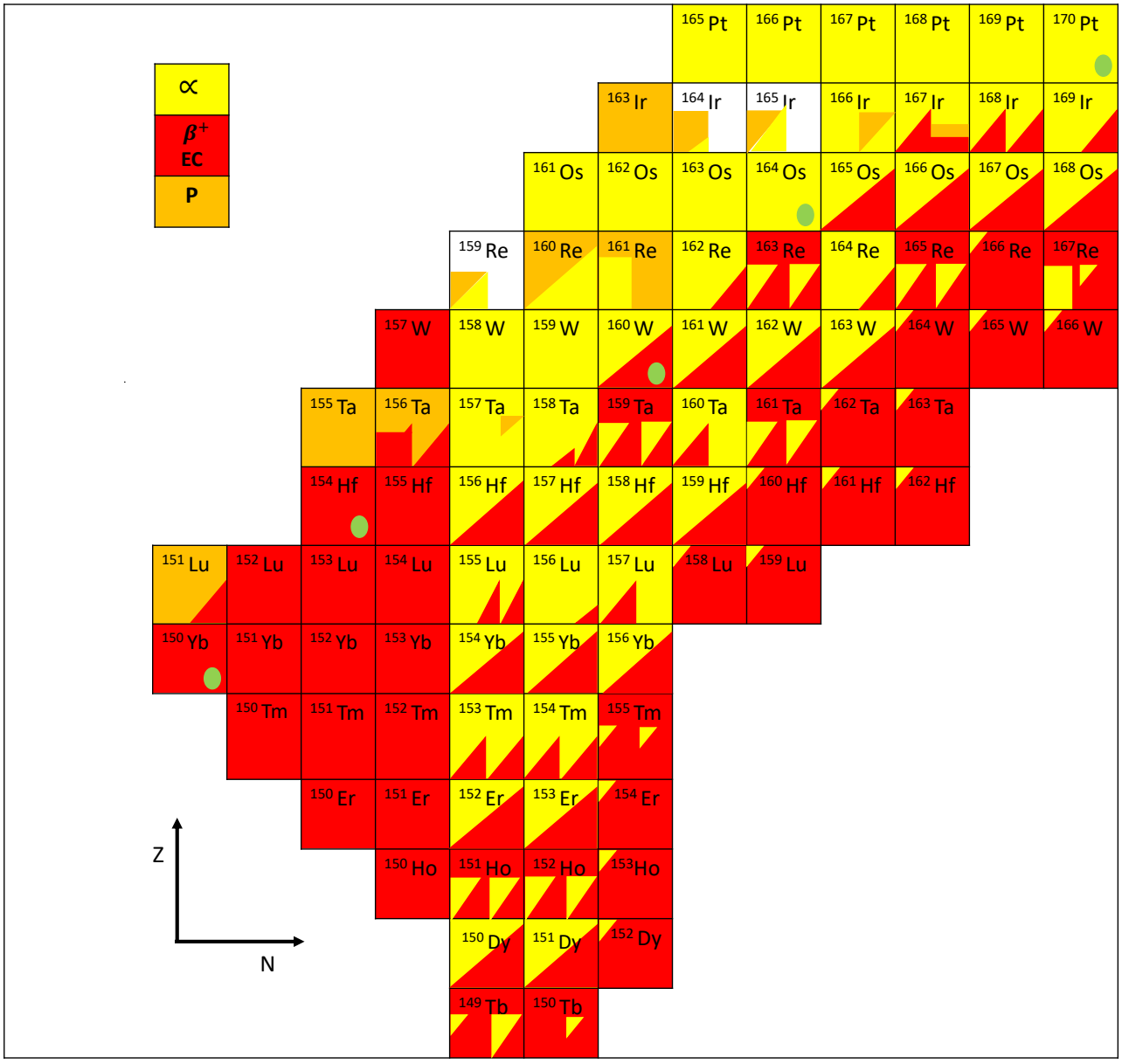

Fig. 3.1 The region of interest of the nuclear chart the colours (yellow, red and orange) represent the decay modes while the green filled circles indicate the compound nuclides formed in this work.

The reaction described here is a two-phase reaction, and the intermediate state prior to the start of particle evaporation is what is known as a compound nucleus; the reaction between the beam (B) and the target (T) is expressed as follows:

$$B + T \rightarrow {}^{A_B+A_T}_{Z_B+Z_T}C^* \rightarrow R + nL \tag{3.2}$$

Where R represents a recoil nucleus and L represents a light particle such as a proton, neutron, or alpha particle. It is possible for the compound nuclei to evaporate one or more light particles. Here n represents the number of evaporated particles. In heavy neutron-deficient nuclei, there is a significant possibility of fission following the fusion of the beam and the target nuclei. Consequently, a large gamma-ray background is introduced, which blurs gamma-ray transitions from the desired reaction channel. It is also possible to write the expression in equation (3.2) as $T(B,nL)R$.

Mainly, the beam energy determines how likely it is to produce the nuclei that are being studied. Through the calculation of fusion evaporation cross sections, a number of reaction simulation programs, including PACE4, HIVAP, and CASCADE, can be used to determine suitable reaction parameters for producing a specific nucleus. An illustration of the chart of nuclides showing neutron-deficient nuclei in the region of Z between 65 and 78 is shown in figure (3.1). As long as the compound nucleus is the same, all the evaporation channels are possible, regardless of the choice of reactants. Figure (3.2) shows the cross section of proton-rich nuclei produced by fusion-evaporation reactions of a ^{58}Ni beam on a ^{102}Pd target. Furthermore, ^{155}Hf can also be produced using different combinations of beam and target, such as ^{54}Fe on a ^{106}Cd target, and ^{64}Zn on a ^{96}Ru target, from evaporation of two protons and three neutrons of ^{160}W compound nucleus. Also shown in the figure is the calculated cross section for these reactions. It can be seen from the figure that the cross section value of ^{155}Hf is relatively the same for all three reactions. Therefore, it is a matter of availability of the target.

Accordingly, to study nuclei in this region, a highly energetic light beam, usually between 200 MeV and 400 MeV, is bombarded onto a heavy thick target to fuse the two nuclei,

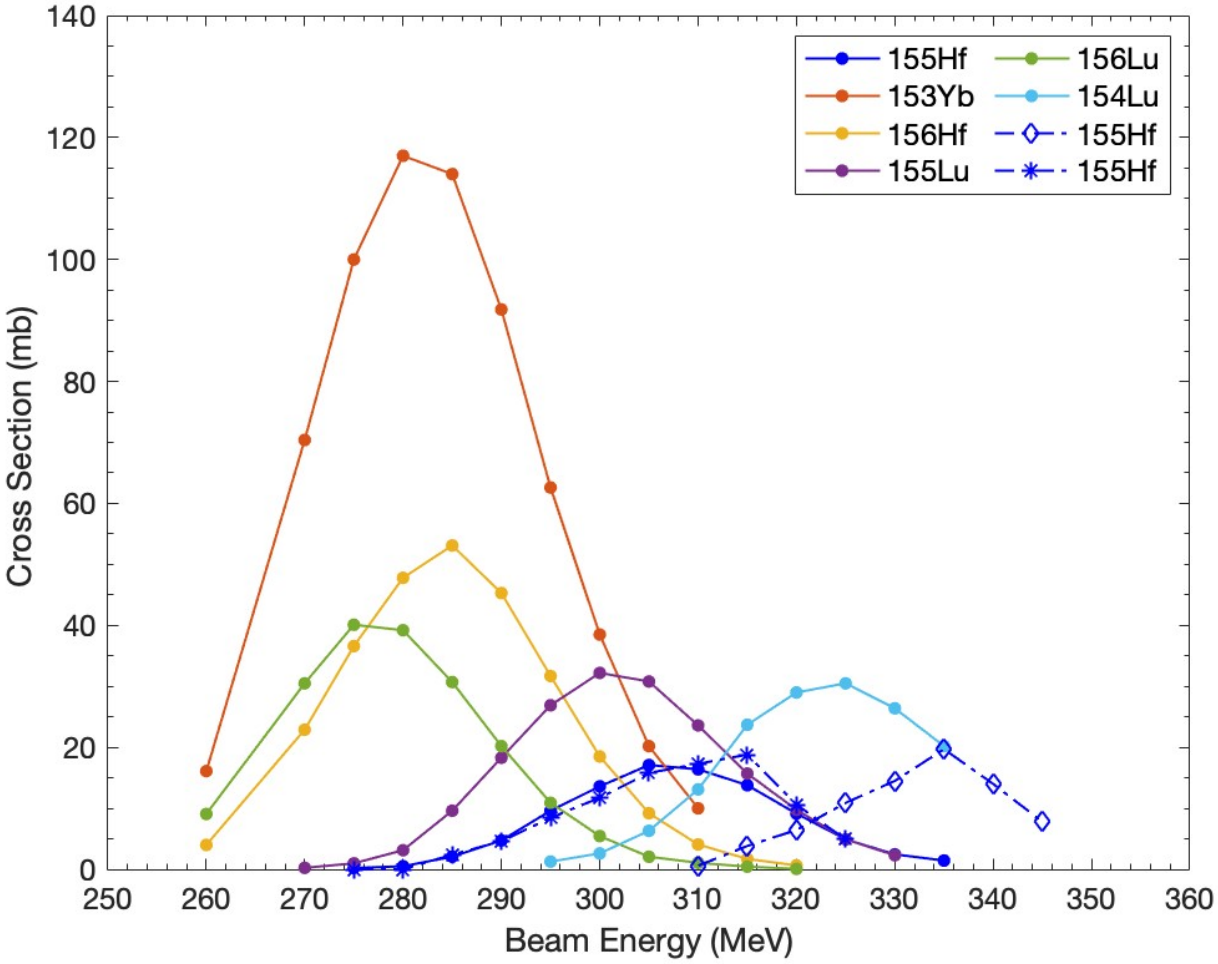

Fig. 3.2 The cross sections obtained with a ^{58}Ni beam on a ^{102}Pd target computed using PACE4 as a function of the beam energy for highly neutron-deficient nuclides produced through fusion evaporation reactions. The dash-dotted lines represent the cross sections produced with a ^{54}Fe beam on a ^{106}Cd target and ^{64}Zn beam on a ^{96}Ru target with diamond and asterisk markers respectively.

resulting in the formation of a compound nucleus with a high angular momentum excited state. At this stage, particles can be emitted until the excitation energy of the compound nucleus falls below the particle-evaporation threshold. At this point, the compound nucleus will be referred to as evaporation residue. Due to the fact the evaporating residue is still extremely excited, two steps of gamma-ray emission are occurring. Initially, it emits a statistical gamma-ray cascade until approaching the yrast line at which point a second type of gamma is emitted. In contrast to statistical gamma cascades, these are very useful for studies of nuclear structure and are sometimes referred to as structural gamma cascades. At the end when there is no energy to be emitted, the nucleus reaches its ground state after $10^{-9}s$ from the fusion. The time scale and stages of the reaction are shown in figure (3.3).

3.2 Beam and Targets

In order to determine which nuclides to use for the beam and target, it is necessary to determine what properties will be investigated and where in the nuclear chart the nuclei of interest are located. The heavy neutron-deficient nuclei in the $N \approx 83$ region are commonly produced by initiating fusion-evaporation reactions using highly charged, high-energy beams. The experiments in this work were conducted at the Accelerator Laboratory of the University of Jyväskylä. In the laboratory, there are three accelerators; the K130 cyclotron, the MCC30/15 cyclotron and the 1.7 MV Pelletron. This work was carried out using the K130 cyclotron, which is an isochronous type cyclotron equipped with three external electron cyclotron resonance (ECR) ion sources. This cyclotron can deliver stable heavy-ion beams with energies of 130 $Q^2/A\ MeV$ [25], where Q is the charge state of the produced ion and A its mass number. In order to produce an effective reaction, the state and thickness of the target are crucial factors. Since the purpose of this work is to explore the nuclear structure and decay properties of nuclei, the focus is on the recoiling nuclei instead of the outgoing light particles. For this reason, a solid thick target is recommended to increase the interaction probability and thus the production rate as there is no concern that light particles will be degraded or stopped

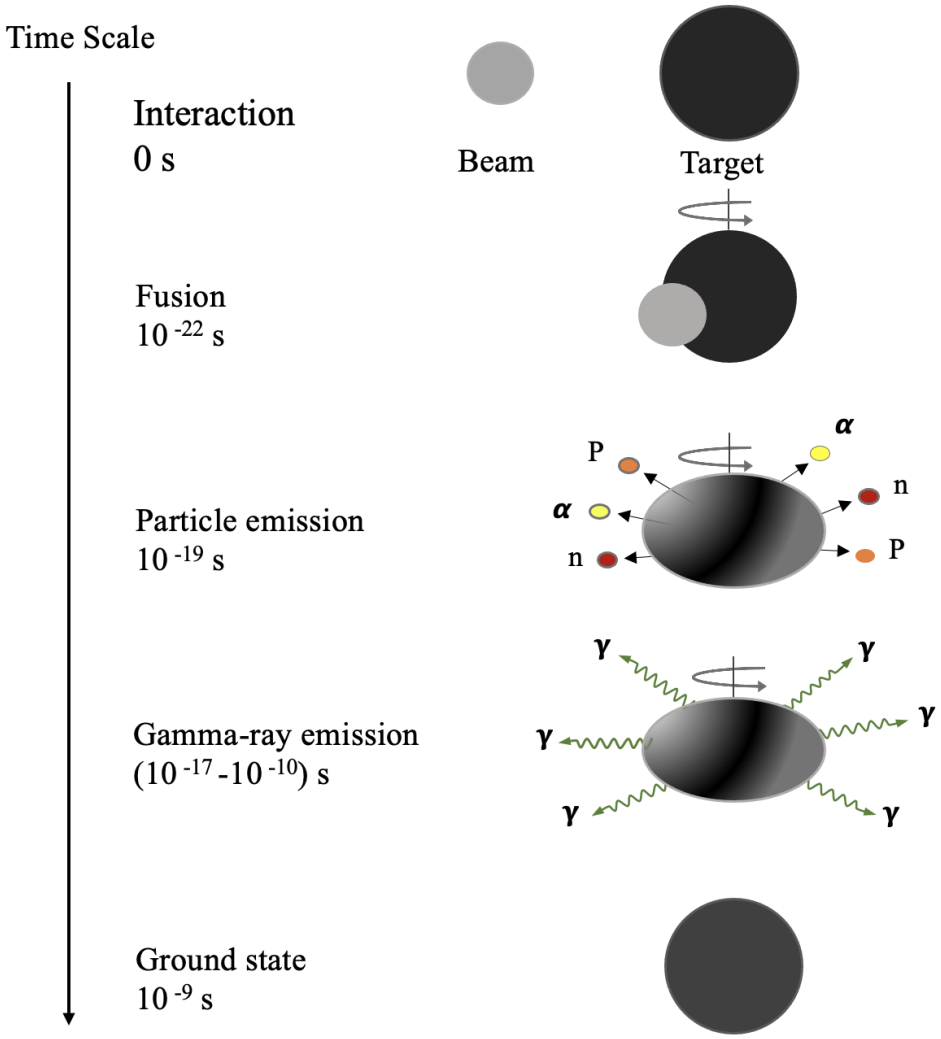

Fig. 3.3 An illustration of the decay time scale of the compound nucleus following fusion-evaporation reaction.

Table 3.1 Specifications for the beam and targets used in the experiments.

Data Set	Beam	Beam Energy (MeV)	Target	Target Thickness $(\mu g\ /cm^2)$	Irradiation time (h)	Average Beam Intensity(pnA)
A	$^{58}_{28}Ni$	295	$^{102}_{46}Pd$	1000	118.03	3 to 5
		315			155.11	5
B		293			21.57	7
		275			47.06	5

during this process. If the energy or scattering angle of the light particles is an important factor for the study, it may be beneficial to use a thin target.

It is necessary to take into account equations (3.2) and the production cross section, figure (3.2), in addition to other factors such as the availability, efficiency, and the accessibility of the reactants when executing a heavy ion fusion-evaporation reaction. Theoretically, there were three options for the combination between the beam and target elements that will lead to the ^{160}W compound nucleus. However, when the experiments were running, it was decided to use ^{102}Pd as a target since other objectives were being pursued. Among these options, ^{102}Pd was the most suitable choice. As illustrated in figure (3.2), whichever choice is made, it will have no effect on the production of ^{155}Hf nuclei.

An accelerated ^{58}Ni (12^+) beam was generated in both experiments with beam energy between 275 to 315 MeV and delivered to interact with an enriched ^{102}Pd target of thickness $\sim 1\ mg\ cm^{-2}$. The details of the beams and the targets are provided in the table 3.1.

3.2.1 The target chamber

The target chamber is the first component of the experimental setup, located in the beam direction and connected to the MARA separator. It is an evacuated aluminium chamber equipped with a wheel capable of holding a maximum of six different targets. Its rotation can be controlled from outside, thus making it possible to change targets during an experiment without opening and then evacuating the chamber each time.

The chamber may also include two carbon foils, one of which may be used as a degrader foil

to reduce the energy of the beam by a tiny amount, less than 800 keV, when this reduction is not possible for the accelerator operator to achieve. Because of this, it is placed at the entrance of the beam and acts as a tuning device before the reaction takes place.

A carbon foil can also be placed behind the target wheel so that the recoils pass through it; in this case, the carbon foil serves as a device for resetting the ionic charge state of evaporation residues and is known as a reset foil. In the event that an isomer is present and decays before the carbon foil, a high charge distribution caused by the Auger cascade will be reset at the carbon foil. Analysing the charge distribution and noticing the anomalous charge distribution before and after the carbon foil reveals evidence regarding the lifetime of the recoil's isomeric states. However, this work is not concerned with this. The aim of using carbon foil is only to ensure that the charge state is reset after the decay of any short-lived isomers.

One last element that may be added to the target chamber is the JYU Tube detector. It is a charged particle detector that is placed downstream and upstream of targets; details about its structure and applications will be discussed in the detection section. An image of the target chamber is shown in figure (3.4).

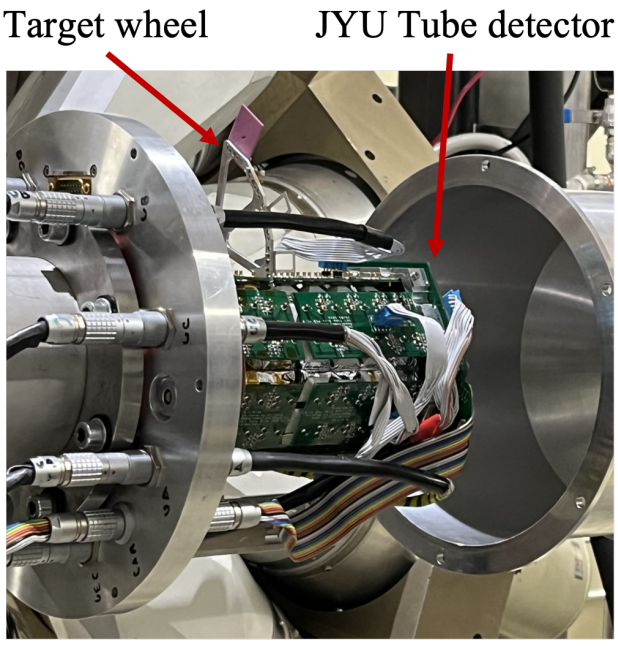

Fig. 3.4 Photograph of the target chamber, in which the wheel holding the targets and the JYU Tube detector are visible.

3.3 The MARA Vacuum-mode Mass Separator

The fusion-evaporation reaction produces a variety of reaction products as well as some residual beam material that passes through with the reaction products. To conduct any kind of decay spectroscopy analysis, it is necessary to design an appropriate separation setup in order to eliminate the beam residues and select only the nuclides that are of interest. At JYFL's Accelerator Laboratory, two different types of separators are available: RITU the Recoil Ion Transport Unit and MARA the Mass Analysing Recoil Apparatus [26]. RITU consists of four principal parts (QM_DQQ) which provide the required segregation. Three of these are quadrupole magnets and the fourth is a dipole magnet. Unlike RITU, MARA has one additional component for its separation system, which is the electrical dipole.

It is more efficient to use RITU for heavy and super-heavy nuclei with, as the transport efficiency of both separators is affected by the mass number of the passing ions [27]. Separation method is another factor that influences the choice of the separator. RITU, for instance, is a gas-filled separator usually filled with helium, and one of the advantages of fusion evaporation is that it produces nuclei with different charge states, so if it is decided to use the mass to charge ratio to get better results in the separation, then the gas would be an obstacle to overcome. Recoils interact with the gas particles, resulting in scattering of the ions, which results in a loss of information regarding mass to charge ratio.

Due to the fact that this work focuses on proton-rich nuclei in the $N \approx Z$ region, it is anticipated a low yield, which is why the MARA separator has been used [28]. It is a vacuum mode recoil separator of 6.85 m length along the optical axis, with transport efficiency between 20% and 40% [29] and angular acceptance up to 45 $mrad$ and 55 $mrad$ for the horizontal and vertical axes, respectively [27]. It is also configured with an ion-optical configuration of $QQQE_DM_D$, as shown in Figure (3.5). The main principle of separation is based on Lorentz force, equation (3.3), which describes the force applied to a charged particle q moving

through a magnetic field B and an electric field E with velocity v as follows:

$$\vec{F} = q(\vec{E} + (\vec{v} \times \vec{B})) \tag{3.3}$$

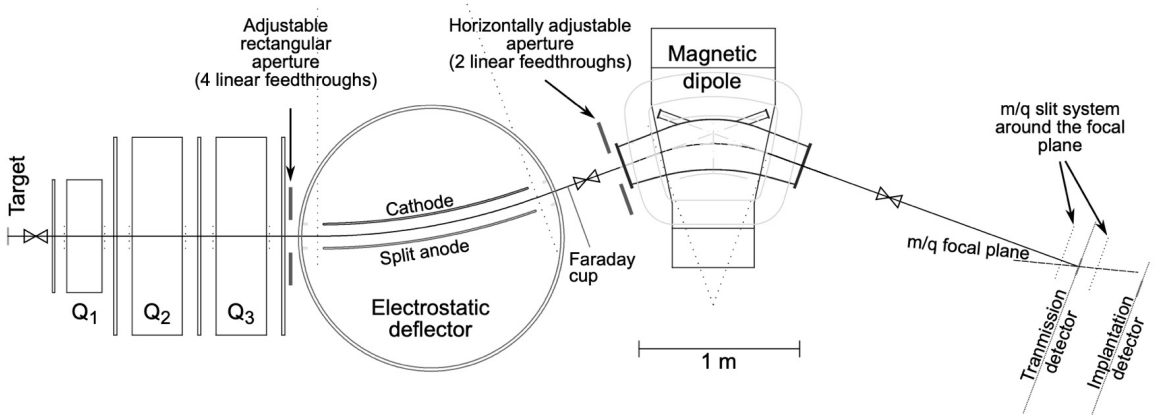

Fig. 3.5 The main ion-optical components of MARA, the vacuum-mode recoil separator, the target position and some of focal plane detectors are also shown [27].

3.3.1 Quadruple triplet

The quadruple triplet is located between the target chamber and the electrostatic deflector, as shown in figure (3.5). The first quadruple magnet has a 10 *cm* bore diameter, while the two after it have a 15 *cm* bore diameter. As a result of the nature of the reaction, the recoils are emitted in all directions, so to obtain the maximum number of nuclei, the quadruple triplet is used. The first $Q1$ and third $Q3$ quadruples are used for horizontal focusing and vertical de-focusing, while the second quadruple $Q2$ is used for horizontal de-focusing and vertical focusing of the recoils. Figure (3.6) illustrates the paths followed by the recoils from the moment they are emitted from the target chamber to the moment they reach the focal plane. While figure (3.7) is shown an image of the actual quadruple triplet.

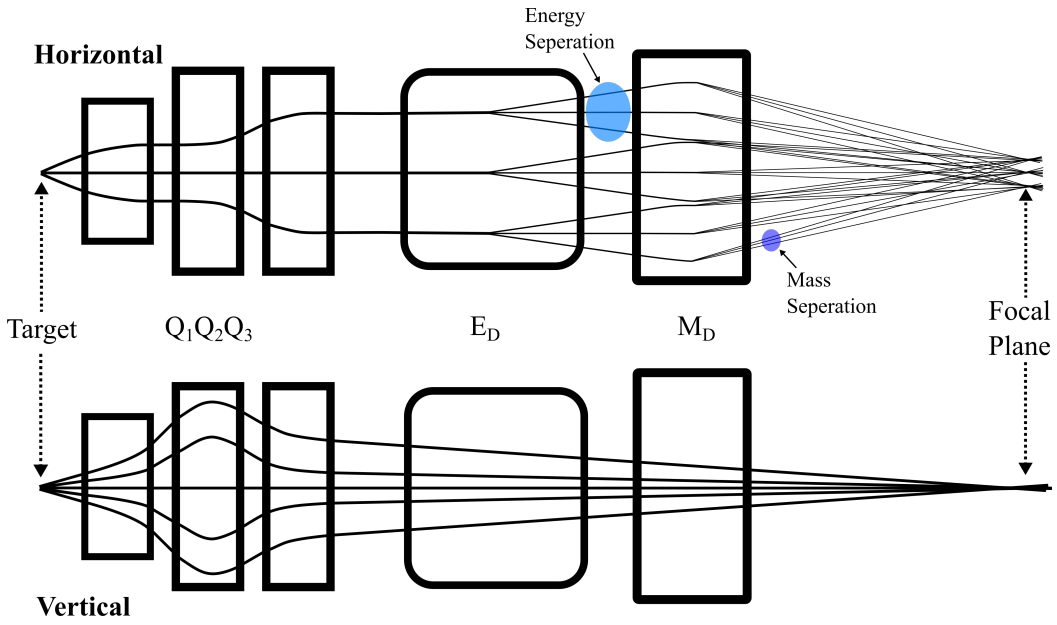

Fig. 3.6 An illustration of the separation principles applied by MARA. Solid lines depict the general route that evaporation residue of a given mass, kinetic energy, and charged state takes through the separator [9].

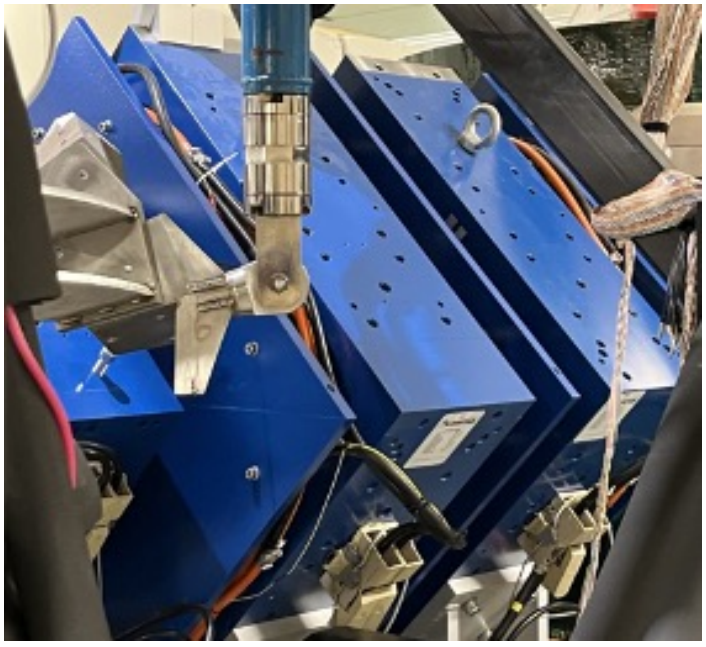

Fig. 3.7 An image of MARA's quadruple triplet.

3.3.2 Electric dipole

MARA's electrical dipole consists of two titanium plates positioned at a distance of 14 *cm* from one another with a curvature radius of 400 *cm*. A photograph of the electrical dipole is shown in figure (3.8). The purpose of the dipole is to perform a kind of filtering of the components that are delivered from the quadruple triplet, which will enable us to distinguish the recoils from the unreacted beam. To create the electric field, a maximum voltage of $\pm 250\,kV$ can be applied to the plates. As a result of the electric field, the ion beam and the recoils will deflect from their original trajectories, therefore the term electrostatic deflector is also used to describe the electrical dipole. There is a difference in deviation level between beams and recoils, which is influenced by the degree of electrical rigidity. It is possible to describe the electric rigidity χ_E of a charge particle q moving with a velocity v in an electric field E with curvature radius r_d in terms of how much it resists the deviation direction caused by Lorentz force. It is clear from the following equation that the momentum p, as well as the kinetic energy E_k of the particle, have the greatest effect on the rigidity value:

$$\chi_E = E r_d = \frac{pv}{q} = \frac{2E_k}{q} \tag{3.4}$$

Suitable electric fields are set to allow the unreacted beam to pass through a small gap in the anode of approximately 1.5 *cm* width , while the recoils continue to travel to the magnetic dipole.

3.3.3 Magnetic dipole

One of the primary components of a MARA separator is the magnetic dipole, which consists of two poles separated by 10 *cm* from each other and with a curvature radius r of 100 *cm* and a maximum magnetic field of 1 T. The effect of the magnetic field on a charge particle q of mass m and velocity v passing through a magnetic field B can be seen as a change in the path of the charge particle. The charge particle will follow a circular path. The radius r of this

Fig. 3.8 A picture of the electrical dipole which is located behind the quadruple triplet.

path is indicated by the following equation:

$$r = \frac{m\,v}{q\,B} \tag{3.5}$$

As with the charge particle in the electric deflector, the motion of the particle in the magnetic dipole can be described by the magnetic rigidity as follows;

$$\chi_B = B\,r = \frac{p}{q} = \frac{\sqrt{2\,E_k\,m}}{q} \tag{3.6}$$

Where χ_B is the magnetic rigidity, q is the particle's charge, E_k is its kinetic energy, and m and p are its mass and momentum, respectively. The magnetic dipole works in harmony with the electric dipole in order to achieve the best results in the separation. In choosing an appropriate value for the electric and magnetic fields in the deflectors, the energy dispersion can be eliminated completely. In this case, the amount of separation is completely determined by the mass to charge ratio m/q.

3.3.4 Focal plane

In the experimental setup, the focal plane is the last component, located just behind the MARA separator on the right side of the figure(3.5). The fusion-evaporation reaction products are detected here after the separation process has been completed. Separator parameters, such as angular acceptance, energy acceptance, and dispersion, can be adjusted to obtain the maximum transition rate for the nuclei of interest. At the focal plane, a variety of detectors may be used depending on the type of measurements being undertaken. A combination of charged-particle and electromagnetic radiation detectors are used, each of which has a different detection efficiency. Some detectors are dedicated to measuring low-energy radiations while others are better suited to detecting higher energy radiations depending on the type of radiation, the atomic number of the absorber and the detector volume. A photograph of how the germanium detectors are arranged around the chamber, in experiment A, can be found in (3.9, A) and a graphical representation of the focal plane detector inside the vacuum chamber can be found in figure (B). A detailed information about the detectors used in this study is provided in the following section.

3.4 Electromagnetic and Charged Particle Detection

3.4.1 Semiconductor detectors

A semiconductor detector is a solid-state detector made of semiconductor material that can detect ionising radiation. A distinguishing characteristic of these materials is that they have an intermediate band gap, between those of insulators and conductors. Materials are composed of atoms arranged in a crystal structure. The electrons in the outer shell of these atoms are responsible for determining the conductivity of the material. When electrons are free to move, they are capable of conducting electricity. On the other hand, if their movement is restricted, they are unable to conduct electricity. In terms of conductivity, materials can be characterised by examining how the energy levels are arranged in bands.

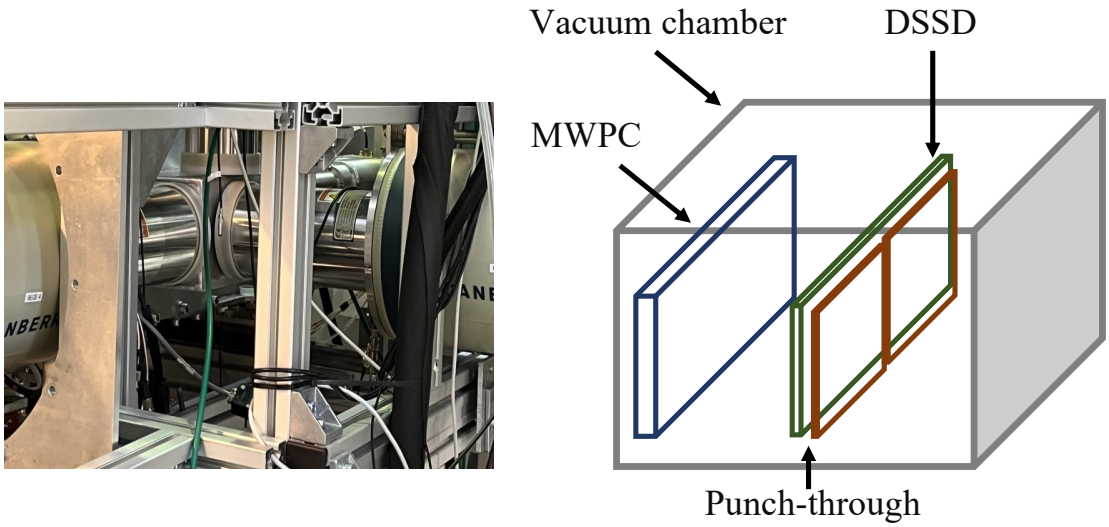

(A) (B)

Fig. 3.9 (A), An image of the germanium detectors arranged around the vacuum chamber at the focal plane of MARA in experiment A. (B) a sketch of the focal plane detector inside the vacuum chamber.

There are two bands that affect conductivity, namely the valence band and the conduction band. When the electrons are situated in the valence band, they are not free to move around, and therefore do not contribute to the flow of electricity. In contrast, if they are found to be in the conduction band, then they are free to move, and they participate in the process of conductivity. An energy gap between the valence and conduction bands in insulators is greater than 5 eV, also known as the forbidden gap or band gap. The gap prevents electrons from moving from the valence band to the conduction empty band. However, the contrast occurs in conductors where the two bands are actually overlapping [23].

In semiconductors, the band gap is small, about 1 eV, therefore valence electrons are able to jump into the conduction band if they gain sufficient energy. Thermal excitation is enough to provide this energy. When the electron leaves its place in the valence band, a hole is created. The combination of the two is known as an electron-hole pair. When an electric field is applied, each of the two pairs will drift towards the opposite pole, contributing to the material's electrical conductivity. The probability of creating an electron-hole pair $P(T)$ by

gaining thermal energy from the crystal is;

$$P(T) = C\,T^{3/2}\,e^{\left(-\frac{E_g}{2kT}\right)} \tag{3.7}$$

Where k is the Boltzmann constant, T is the absolute temperature, E_g is the band gap energy, and C is a material-specific constant.

In order to use semiconductors such as silicon (Si) or germanium (Ge) in radiation detection, a doping process is required. Doping refers to the process of creating an impurity within the crystal structure of a semiconductor material, commonly phosphorus (P) and boron (B) are used in trace amounts. By substituting one of the semiconductor covalent bond atoms with phosphorus atoms that have 5 valence electrons, an additional weakly bound electron will be produced. These electrons will lie at a level near the conduction band, also known as the donor level. In this case, the semiconductor is referred to as n-type. In equation (3.7), it can be seen that the probability of producing electron-hole pairs increases as the value of E_g decreases. A second type of extrinsic semiconductor is the p-type, in which the impurity is formed by boron, for example, which has 3 valence electrons. Contrary to the n-type, where electrons are the primary charge carriers, here the nearest electron from a neighboring atom will fill the hole created by the covalent bond of the boron atom. The electron leaves a hole in its place, which is filled by another electron. Thus, the charge carriers are the holes and the acceptor level is formed. In figure (3.10), the doping process in n-type and p-type semiconductors is shown, along with how it affects electron band structure.

In detectors, p-n junctions are created by doping a semiconductor material in a way that produces both n and p types within the same crystal structure. As a result of the interaction between the electrons from the n-type and the holes from the p-type, a small neutral region appears in the contact area of the two types. There are no charge carriers in this area, which is why it is referred to as the depletion region. In the depletion region, the radiation is detected, however it must be expanded first, and this is accomplished by applying a reverse bias to the p-n junction.

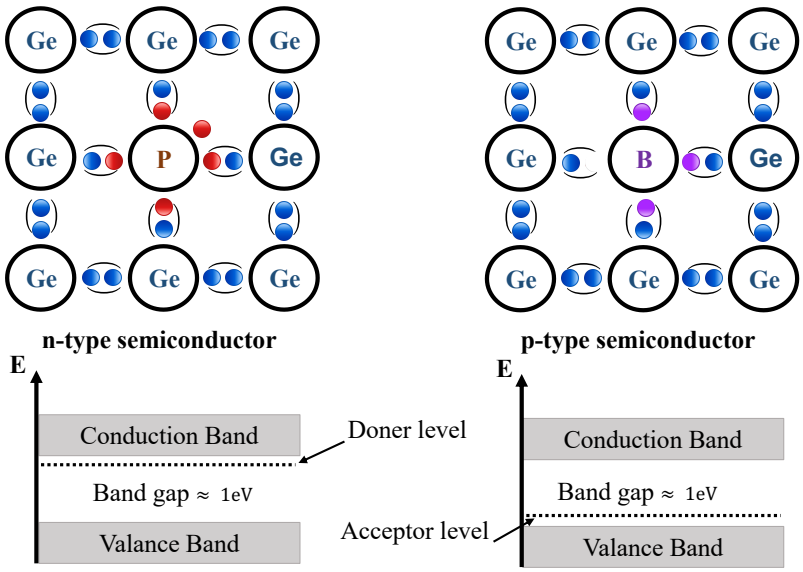

Fig. 3.10 An illustration of how doping affects the electron band structure in n-type and p-type semiconductors.

As radiation passes through the depletion region, electron-hole pairs are formed as a result of the interaction between the radiation and the detector materials. The electron-hole pairs are then collected by the attached electronics. The electric pulse is proportional to the number of electron-hole pairs, which represents the radiation deposited energy. The amount of energy required to create an electron hole pair is extremely low, approximately 2.96 eV in germanium at temperature of 77 K and about 3.62 eV in silicon at 300 K [30]. The electron-hole creation energy in comparison with the energy of a typical alpha particle ranged from 4 to 9 MeV indicates that a large number of pairs is generated. This feature gives this type of detector a significant advantage over other types in terms of resolution. A semiconductor detector is capable of detecting a very low energy particle and distinguishing between the energies of two particles which are quite close to each other. In addition, the solid state of semiconductors makes them more compact and smaller than gas detectors, for example. In this experiment, various types of semiconductor detectors have been used to detect alpha particles and gamma rays, each of which is described below.

Double sided silicon strip detector

The Double-Sided Silicon Strip Detector (DSSD) used in this experiment had a thickness of 303 μm and consisted of $13,824$ pixels with 192 strips on the x axis and 72 strips on the y axis. A photograph of the DSSD is shown in figure (3.11). Each pixel was $0.67 \times 0.67\ mm^2$ [31]. The dimension of the detector was $52.21 \times 132.6\ mm^2$ with an active area of $48.21 \times 128.61\ mm^2$. The detector had an energy resolution of $\sim 30\ keV$ FWHM at $7390\ keV$. In order to preserve its performance and mitigate radiation damage, it was cooled to around -20 °C during the experiment. With the segmentation of the detector, high precision of position identification was possible, which resulted in the identification of the decay chain of nuclides and the subsequent accurate assignment of nuclides. Furthermore, as each event was time stamped, the decay properties of other well-known nuclides could be use to reduce the effects of random correlations. Moreover, the lifetime of an isomeric state was determined by correlating the event in the *DSSD* with gamma rays detected in the germanium detectors. It is also possible to distinguish between recoils and decays through the use of the time differences between the time stamps from the DSSD and MWPC.

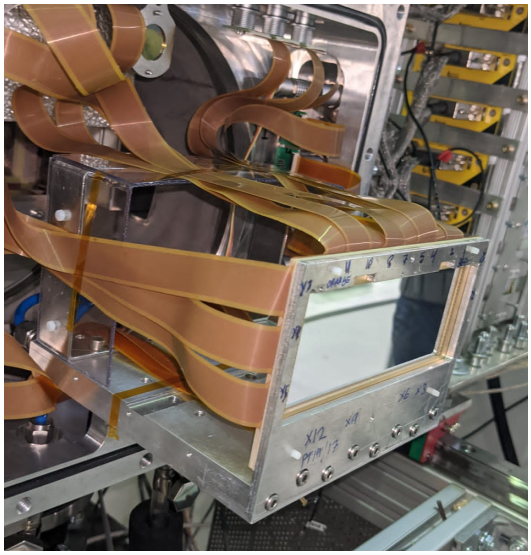

Fig. 3.11 An image of the DSSD installed at the focal plane, the external calibration source holder is also shown.

Punch-through detector

Another silicon type detector was placed just behind the Double-Sided Silicon Strip Detector. This detector consisted of two identical parts. It had a thickness of 1 *mm* and the same height and width as the DSSD. As the name implies, the primary function of this detector was to measure particles that would not be stopped by the 303 μm thick DSSD and pass through it. Most of these particles were either light particles, such as electrons, or highly energetic ions. In both cases, from the detected signals it was possible to improve the quality of the results by using the punch through detector as a veto detector. Figure (3.12) illustrates the installation of a punch-through detector at the back of the vacuum chamber at the focal plane of MARA.

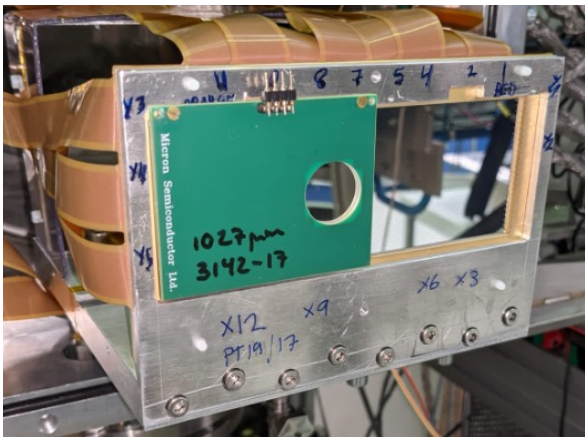

Fig. 3.12 Photograph of the Punch-through detector, also known as the Veto detector, installed just behind the DSSD at MARA's focal plane (only one part appears in the photograph).

The JUROGAM spectrometer array

In order to measure the energy and correlate the cascades of gamma rays that depopulate high-spin nuclear states with accuracy, an array of Ge detectors has been constructed. Using a large number of detectors maximizes the total photopeak efficiency of the germanium detectors, thereby improving the performance of the array. Another important aspect of array performance is the resolving power, which determines the quality of the spectrum. The value is an indication of the array's ability to distinguish one or more gamma-ray sequences in the

middle of a complicated spectrum containing thousands of gamma rays.

The JUROGAM Phase III array consists of 43 HPGe detectors that are spherically arranged around the target at fixed polar angles relative to the beam line. A total of 14 of these were used in this study "Phase I detectors" which were positioned mostly at a backward angle around the target. This resulted in a total coverage of 23% and a total photopeak efficiency of 5.6% for 1332 *keV* gamma rays. The Ge crystals had a length of 75 *mm* and a diameter of between 65 *mm* to 75 *mm*, with the first 30 *mm* millimeters tapered with a cone angle of 5.7°. The distance between the target and the front face of the Ge crystal was usually ranged between $\sim$ 20.5 *cm* and $\sim$ 22.4 *cm* [32].

Compton-suppression shields made of bismuth germanate (BGO) were fitted to each detector in the array. They were 19 *cm* long and had a thickness of 0.3 *cm* at the front and 2 *cm* at the back. The shields are used to reduce the Compton continuum in gamma-ray spectra from germanium crystals which are primarily generated by gamma rays that undergo scattering in the detector followed by escape of the scattered photon. Accordingly, coincident detection of the escaping photons in the BGO detectors can be used to reject events that contribute only to the continuum, while preserving full-energy events. In addition to the usual suppression, where a signal is suppressed using its own shield, it was also suppressed by the closest BGO crystals in the next ring of BGO shields. In figure (3.13, a), it can be observed how JUROGAM employs the concept of compton suppression while in figure (3.13, b), a photograph of JUROGAM can be found. The JUROGAM array was only used in experiment A.

Clover detector

A Clover type detector consists of four separate large coaxial high purity germanium crystals HPGe, n-type bulk material, anchored in the same enclosure. Each one of these crystals can be segmented into four regions so that the detector consists of 16 segments. The segmentation of the detector means that each of the four crystals is connected to its own electronics, resulting in separate outcomes for the four regions. Compton scattering between crystals can be combined to reconstruct the original energy of a gamma-ray emission. This method is

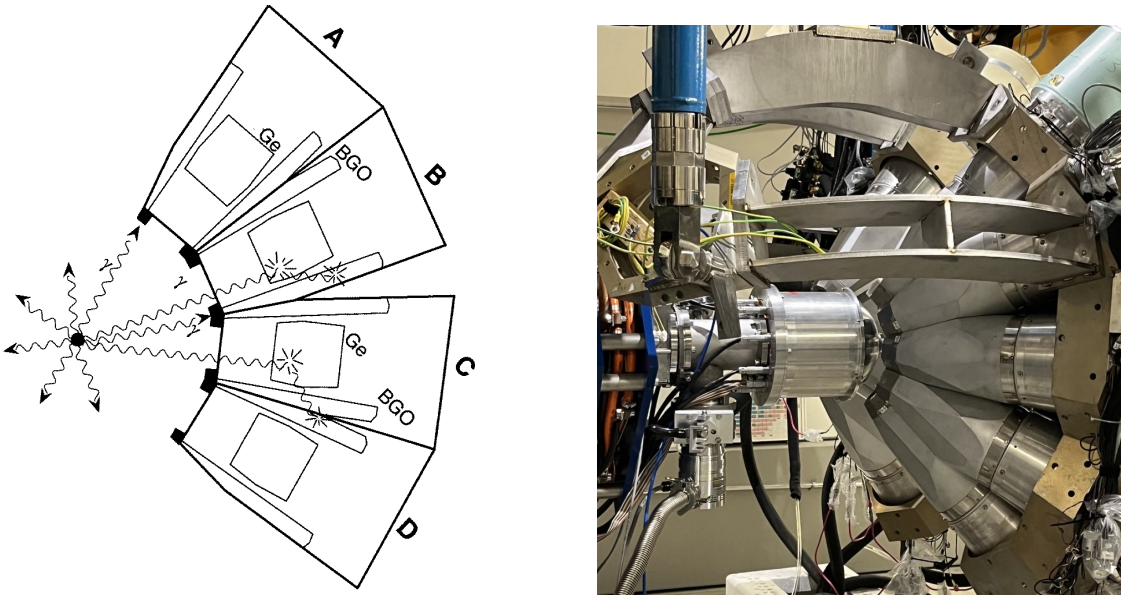

(a) (b)

Fig. 3.13 The diagram in (a) illustrates how compton suppression works in JUROGAM [32]. (b) A photograph of JUROGAM which is located at the entrance to MARA. The beam arrives from the left, it collides with a target positioned inside the target chamber, which is also visible here.

referred to as add-back mode. During experiment B, five clovers were used at the focal point of MARA around the vacuum chamber which held the charged particle detectors, as shown in figure (3.14).

A GREAT type Clover detector was located behind the vacuum chamber; it contains four crystals that are each 10.5 *cm* long and 7 *cm* in diameter before shaping [33]. The first 3 *cm* of their length is sharpened at an angle of 15° on the outside surfaces. As a means of reducing the effect of gamma rays Compton scattering out of the Ge detectors and thereby enhancing the peak-to-total ratio, the HPGe crystals were surrounded by bismuth germanate crystals of 18.5 *cm* in length.

The detectors located on the right, left, and above of the vacuum chamber are EUROBALL type Clovers [34]. These detectors contained four smaller crystals than the GREAT clover, each of which measured 7.0 *cm* in length and 5 *cm* in diameter. During the experiment, the clovers were cooled down with liquid nitrogen-filled insulated dewars to a temperature of 77 $°K$, in order to reduce the effects of leakage current and maintain high energy resolution.

They were primarily installed at the focal plane in order to detect the delayed gamma rays generated by the recoils. It was possible to identify an isomeric state by analysing the delayed gamma rays in conjunction with an evaporation residue implantation in the DSSD. For example, figure (3.15) shows the detected gamma rays correlated with 5565 *keV* alpha decay of ^{156}Lu which is known to have an isomeric 19^- state with a half-life of $t_{1/2} = 179(4)$ *ns* [35].

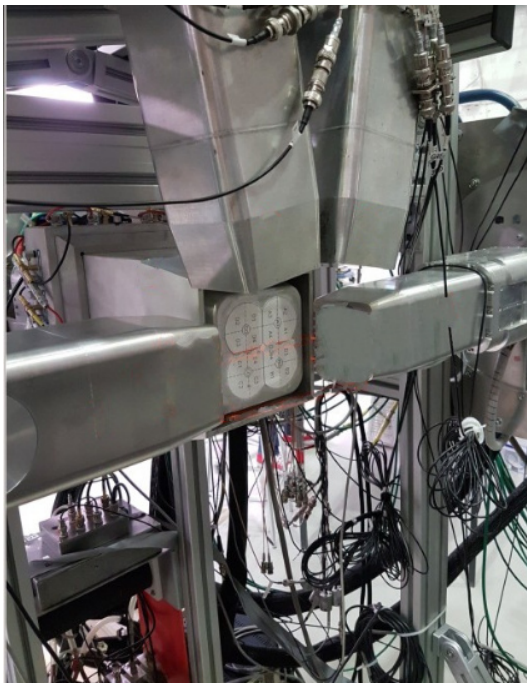

Fig. 3.14 A photograph of the clover detector array installed at the focal plane used in experiment B. During the experiment the array was moved to surround the vacuum chamber containing the DSSD.

Broad energy germanium detector

The Mirion Broad Energy Germanium (BEGe) detector used in this study was a p-type detector model BE6530. The germanium crystal had an active area of 65 cm^2, a diameter of 91.1 *mm*, and a height of 31.4 *mm*. Figure (3.16) illustrates the detector design. The signal contact was represented by a boron implanted p^+ electrode measuring 13.5 *mm* in diameter, while the high-voltage contact was represented by a lithium-diffused n^+ electrode.

This detector had a carbon window that was 0.6 *mm* thick to improve the sensitivity to

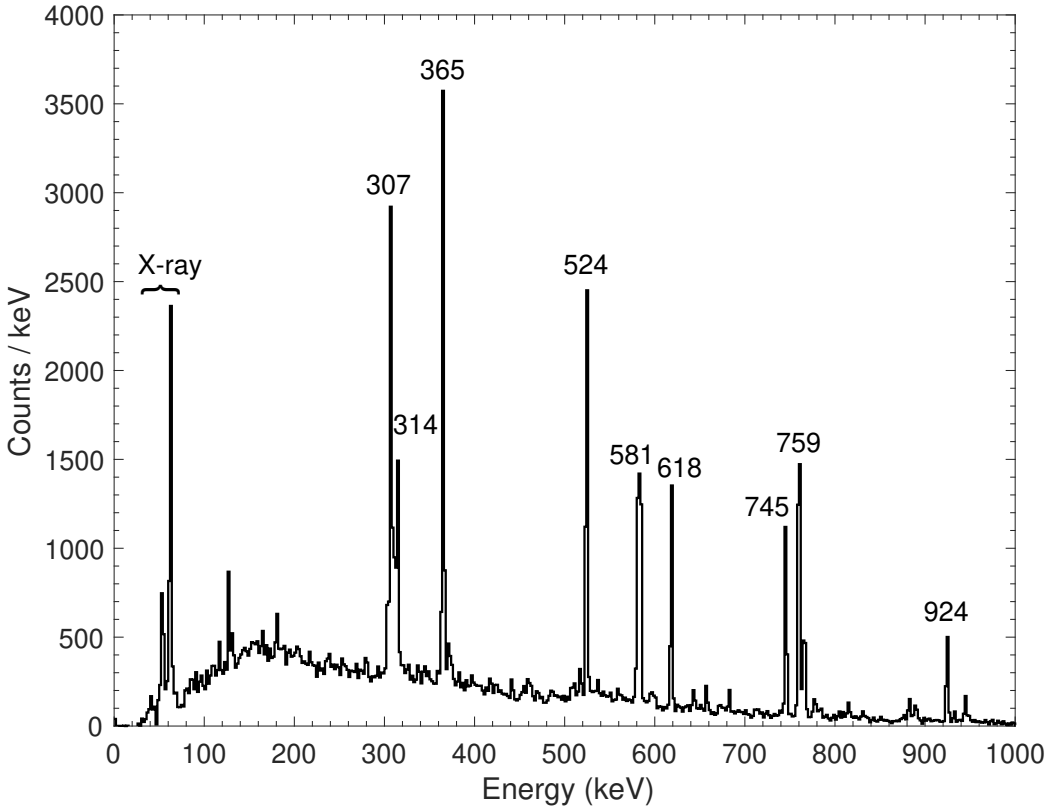

Fig. 3.15 Gamma-ray energy spectrum, with add-back, observed in the focal plane Ge detectors within 600 *ns* of the implantation of an ion into the DSSD that was followed within 800 *ms* by alpha decay from the (10^+) state in ^{156}Lu.

low-energy gamma rays. The crystal was located 8 *mm* from the front window and was held by a copper cup inside an aluminium end cap with a thickness of 1.6 *mm*. One unique feature of the BEGe detector is that it covers an energy range of 3 keV to 3 MeV, which is not found in any other type of detector. Furthermore, the detector generally produces a low background spectrum compare to typical coaxial detectors as well as a better energy resolution [36]. During experiment A, three detectors were placed at the focal plane of MARA in order to detect delayed gamma rays emitted by the recoil nuclei. The position of the detectors is shown in figure (3.9, A) . An analysis of the gamma-ray spectrum obtained after the evaporation residues were implanted into the DSSD allowed the identification of an isomeric state as shown in figure (3.15).

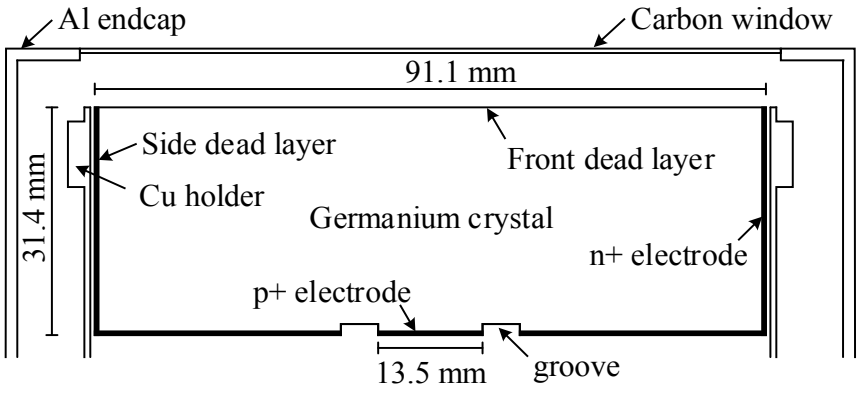

Fig. 3.16 Schematic representation of the BE6530 BEGe detector [37].

3.4.2 Gas-filled detectors

Gas-filled detectors have a relatively simple working mechanism. The passage of external nuclear radiation through a gas medium results in the ionisation of the medium. By collecting the produced ions, features about the radioactive source can be determined, such as its energy, type and position. It is possible to manufacture gas-filled detectors in a variety of shapes depending on the purpose of the research, but they typically consist of isolated metallic wires or plates inside a metallic chamber that holds the gas. By applying an electrical field between

the two metalic surfaces, the electrons drift to the anode and the positive ions are collected by the cathode.

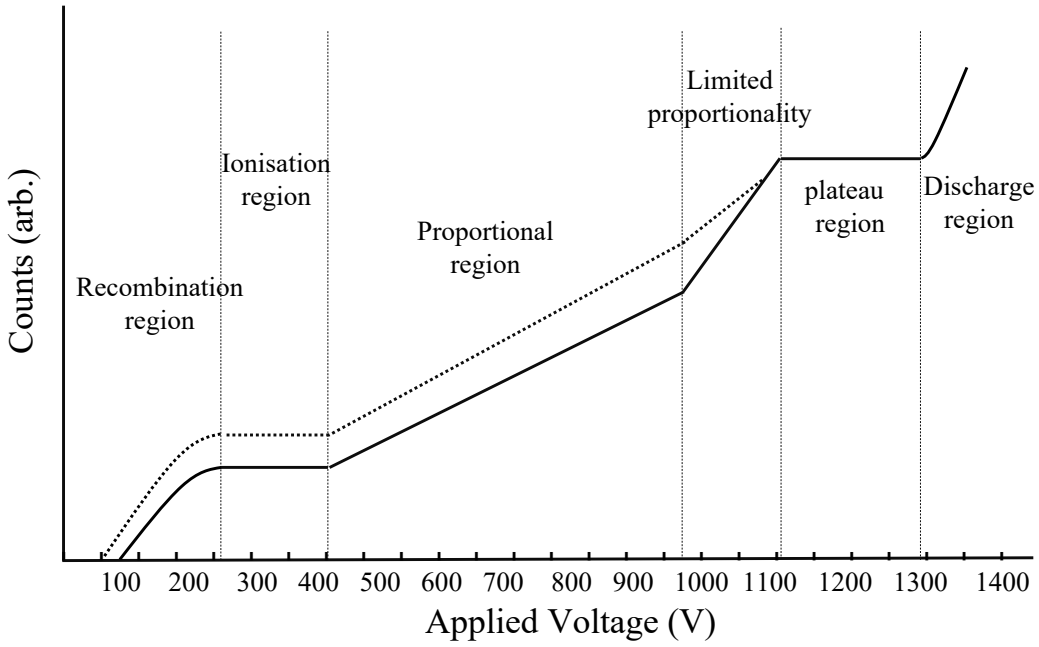

Fig. 3.17 The different operational of gas-filled detectors as a function of voltage.

It is important to note that the range of the applied voltage plays a significant role in the detector performance. Figure (3.17) illustrates the different operational regions of gas-filled detectors. If the voltage between the two electrodes is not high enough to pull all the produced ions, then there will be a recombination of the negative and positive charges. The recombination of ions can be prevented by increasing the potential difference between the cathode and the anode. This is the ionisation chamber region where all the primary ions are collected and the pulse size is independent of the voltage and proportional to the incident energy. Further increasing the voltage to about 400 to 1000 V, depending on the detector volume, results in a linear increase in the resulting signal. This is due to the ability of the primary ions and electrons to ionise the gas medium. This region is known as the proportional region. For environmental samples and generally low-energy particles, it is practical to operate the detector in this region so that the real signal can be distinguished from the electronic noise. The MWPC used in this study works in this region and is described in the next section.

As the voltage increases, the proportionality becomes limited until the plateau region is reached. Electrons in this region are subjected to a strong acceleration, which leads to chain reactions near the anode, known as avalanche effects. In this case, the detector works only as a counter, and any information regarding the particle's energy will be lost. With an increase in the applied voltage, a single ionising event will generate a series of repetitive discharges, thereby forming the discharge region. It is possible for gas in this region to be ionised in the absence of radiation and this may lead to damage the detector when operated in this region.

Multi-wire proportional counter

At the focal plane of MARA, just after the recoils were separated, they passed through a Multi-Wire Proportional Counter MWPC before being implanted into the DSSD. The MWPC used in this work consisted of a grid of 20 μm gold-coated tungsten wires with a 1 mm spacing, which act as the anode. The two-dimensional grid was placed between two large plates that represented the cathode, with a gas filling the space between the plates. Figure (3.18) shows a schematic of a MWPC. As with any gas-filled detector, the MWPC detects by collecting electrons and ions from the electrodes. By passing through the detector, the reaction products ionise the molecules of the gas. The charges were collected by biasing the wire grid and the plates to a maximum voltage of 1000 V. A multi-wire detector has the advantage over a one-wire proportional detector in that it provides a fast response, since one of the most significant disadvantages of gas-filled detectors is the long dead time. Therefore, it is possible for the ions to drift to the nearest anode wire from where they have been produced, as well as for the electrons to drift to the cathode. Furthermore, the position and energy loss of the particles detected were determined with greater accuracy. For this experiment, the MWPC was used to set gates separating recoils from beam residues, distinguishing between recoils and decay events, as well as determining the mass of a correlated unknown gamma ray.

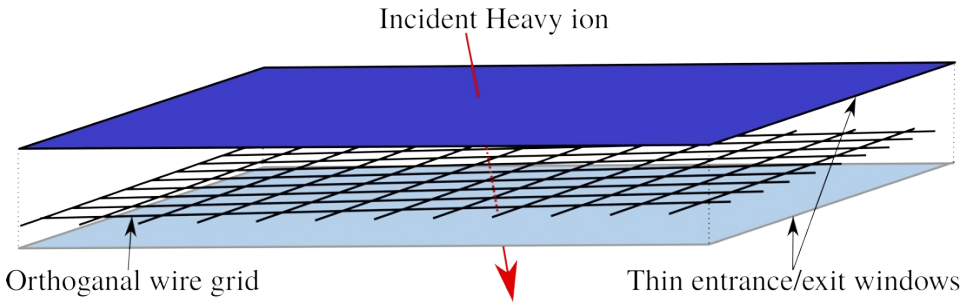

Fig. 3.18 An illustrated representation of a MWPC detector schematic [9].

3.4.3 Scintillation detectors

Scintillation detectors one of the oldest and most widely used types of detector in which a scintillation material is used as the main component. During the passage of ionizing radiation through the material, visible light with an energy of about $3-4\ eV$ is emitted.

As radiation interacts with an atomic electron of the scintillation material, part of its energy is transferred to an electron, which will in turn jump to an exited state. By emitting photons, the electron is then de-excited, a process known as fluorescence. As the light emits isotropically even with high light yield materials, some form of multiplication must be used. The photon must be converted to a primary electron first using photoelectric effects, so a photo-cathode medium is used. To perform the multiplication, a silicon photomultiplier (SiPM) is connected to the photo-cathode. The SiPM can be described as an arrangement of Avalanche Photodiodes (APDs) that function in Geiger mode. Each micro-cell consists of an APD and a quenching resistor that neutralizes residual charge, enabling the APD to receive photons more quickly. The combination of these components in an array increases sensitivity and reduces the recovery time between detection events.

The energy resolution of scintillation detectors is quite low, but they have the advantage of high efficiency and a fast response compared to gas-filled and semiconductor detectors. Consequently, it has been used in this study as a charge particle counter placed at the target chamber.

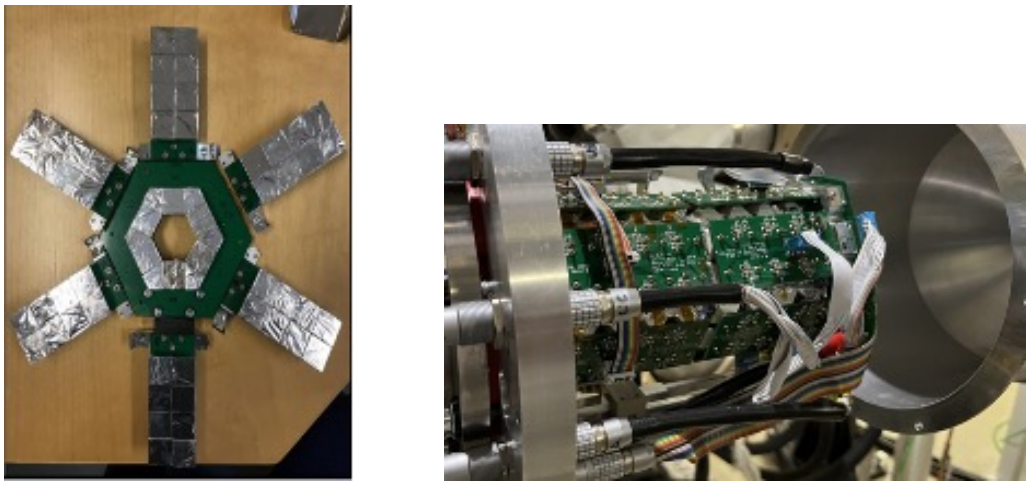

(a) (b)

Fig. 3.19 A photograph of half of the JYUTube that has not yet been mounted (a) [39]. A Photograph of the JYUTube mounted in the target chamber of MARA (b).

JYU Tube detector

The Jyväskylä university (JYU) tube detector consists of plastic scintillation detectors connected to a silicon photomultiplier (SiPM) placed at the target position. The scintillation material was developed using a Polyvinyltoluene (PVT) polymer as a base and has an efficiency of producing 10^3 photons for a 1000 keV incident electron [38]. The detector comprised 120 cells that were divided into two parts and arranged around the six sides of the cylinder, each of which has a hexagonal cross section of 8.15 cm in height. This setup is intended to maximize the solid angle by positioning one of these parts upstream of MARA and the other in the opposite direction in front of the targets wheel. A photograph of the detector is shown in figure (3.19).

In the fusion evaporation reaction, as a compound nucleus is formed, it begins to emit charged particles which can be detected by the JYU tube detector. Basically, it works as a counter detector and therefore acts as a selection device for a particular evaporation channel. Figure (3.20) shows the alpha decay spectra collected using the DSSD at the focal plane. Each spectrum was generated from a correlation between a recoil and its corresponding alpha decay, in addition to the condition of detecting one, two, or three charged particles in the JYtube detector. Fold 1 refers to events that result from the detection of a single charged

particle, whereas fold 2 denotes events that are recorded when two charged particles are detected. Similarly, fold 3 and fold 4 refer to events resulting from the detection of three and four charged particles, respectively.

The JYTube efficiency is not 100 %, which results in a distribution of folds for each number of charged particles emitted. The efficiency of one proton channel suppression is 65 %, while the efficiency of two proton channel suppression is 80 % [39]. In this experiment, the nuclei of interest were produced using an energetic ^{58}Ni beam and a ^{102}Pd target by fusion-evaporation. This results in the formation of a compound nucleus of $^{160}_{74}W$. Therefore, the evaporation channel of one, two or three protons will yield Ta, Hf and Lu isotopes, respectively. Consequently, it is possible to observe the variation in intensity that occurs as a result of changing the fold of the tube.

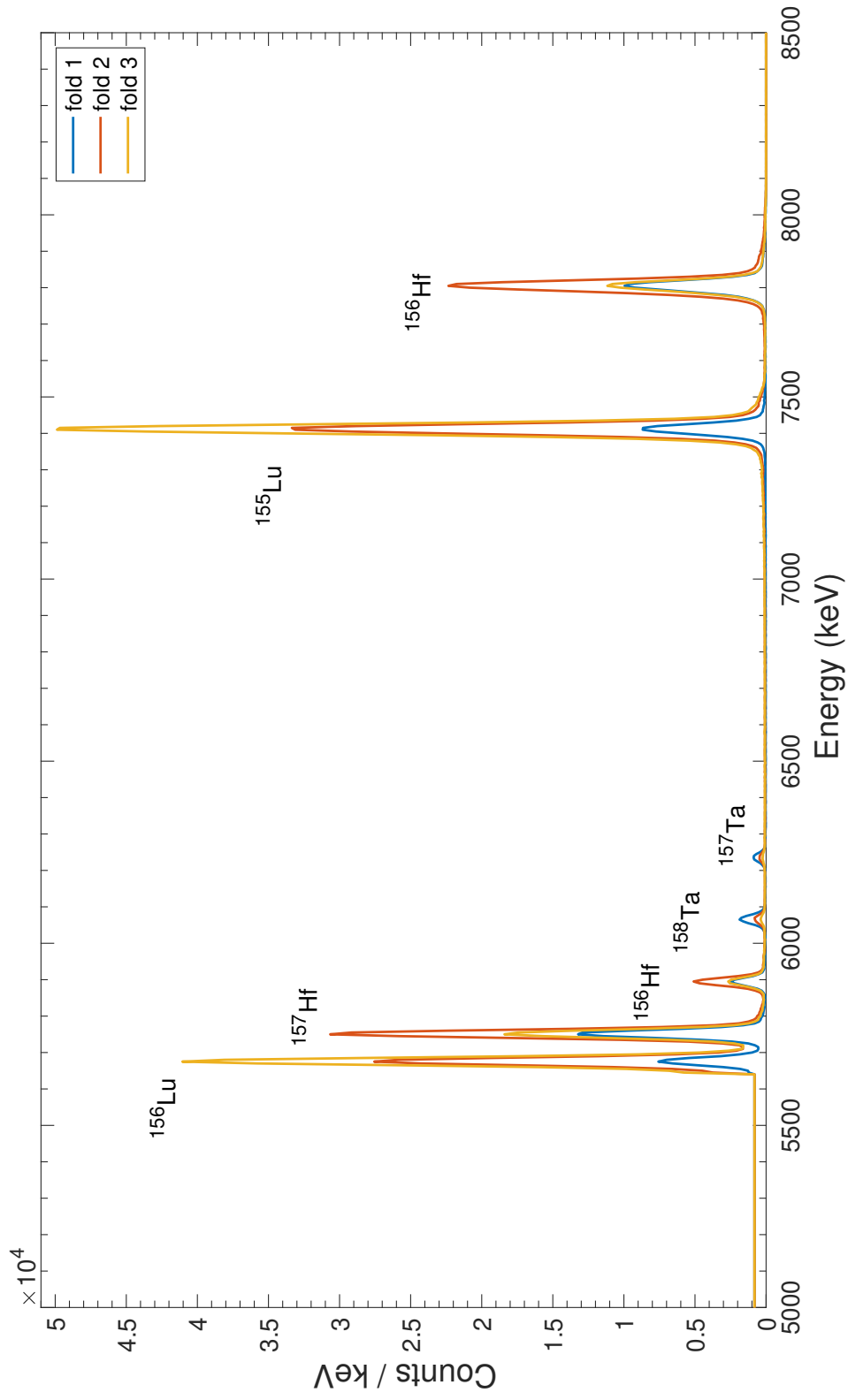

Fig. 3.20 Alpha-decay spectra collected from the DSSD. Spectra are labelled with the production channel selected to generate each spectrum. Presented here is an example of a spectrum correlated with $1, 2$, and 3 charged particles detected by the JYU tube detector, counts below 5200 keV are excluded from the spectra.

3.5 Analysis Techniques

A variety of analysis methods have been applied during this work in order to deal with large raw data sets (approximately 8 TB). Most of the analysis of the recorded data was initially performed using the GRAIN software [40]. The Recoil Decay Tagging technique (RDT) is used to select gamma rays after identifying nuclides based on their known decay properties, energy and half-life. A description of the techniques is provided in the following sections, accompanied by examples of how they were employed in this study.

3.5.1 Data acquisition

For the purpose of acquiring information and reading signals generated by the detectors, the Total Data Readout (TDR) technique was used [41]. Analogue-to-digital converters (ADCs) convert the pulse from the detector after it has been passed by the preamplifier into a digital signal that can be analyzed by a computer. In digital electronics, discrete representations of signals from preamplifiers can be stored. In this work a buffer containing ADC sample data consists of 1016 samples, each of which is 16 bits in size, along with a 64 bit header, giving a total event size of 2040 bytes was used.

The TDR method is a triggerless data acquisition method,that avoids common dead-time losses. When, for example, there is interest in the detection of gamma-rays emitted from relatively long-lived isomeric states, the time gate will have to be set to be long enough to detect these rays, thereby increasing the dead time and causing more events to be lost. A wider gate will result in greater losses, both in the gamma detector system and in the charged-particle detector system.

In order to overcome the dead time issue and prevent signals from being lost, especially when the production rate for undesired channels is high, the total data readout system was developed. Each signal in the detectors is time stamped with a precision of 10 ns achieved by 100 MHz wide clock. The signals are read individually, then passed to a software program where events are constructed according to spatial and temporal correlations. Grain software packages, written in Java, were used to open, sort, and analyse the recorded data. In addition

to using Grain for sorting data, files have been exported as ASCII format to use in other software packages such as ROOT [42, 40]. Python and Matlab were also used in the analysis and to perform fits on data points such as peaks to identify the centroid and the area under the peaks.

3.5.2 Recoil-decay identification

Executing a fusion evaporation reaction leads to the implantation of various types of nuclear species into the DSSD at the focal plan of MARA. It is necessary to do some method of ion identification in order to investigate the nuclear structure of any of these implanted particles, for which Recoil Decay Tagging (RDT) has been used [43]. In addition to the fusion evaporation residues, part of the unreacted beam passes through the MARA separator and ends up in the DSSD.

Both the evaporation reaction products and the unreacted beam are passing through the MWPC and lose some of their energy before being implanted into the DSSD. The Time Of Flight (TOF) between the MWPC and DSSD of these ions can be used to distinguish between the slow-moving evaporation residues and the faster unreacted beam. Furthermore, the highly energetic lighter ion beam of $^{58}_{28}Ni$ deposits less energy in the MWPC than the recoils. Figure (3.21) shows a plot of the flight time between MWPC and DSSD of the implanted ions which deposited their energy into the DSSD. There are three intense collections of ions in the figure representing the unreacted beam at the high energy region, the fusion evaporation residues at the low energy region and the curvy line extending from about 10 MeV representing the scattered reaction products. In order to achieve a clean separation between the implanted ions, TOF and energy limits must be set in such a way that only include fusion evaporation residues.

This work examines the structure of nuclei in the neutron-deficient region close to the proton drip line. It is common for nuclei in this part of the nuclear chart to undergo alpha, proton and beta decay. As a result, signals from recoils and their decays are collected in the DSSD. Once the recoils of interest have been identified, the next step in the analysis is to correlate them with their decaying products.

When an ion interacts with silicon material, information is saved regarding its energy E_i, implant time t_i, and position on the two sides of the detector x_i and y_i. An advantage of using the highly segmented DSSD as a charged particle detector is that spatial and time correlation can be performed. When two events occur within the same pixel, they are tagged as possible recoil-decay events. It is important to keep in mind that the recoil event causes a signal to be generated in the MWPC and DSSD, in contrast with the decay event in which the signal appears only in the DSSD.

Additional time conditions must be applied to confirm the link between the two events, this time being based on the half-life of the nuclei under consideration. The optimal time gates chosen to maximise statistics but minimise background will depend on the half-life of the decay in question and the background rates. Therefore, during the analysis, each nuclide was considered separately, taking into account the energy, mass, and half-life in relation to other possible ions implanted in the same pixel.

One of the disadvantages of this approach is that random correlations cannot be avoided. The problem arises when more than one recoil is detected at the same pixel at the same time. The system may overlook the second recoil and erroneously assign its decay products to the first recoil if the second recoil has a shorter half-life than the first one. Moreover, the detector's per channel dead time, which the TDR cannot avoid without using traces, can also cause this mismatches.

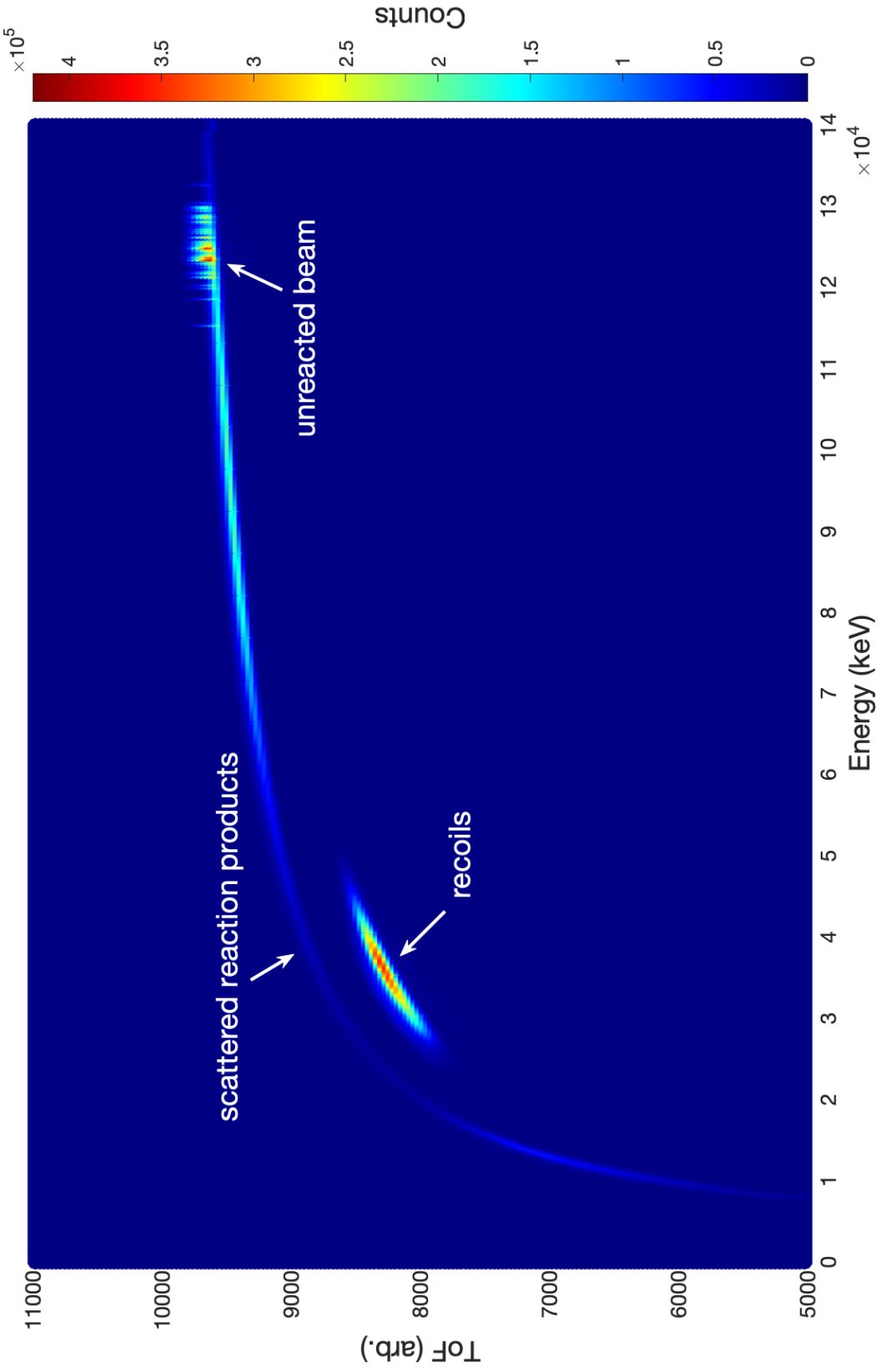

Fig. 3.21 Plot of the energy deposited in the DSSD as a function of flight time between the MWPC and the DSSD.

3.5.3 Gamma-ray identification

In this work, the aim was to investigate an isomeric state near the proton drip line in the $N = 83$ region. RDT is a powerful technique which can be used for correlating the fusion evaporation residues with gamma rays depopulating an isomeric state. Gamma rays emitted from isomers that have survived the flight through the recoil separator will be detected by the germanium detectors located around the vacuum chamber at MARA's focal plane. It is possible to identify an isomeric state by applying a time limit between recoil implementation and gamma ray detection that will allow some of the isomeric transitions to be observed. A further correlation with a subsequent alpha decay will improve the identification.

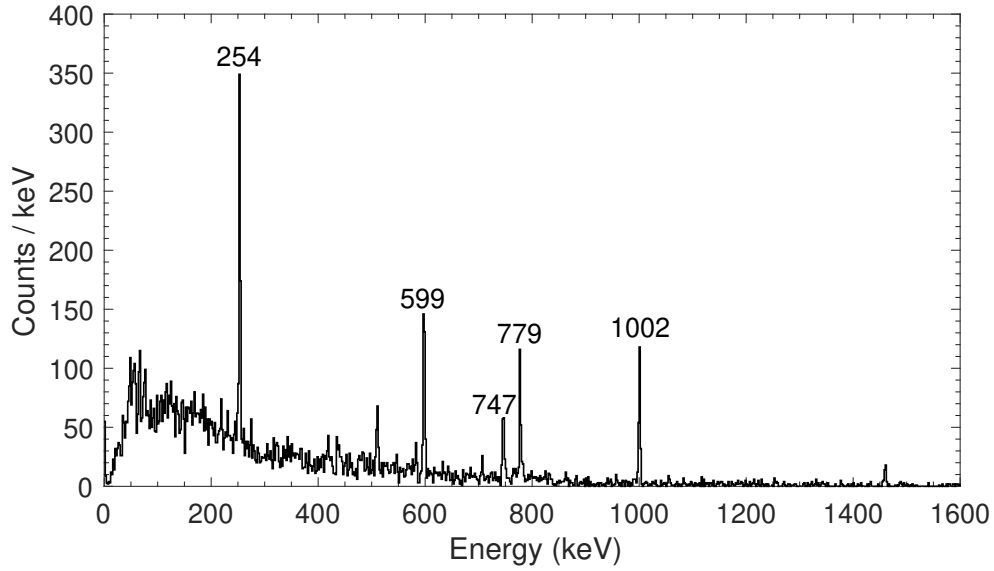

Fig. 3.22 Energy spectrum of gamma rays tagged using the alpha decay from the $^{158m1}Ta$ (9^+) state with a recoil-α correlation time of 175 ms, with additional condition that a delayed ^{158}Ta gamma ray is observed in a focal plane clover detector within 10 μs of the recoil implantation [44].

Figure (3.22) shows gamma transitions which depopulate the 6.1 μs isomeric state in ^{158}Ta where the recoil is correlated with the 6048 keV alpha decay. However, it is not always the case that gamma transitions are followed by the alpha decay: instead, beta particles may be emitted before an alpha emitter is reached. As a result, the time gate between the recoil and the decay of the charged particle can be optimised so that the second-generation nuclei can

decay, and then a correlation between the two events can be made.

An example of such a case is the detection of the $27/2^-$ isomeric state decay in ^{153}Yb, which has a half-life of 4.2 s and beta decays to ^{153}Tm [45, 46]. Figure (3.23) shows the energy spectra of gamma rays observed in the focal-plane germanium detectors. Gamma rays were recorded within 8 μs after an evaporation residue was implanted into the DSSD and was followed by the alpha decay of ^{153}Tm the same DSSD pixel within 2 to 20 s. These highly intense transitions can be seen in the level scheme shown in figure (4.17). The $K\beta_1$ X-ray transition with an energy of 59 keV, is visible to the right of the strongest peak at 51 keV.

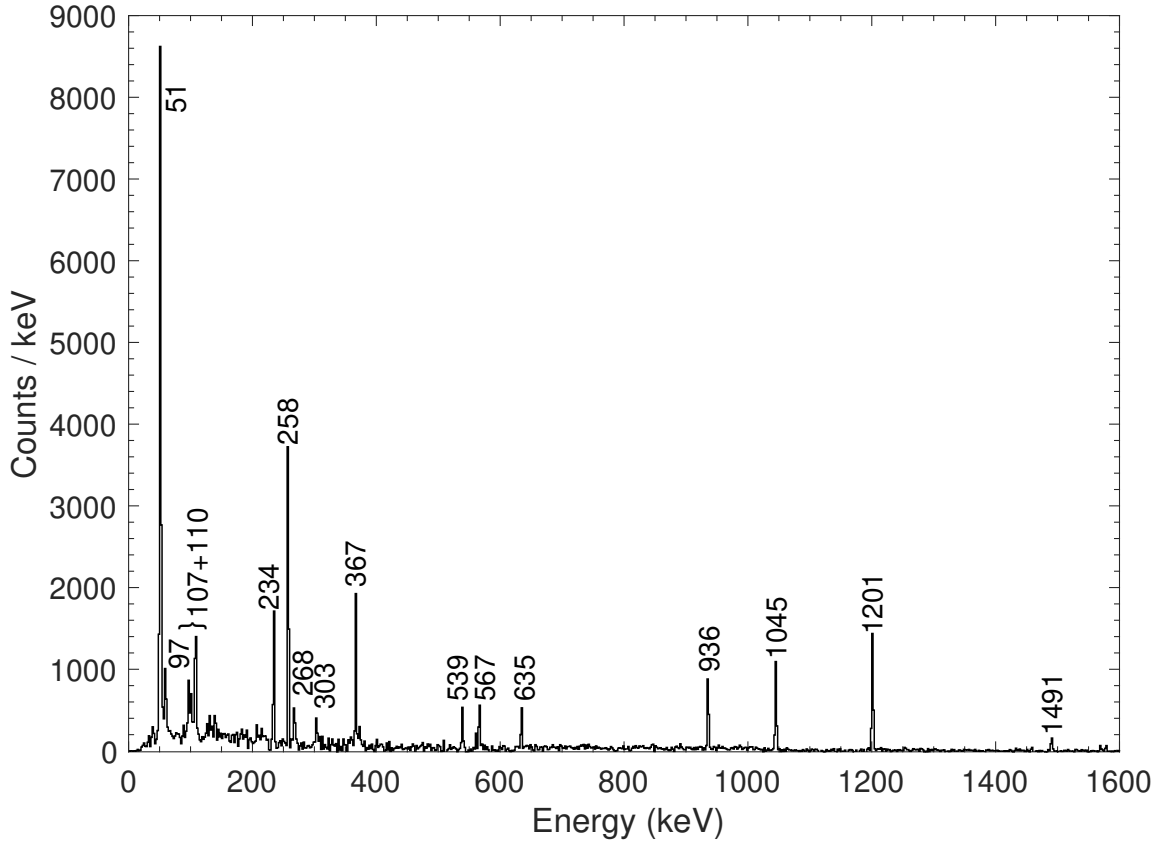

Fig. 3.23 A background-subtracted energy spectrum of γ rays obtained using the RDT technique tagging on α decays from ^{153}Tm with a 20 s correlation time.

Gamma rays detected at the target position were in delayed coincidence with the implantation of fusion-evaporation residues in the DSSD. By taking advantage of the additional selectivity offered by the isomer decay, transitions observed at the target position can be studied. Tagging

on gamma transitions depopulating the ^{153}Yb isomer shows clear unidentified peaks. Figure (3.24) shows the energy spectrum of the gamma rays. These transitions have been confirmed to belong to ^{153}Yb in an experiment designed to study the structure of ^{153}Yb. The results will be published soon and are not analysed further in this thesis [47]. The energies and the intensity of these transitions are displayed in table (3.2).

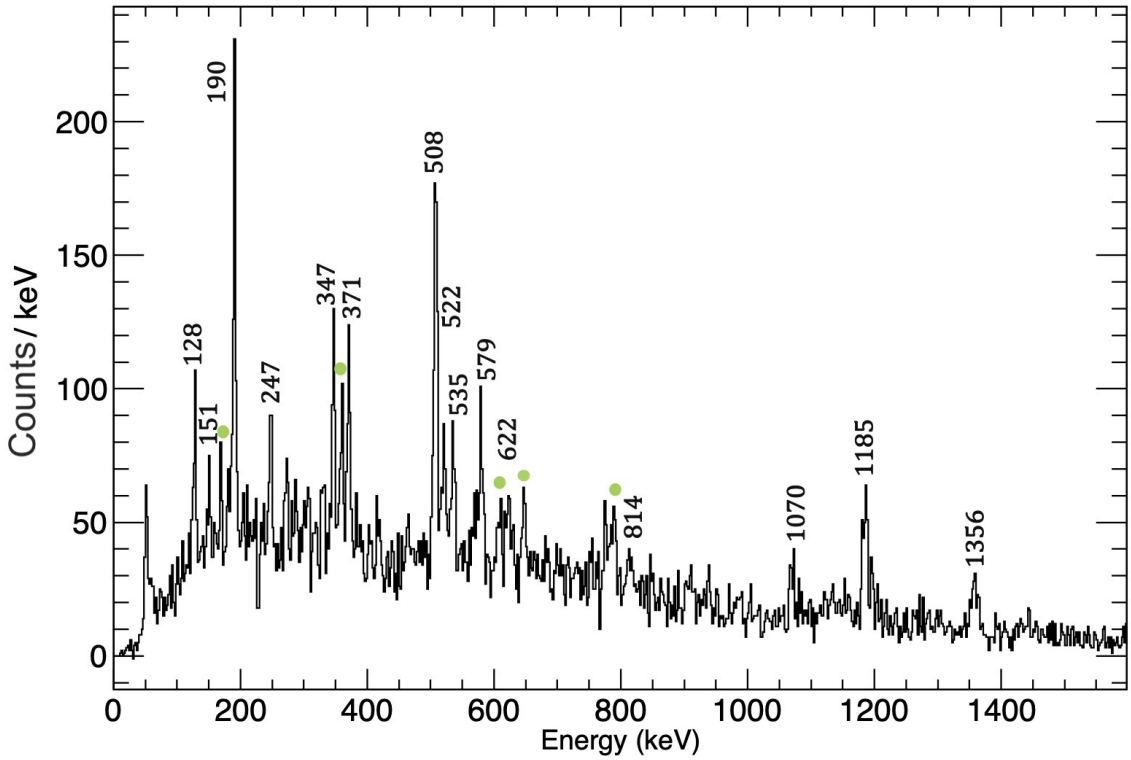

Fig. 3.24 Energy spectrum of γ-ray transitions detected at the target position and correlated with γ-ray transitions from the ^{153}Yb isomer detected at the focal plane which were recorded within 8.0 μs of an evaporation residue implanted into the DSSD was followed by an alpha decay of ^{153}Tm using a correlation time of 20 s.

There is also the possibility of using the mass dispersion feature of the separator in order to connect the observed gammas to the correct nuclei. Figure (3.25) indicates the MWPC position of different recoils which are correlated with the subsequent isomer decays of ^{156}Lu and ^{158}Ta detected by the focal plane germanium detectors. Each peak corresponds to the ^{156}Lu or ^{158}Ta ions passing through MARA in a different charge state.

Table 3.2 Energies and efficiency-corrected relative intensities of gamma-ray transitions feeding the $27/2^-$ ^{153}Yb isomer. Energies are accurate to ± 1 keV.

Energy (keV)	Peak Area	Intensity
127.8	320 (41)	18 (3)
151.1	116 (29)	9 (2)
190.7	769 (57)	45 (4)
247.5	263 (39)	17 (2)
346.9	427 (42)	35 (3)
370.9	444 (45)	37 (4)
507.9	996 (54)	100 (5)
511.3	192 (32)	18 (3)
521.9	171 (28)	17 (3)
535.3	310 (43)	32 (4)
578.9	390 (57)	41 (6)
621.9	165 (30)	18 (3)
647.4	135 (34)	15 (4)
814.2	130 (36)	16 (4)
1069.5	140 (26)	20 (4)
1185.4	431 (37)	67 (6)
1356.0	226 (31)	38 (5)

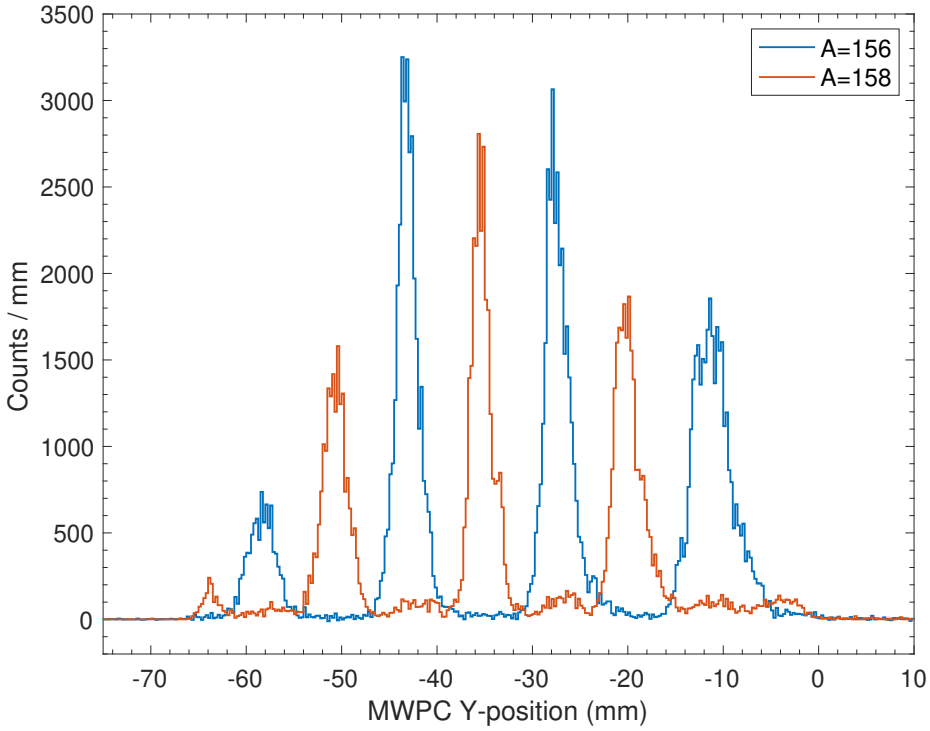

Fig. 3.25 The horizontal (Y) position of mass 156 (blue) and mass 158 (orange) evaporation residues that traversed the MWPC prior to implantation in the DSSD, selected by measuring subsequent gamma rays detected at the focal plane Ge detectors.

3.5.4 Energy calibration

In order to derive accurate spectroscopic measurements about detected radiation, it is necessary to transform the electrical response of a detector into its corresponding energy. However, before converting to energies and in order to produce a sum spectrum, the responses of each channel within a detector must be matched. This is usually done through including individual parameters for each channel into the software.

For precise measurements of the energy decay properties of nuclei, the detectors must be calibrated before, during and after operation. This is to correct for any gain shift that may have occurred. To calibrate both the JUROGAM and the focal plane germanium detectors, a joint $^{152}Eu^{133}Ba$ source was used. The gain matching of the DSSD was conducted with an alpha source consisting of ^{244}Cm, ^{241}Am, and ^{239}Pu. A further internal alpha calibration was applied to the DSSD using the alpha decay of ^{151}Dy, ^{150}Dy, ^{158}Ta and ^{156}Hf which all were produced during the experiments. Those were chosen based on the range of energies they cover. A list of the energies that have been used is provided in the table (3.3). Figure (3.26) illustrates the goodness of the fit following the internal calibration with the implanted alpha decay energies, in the same figure shows the corresponding residuals.

3.5.5 Efficiency calibration

It is possible to define the efficiency of germanium detectors in several different ways, depending on their intended use. The most common definitions are;

- Relative efficiency; this refers to the detector's ability to detect the ^{60}Co gamma ray at 1332 keV in comparison with a standard NaI scintillation detector.
- Intrinsic efficiency is measured by relating the counts in the spectrum with the number of gamma rays incident on the detector and does not depend on the source-detector geometry.

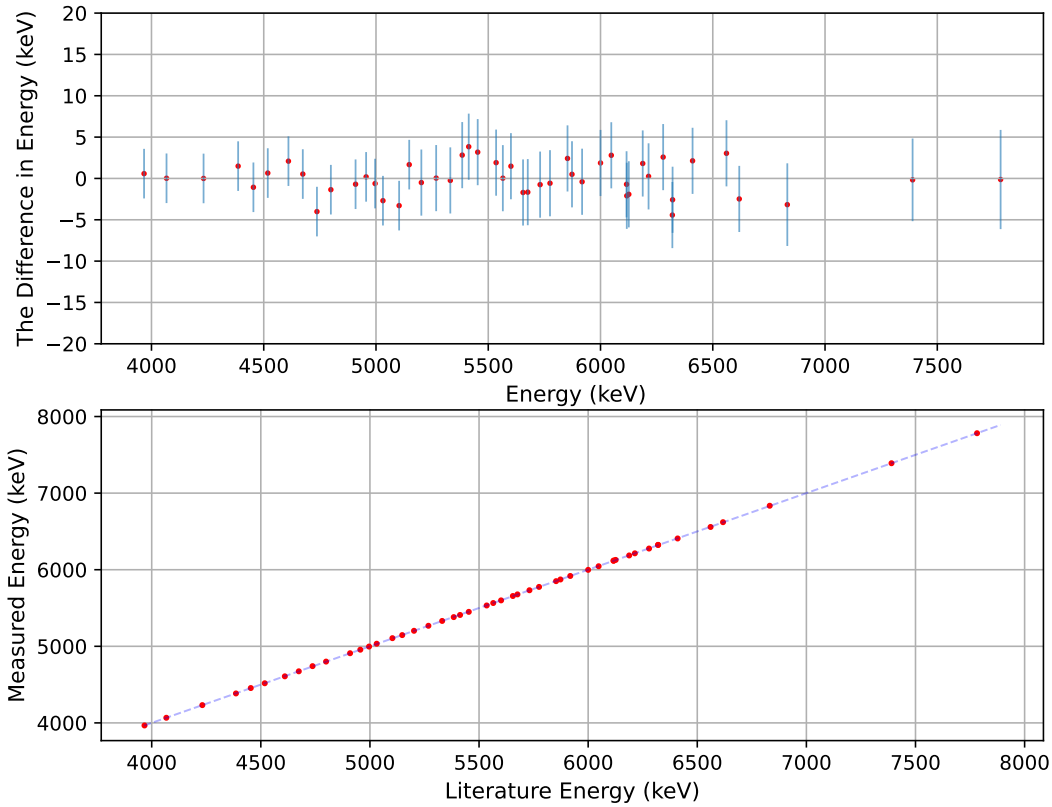

Fig. 3.26 A plot of the alpha-decay energies measured in this study after a linear calibration fit in the bottom. The corresponding residuals are also included in the top.

Table 3.3 Literature values for gamma decay in ^{133}Ba and ^{152}Eu and alpha decay in ^{151}Dy, ^{150}Dy, ^{158}Ta and ^{156}Hf that were used to calibrate the detectors.

Isotope	Energy (keV)	Reference	Isotope	Energy (keV)	Reference
^{151}Dy	4067.00 (5)	[48]	^{152}Eu	121.78 (1.30)	[49]
^{150}Dy	4232.00 (5)	[48]		244.69 (0.46)	[49]
^{158}Ta	6046.00 (4)	[50]		344.28 (1.20)	[49]
^{156}Hf	7782.00 (4)	[50]		586.29 (0.19)	[49]
^{133}Ba	53.16 (0.22)	[49]		778.90 (0.44)	[49]
	80.99 (0.6)	[49]		867.39 (0.19)	[49]
	223.23 (0.04)	[49]		964.05 (0.44)	[49]
	276.39 (0.22)	[49]		1089.70 (0.08)	[49]
	302.85 (0.05)	[49]		1112.08 (0.48)	[49]
	356.01 (1.90)	[49]		1212.00	[51]
	383.85 (0.30)	[49]		1299.20	[51]
				1408.00	[51]

- Absolute total efficiency is a measure of the number of gamma rays emitted by the source compared to the number of counts detected in the full-energy peak and the Compton continuum.

- The absolute full-energy peak efficiency; this refers to the peak area at a certain energy in relation to the number of gamma rays emitted from the source. It is often used in gamma-ray spectroscopy and it depends on the geometrical arrangement of the source and detector. Whenever the term "efficiency" is used in this work, it refers to the full-energy peak efficiency.

In general, the efficiency can be defined as:

$$\varepsilon = \frac{N_{recorded}}{N_{emitted}} \tag{3.8}$$

Where $N_{recorded}$ represents the total counts in the full energy peak and $N_{emitted}$ is calculated using the following equation:

$$N_{emitted} = T \times A \times I_{\gamma} \tag{3.9}$$

Where T is the life time in seconds, A the current activity of the source in becquerels, which can be calculated using equation 2.10, and I_{γ} is the branching ratio of gamma ray. Two calibrations were carried out in this study, one for the Jurogam array and the other on the focal plane germanium detectors. In both, a dual standard calibration source of ^{152}Eu and ^{133}Ba was used since they cover a wide range of gamma-ray energies. A list of gamma-ray energies that have been used for the calibration is provided in table (3.3). Using the sum-peak method [52, 53] , the efficiency curve was normalised with the absolute gamma-ray efficiency derived from the ^{60}Co data. Using the source's activity, the efficiency calculation is then validated. In figure (3.27), values of Jurogam efficiency as a function of gamma-ray energy are plotted and fitted using the following equation:

$$\varepsilon = P_3 \,.\, 10^{\,[\,P_0 \,.\, log_{10}\, x + P_1 \,.\, log_{10}\, x^2 + P_2 \,.\, x^{-2}\,]} \tag{3.10}$$

Where x is gamma-ray energy and $P_0,\ P_1,\ P_2\ P_3$ are the parameters of the fit function.

Monte Carlo simulation

Monte Carlo calculation is a computational method that uses random sampling to obtain results. Particle interactions are estimated based on external physics libraries and the process randomly in order to achieve a better statistical approximation of the real results. By increasing the number of simulated initial events, it is possible to improve the accuracy of simulations.

International collaboration of scientists at CERN has developed a Monte Carlo toolkit called GEANT4 (GEometry ANd Tracking 4) [54]. It is capable of accurately simulating particle propagation through interactions with matter. A significant advantage of GEANT4 is that it is based on C^{++} class libraries, which provide greater flexibility than other Monte Carlo

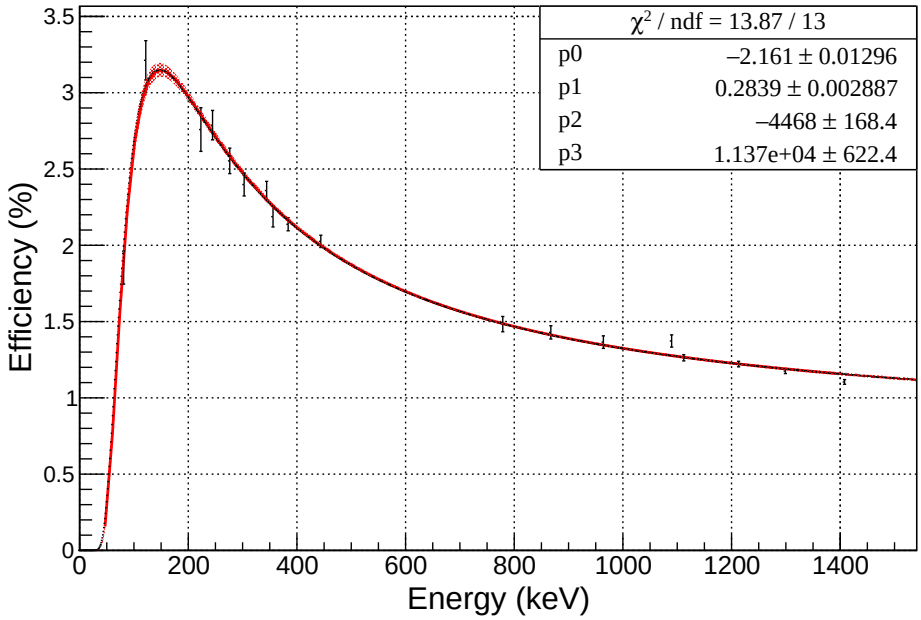

Fig. 3.27 An efficiency curve for the Jurogam spectrometer obtained using a compound $^{152}Eu^{133}Ba$ source. All the parameters of the fit function are shown in the box, including the reduced χ^2 value of 1.06.

codes such as MCNP, which is a fixed executable program. Through the use of GEANT4, particles can be tracked at all points of interaction, enabling data such as the amount of energy deposited per step and the particle's position to be determined. When the information from all steps is combined, specific information about each event can be extracted allowing useful outputs to be produced, such as energy spectra and radiation distributions.

Simulations were used to determine the efficiency of focal plane germanium detectors in both experiments. The need for simulation arises from a lack of knowledge regarding the activity and location of the source that emits gamma rays. The objective in this study was to search for new gamma-ray transitions that depopulate isomeric states. It is therefore essential to correct the intensity to produce the correct level scheme.

The first step is to construct the detector geometry, consisting of the crystal, window, end cap, and casing. Additionally, the calibration sources (^{152}Eu and ^{133}Ba) and source holder geometry are included in the simulation inputs. A screenshot of the simulation of the focal

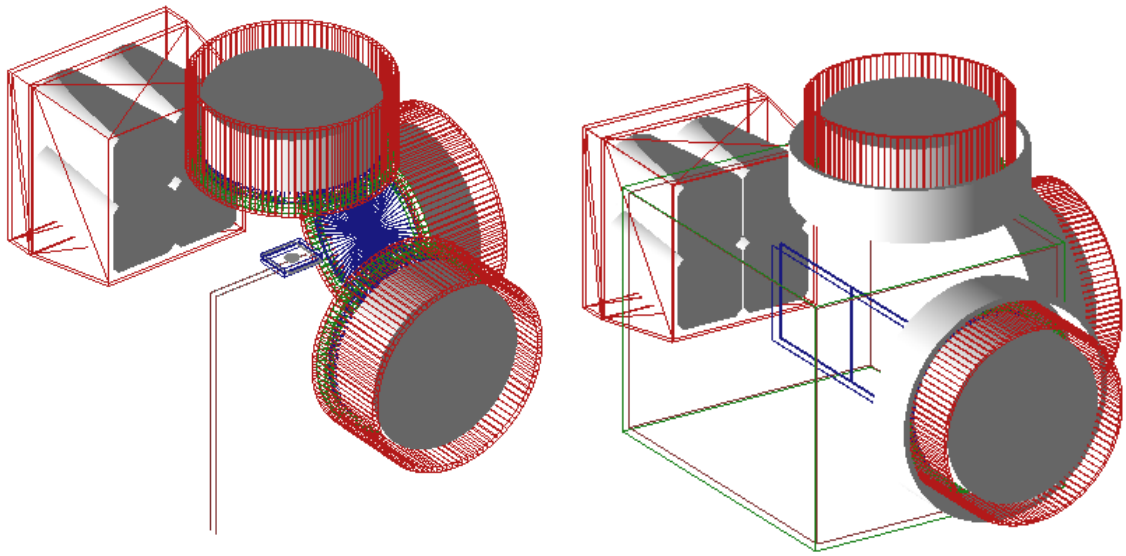

(a) (b)

Fig. 3.28 Screenshots of the simulation of the focal plane germanium detectors in GEANT4. The calibration source between the detectors can be seen in (a). (b) shows the DSSD and the punch-through detectors inside the vacuum chamber. The detectors' plastic caps are removed only in order to display the windows.

plane detectors system is shown in figure (3.28.a). A gamma spectrum was generated for each source using the energy list in table (3.3). The efficiency values were then obtained by dividing the area under each peak by the number of primary particles.

Through the use of point calibration sources, the simulation was tested against experimental data following the same steps as described above for the efficiency calibration of Jurogam. As shown in figure (3.29), the efficiency curves produced are in good agreement with each other. Once the validation using the point sources had been performed, the vacuum chamber and its contents, the DSSD and punch-through detectors, were added to the simulation. A screenshot of the simulation of the complete focal plane detectors system is shown in figure (3.28.b). The actual position of gamma rays was unknown, so the closest estimate was to use the distribution of the recoils identified by their alpha decay in the DSSD. Due to passing through MARA separator, the X-Y position of the recoils was highly dependent on the mass number of the isotope.

During the experiment, three well-known isomers were produced: ^{158}Ta, ^{156}Lu and ^{153}Yb.

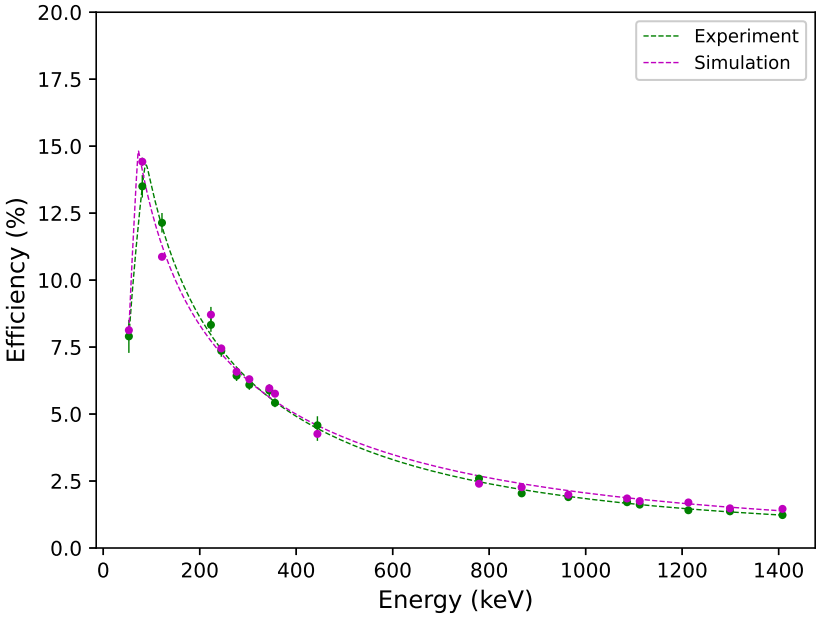

Fig. 3.29 An efficiency calibration curve generated for the germanium detectors at the focal plane of MARA using a $^{152}Eu^{133}Ba$ compound source produced by experimental measurements (green) and simulation (pink).

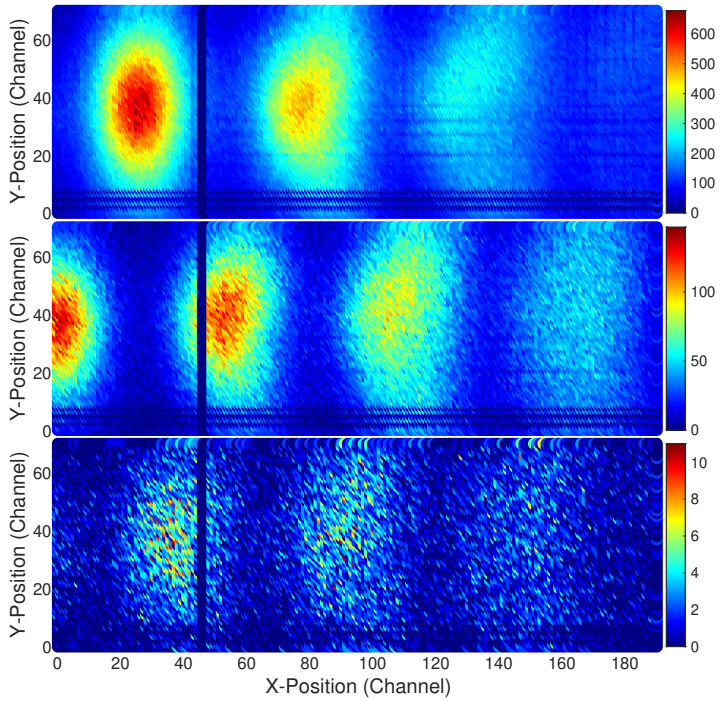

Fig. 3.30 The DSSD X and Y positions of evaporation residues of ^{153}Yb (top), ^{156}Lu (middel) and ^{158}Ta (bottom) determined by measuring their subsequent alpha decay.

Figure (3.30) illustrates the distribution of these recoils in which each group represents a different charge state. Therefore, it is possible to verify whether the applied method is valid by using the distribution of these isomers. After producing a gamma-ray spectrum for each isomer, the efficiency value were determined. The intensities of gamma rays for those isomers were calculated from experimental data and corrected using the efficiency calculated from simulations. Table (3.4) shows the efficiency corrected intensity from this study which can be compared to published values. Following this, the efficiency values obtained from the known isomers were combined in order to produce an efficiency curve that can be used to correct the intensity of gamma rays detected in the focal plane detectors in this experiment. This efficiency curve is shown in figure (3.31) where the values of the efficiency as a function of gamma-ray energies were fitted using the following equation:

$$\varepsilon = e^{[(A+Bx+Cx^2)^G+(D+Ey+Fy^2)^{-G}]^{-1/G}} \tag{3.11}$$

where A, B, C, D, E, F, and G represent the parameters of the fit function. $x = log(EG/E1)$ and $y = log(EG/E2)$. The variable EG denotes the gamma-ray energy, and the constants $E1$ and $E2$ are equal to 100 keV and 1 MeV, respectively [55].

Table 3.4 Gamma-ray energies and intensities relative to the 759.4 *keV* transition in ^{156}Lu [56], to the 1201.4 *keV* transition in ^{153}Yb [1] and to the 599.8 *keV* transition in ^{158}Ta [44] obtained from literature and measured in this work after intensities have been corrected for the efficiency of detection.

Nuclide	Energy (keV)	Intensity	Literature Intensity
^{156}Lu	126.0	6.1 (5)	8.5 (1)
	307.1	68.1 (16)	77.2 (12)
	314.0	33.6 (10)	44.0 (14)
	364.7	98.0 (17)	101.6 (7)
	524.0	96.9 (15)	101.6 (8)
	618.3	55.5 (11)	56.9 (6)
	744.8	54.0 (12)	53.0 (5)
	759.4	100.0 (16)	100.0 (10)
	923.9	30.8 (9)	34.1 (4)
^{153}Yb	109.5	98.0 (5)	91.0 (15)
	257.6	616.0 (31)	659.7 (55)
	367.1	384.0 (19)	411.1 (38)
	539.4	142.0 (7)	156.3 (15)
	935.8	473.0 (24)	454.7 (54)
	1045.3	612.0 (31)	600.1 (70)
	1201.4	1000.0 (50)	1000.0 (120)
	1490.6	148.0 (7)	158.4 (23)
^{158}Ta	253.5	911.0 (47)	961.7 (51)
	599.8	1000.0 (40)	1000.0 (70)
	747.2	488.0 (26)	467.4 (99)
	778.8	579.0 (31)	584.4 (40)
	1001.6	984.0 (51)	962.3 (60)

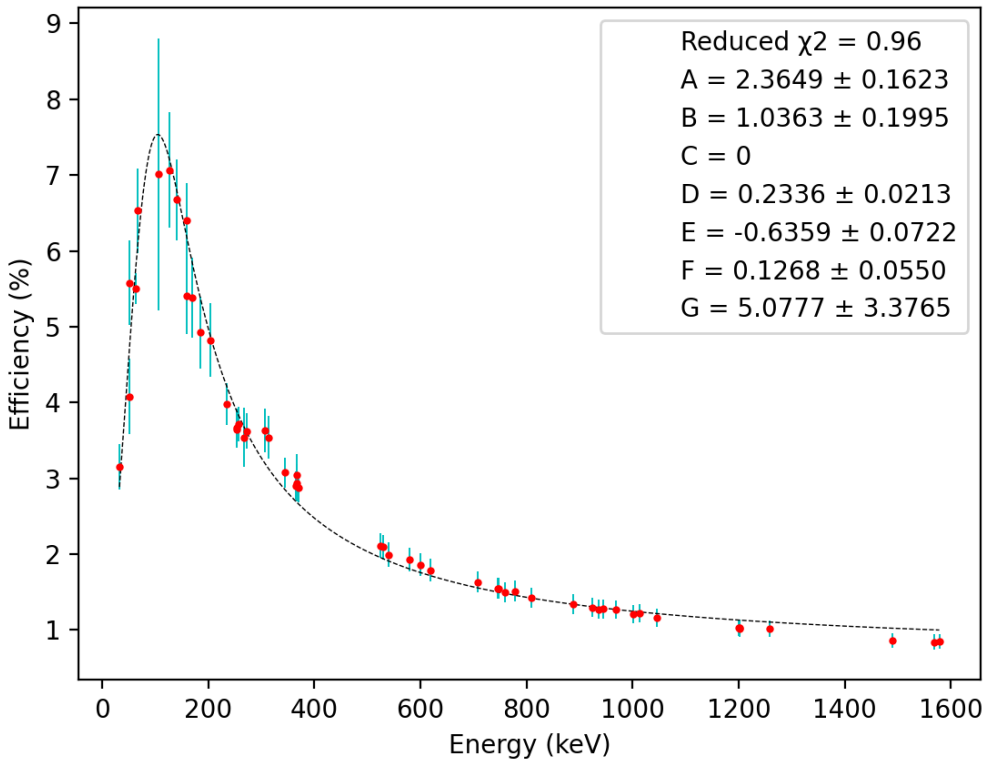

Fig. 3.31 Efficiency calibration curve of the focal plane germanium detector system using GEANT4 simulation of implanted ions in the DSSD.

Chapter 4

First Observation of Excited States in ^{155}Hf

4.1 Introduction

In this chapter, the first observation of excited states in the neutron-deficient even-odd nucleus ^{155}Hf, $Z = 72$ and $N = 83$, are presented. The ^{155}Hf nucleus is located one neutron above the $N = 82$ shell closure and lies near the proton drip line. Nucleons in the Fermi surfaces are expected to occupy the following level; the proton $h_{11/2}$ and neutron $f_{7/2}$, $h_{9/2}$ and $i_{13/2}$ orbits. At low spin, an isomeric state was observed through the detection of delayed gamma rays. A level scheme is constructed and $\pi {h_{11/2}}^n \otimes \nu f_{7/2}$ configurations are assigned and discussed.

Experiments in this region are challenging because correlations with subsequent α decays are delayed by intervening β emissions that are relatively long lived. Previous studies of isomeric decays in the exotic proton-rich $N = 83$ even-Z isotones have confirmed the existence of isomeric states in ^{149}Dy, ^{151}Er, and ^{153}Yb [57, 58, 59]. The ground states in all isotones was assigned a spin and parity of $7/2^-$ based on the single-particle configuration $\nu f_{7/2}$. No excited states in ^{155}Hf had been observed prior to this work.

In this work, an experiment was performed to search for isomeric states in ^{155}Hf. Nucleons outside the closed shell of a heavy nucleus can occupy orbits with high orbital angular

momentum. Consequently, multi-particle states with large spins can be produced at relatively low excitation energies. As a result of a low transition energy and a large spin change between two states, an isomeric state can be formed. In order to be considered isomeric, a state must be long-lived in comparison to other excited states of a particular nuclear species. The long lifetime of states can be attributed to a reduced overlap between the initial and final wave functions, which hinders the decay of the state [60]. By analysing the angular momentum couplings between multiple valence nucleons, it is possible to determine how nucleon-nucleon interactions evolve as proton or neutron numbers change.

The experiments were performed at the accelerator laboratory at the University of Jyväskylä using the apparatus described in Chapter 3. An accelerated stable ^{58}Ni beam was produced, with energies between 293 and 315 MeV, and projected onto an 1 mg/cm^2 ^{102}Pd isotropically enriched target. ^{155}Hf nuclei were produced through the following reactions:

$$^{102}Pd(^{58}Ni, 2p3n)^{155}Hf^* \tag{4.1}$$

$$^{102}Pd(^{58}Ni, \alpha n)^{155}Hf^* \tag{4.2}$$

At this beam energy, it is expected that the $2p3n$ channel will be stronger than the $\alpha\, n$ channel. Particularly at the center of the target, where the beam loses some energy in the target.

Previous studies of $N = 83$ isotones above Gd $(Z = 64)$ have revealed a lowering in excitation energy of $\nu i_{13/2}$ single particle state with increasing proton number [61, 62, 63]. A similar phenomenon had been observed in the $\nu h_{9/2}$ single particle state. This behaviour is attributed to the protons that fill $h_{11/2}$ orbits and the strong P-N interaction between the pairs in the state $(\pi h^2_{11/2})$ 0^+ and $\nu h_{9/2}$ in the anti-parallel $\pi\ h_{11/2}\ \nu h_{9/2}$ configuration [64]. These trends are interesting as they demonstrate the effects of adding an individual neutron into a nuclear system at the extremes of stability. The constructed ^{155}Hf level scheme and assigned nucleon configurations are compared with neighbouring $N =$ 83 isotones and systematic trends are discussed. The isomer half-life has been measured, which, when compared to Weisskopf estimates for the transitions directly depopulating the isomer, supports the assignment of the isomer to a $27/2^-$ state.

There are several considerations that must be taken into account in this study to overcome the constraints implied by decay nature and the location of ^{155}Hf in the Segrè chart. Figure (4.1) indicates the decay scheme of ^{155}Hf. Applying the RDT method in this region is challenging because correlations with subsequent α decays are delayed by intervening β emissions that are relatively long lived. This will give a rise to a significant decay background to appear in the spectrum due to randomly correlated events. This study relies on the capabilities for the mass-selection of the MARA separator used in conjunction the JYU-Tube, which will veto reaction channels arising from charged particle evaporation.

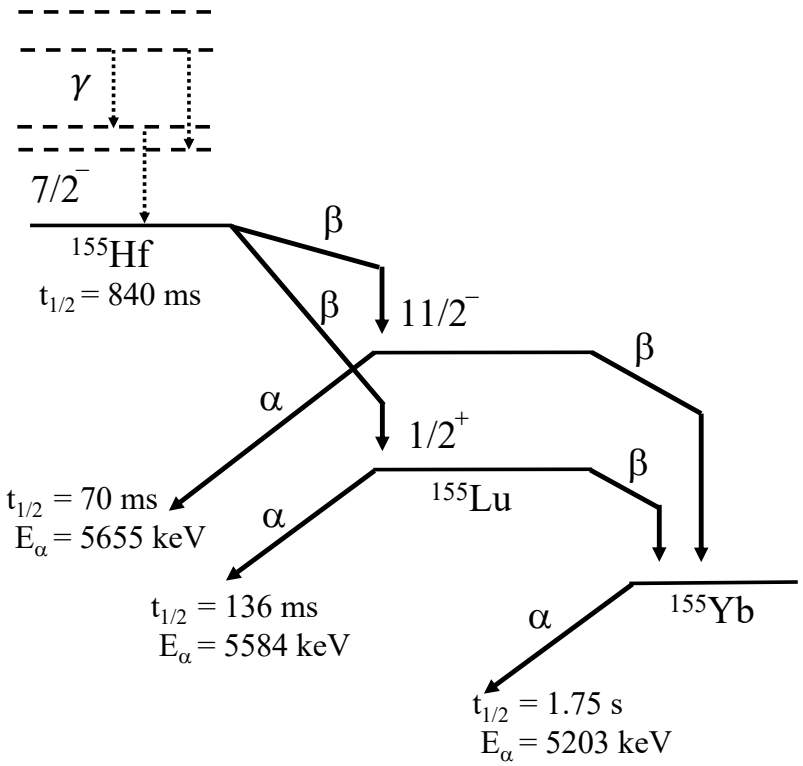

Fig. 4.1 Schematic decay scheme of ^{155}Hf.

Another factor to consider is that the alpha particle emitted from the $1/2^+$ state in ^{155}Lu has an energy of 5584 *keV* while ^{156}Lu has a 9^+ alpha decaying state of energy about 5564 *keV* [65, 66]. Since they are only about ~ 20 *keV* apart they are expected to overlap and appear in the spectrum as one peak. They are indistinguishable even when the veto detector is used. When using alpha decay from this state and analysing the coincidence gamma-ray spectrum,

it is expected to be dominated by ^{156}Lu gamma transitions that depopulate its 19^{-} isomer [56].

4.2 Results and Discussion

The distinguishing properties of recoils, scattered reaction products and the unreacted beam in terms of their TOF make it possible to set a selection limit on the recoils group identified in figure (3.21). Based on these properties, true implantation events can be discriminated by requiring that they comply with a two-dimensional selection condition, namely the time of flight between the two detectors, MWPC and DSSD, and the implantation energy of the DSSD. Figure (4.2) shows a plot of TOF versus DSSD implantation energy signals after setting the 2D gate to only select recoils ions and excluding unreacted beam particles and scattered reaction products.

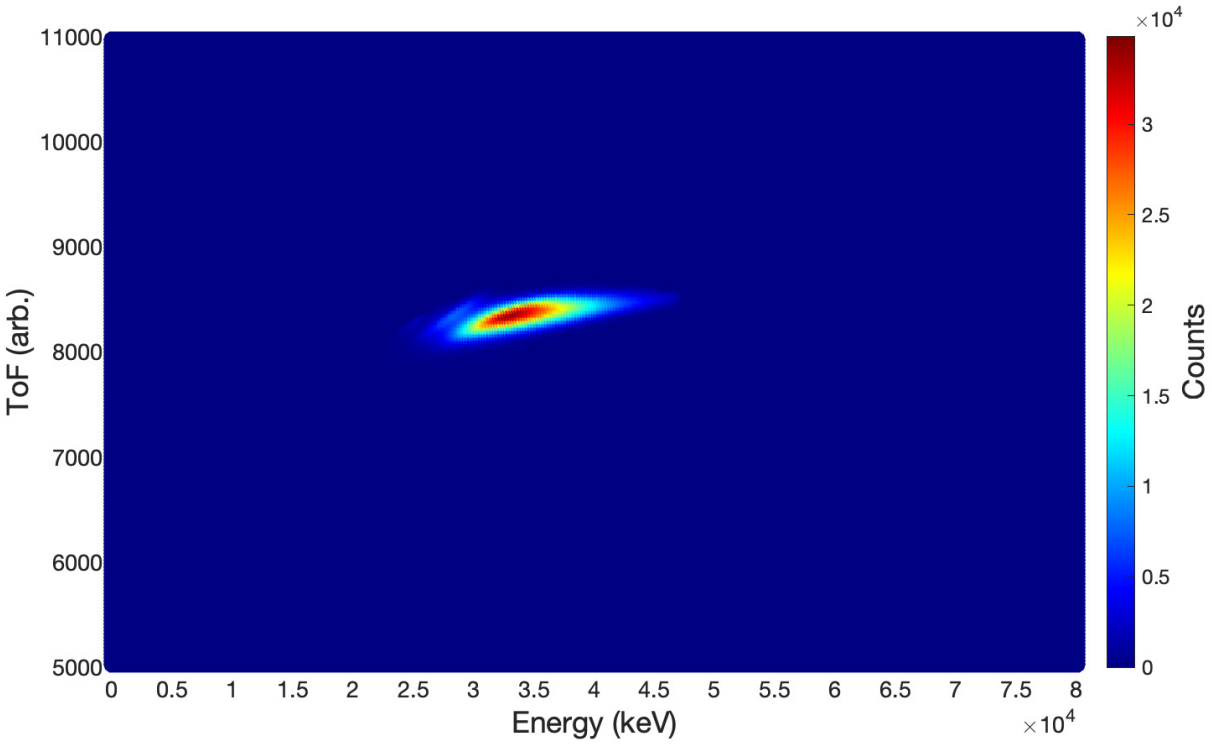

Fig. 4.2 Plot of the energy deposited in the DSSD as a function of flight time between the MWPC and the DSSD. Fusion-evaporation residues are distinguished from other implantations, shown in figure (3.21), based on a two-dimensional selection process.

The RDT technique has been used to search for an isomer in ^{155}Hf. However, a substantial degree of selectivity is likely to be required to distinguish relevant alpha decays used as tags from other strongly produced nuclei. In figure (4.3), all the alpha decays that occur within eight seconds of an implanted fusion-evaporation residue event are shown.

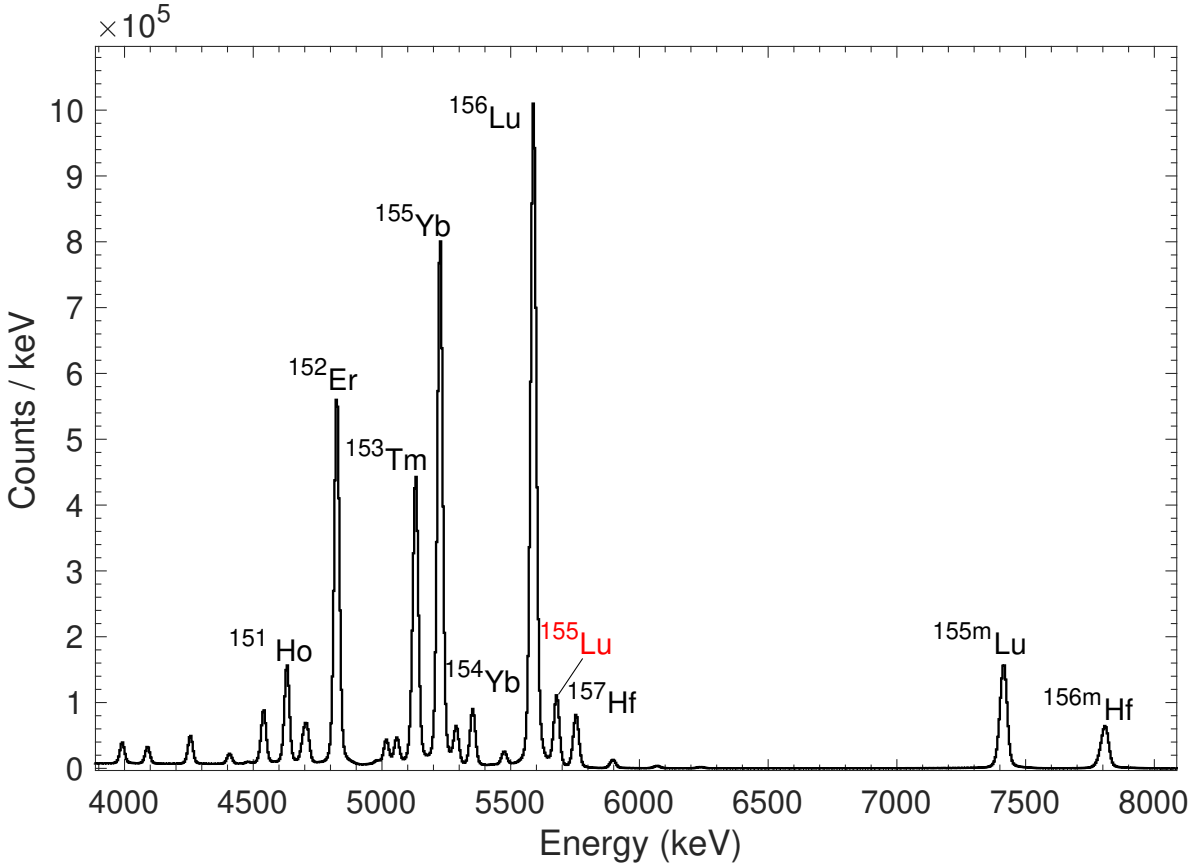

Fig. 4.3 All alpha decays that occur within 8 *s* following an implanted fusion-evaporation residue event. The strongest peaks are labelled.

The subsequent decays of fusion evaporation residues are required to occur within the same DSSD pixel as implantation occurs in order to reduce the probability of false coincidences. The large level of background present in the alpha spectrum may result in false correlations between signals from the germanium detectors and recoils identified by corresponding alpha decay. False correlations are caused by the previously described mismatch between recoils and alpha decays. This is particularly a problem when the production cross section is small as the case for ^{155}Hf. This could be improved somewhat by setting a time gate between

the implantation of recoils and the alpha decay. For example, setting 200 *ms* to 4.5 *s* time window between the recoil implantation and the alpha decay of the ground state of ^{155}Lu reduced the counts of the observed alpha peak from 6.3 $\times$ 10^6 to 8.2 $\times$ 10^5 . However, since the DSSD has a per channel dead time of approximately 8 μs, some mismatches between events cannot be avoided.

4.2.1 Gamma-ray identification

Gamma-ray spectroscopy is possible with the germanium array located at the focal plane which allow for the detection of delayed emission gamma-ray energies. The RDT technique makes it possible to separate transitions belonging to ^{155}Hf from the high γ-ray background using the characteristic α decays of ^{155}Lu. Figure (4.4.A) shows a spectrum of gamma rays measured by the focal-plane germanium detectors within 8.0 μs of the implantation of an evaporation residue into the DSSD. Gamma rays from long-lived decays, such as ^{153}Yb, ^{154}Lu and ^{150}Er, are visible in the spectrum. These can be removed by subtracting the spectrum from another obtained by using the same conditions but changing the time between recoil implantation and gamma ray detection to $8.0 - 10.0$ μs. Additionally, by reducing the time window allowed for the correlation between gamma rays detected in the germanium detectors and the recoil implantation, the long-lived transitions from isomers and the random correlations will be reduced. Furthermore, adding the condition of only collecting gamma rays with recoil-decay events improves the quality of the spectrum. Figure (4.4.B), illustrates a background-subtracted gamma-ray spectrum correlated with recoils followed by an alpha decay in the same pixel within 4.5 *s*. Peaks from the strongly produced nuclei ^{156}Lu and ^{158}Lu can be observed.

As shown in figure (4.1), ^{155}Hf has a half-life of 840 *ms* and decays to the $11/2^-$ and $1/2^+$ level in ^{155}Lu which decay by emitting alpha particles with energies of 5655 *keV* and 5584 *keV*, respectively. Therefore, tagging on either alpha decay should return any gamma-ray transitions belong to ^{155}Hf. Figure (4.4.C) shows gamma-ray spectrum correlated with the alpha decay of the ground state in ^{155}Lu, where more than 10 clear peaks can be seen. In

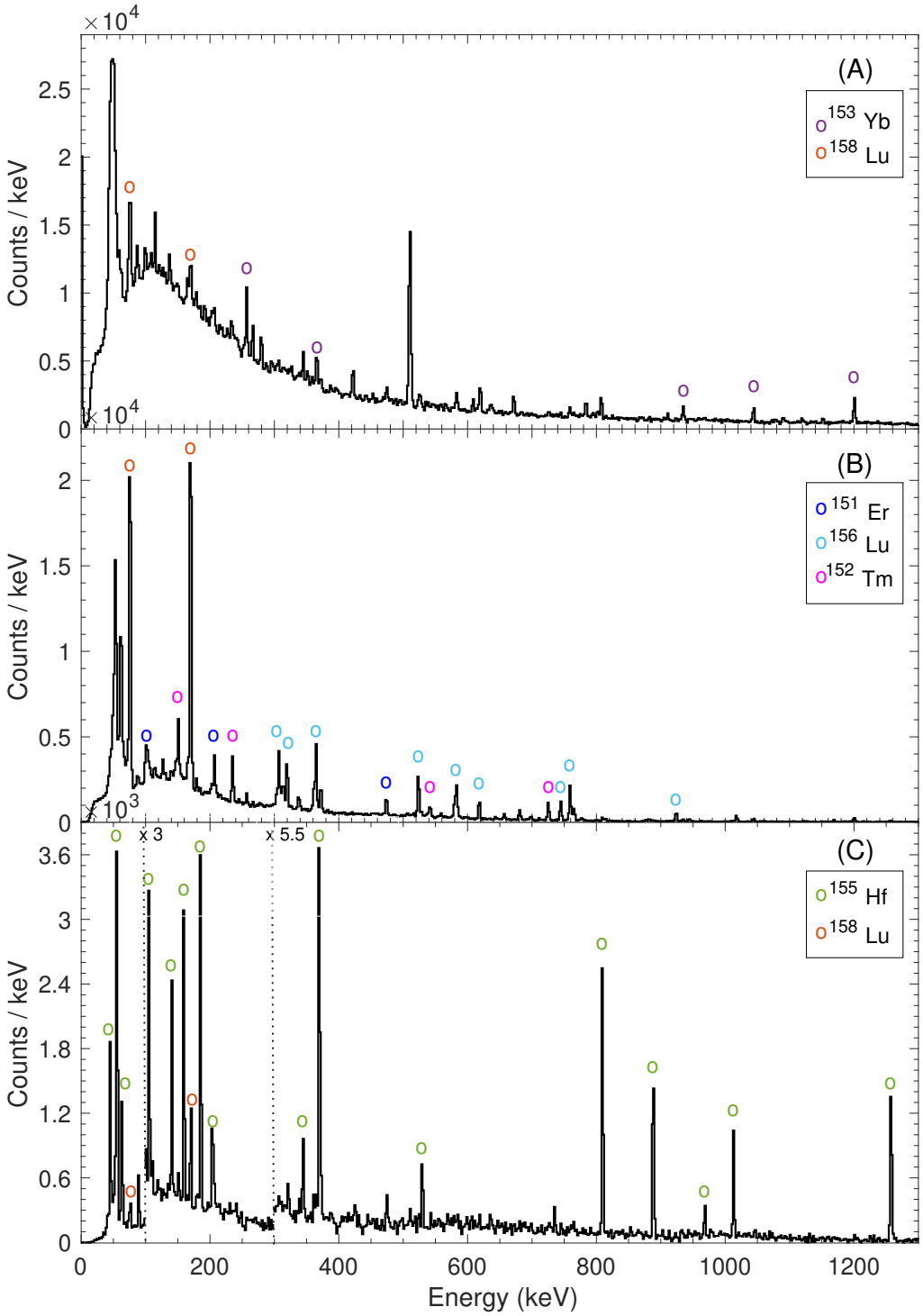

Fig. 4.4 Energy spectra of gamma rays observed in the focal-plane germanium detectors. A) All gamma rays were recorded within 8.0 μs of an evaporation residue implanted into the DSSD. (B) A background subtracted spectrum of gamma rays recorded within 8.0 μs of a recoil implanted into the DSSD that was followed by an alpha decay within 4.5 s in the same DSSD pixel. Emissions can be observed from the strongest reaction channels ^{156}Lu and ^{158}Lu. (C) The same conditions as in (A), with the additional requirement that the alpha decay that follows is only from ^{155}Lu ground state decay of 5655 keV.

figure(4.5), the same gamma-ray spectrum is shown with each peak identified by a text label. A gaussian with a polynomial background function was used to fit each peak in the figure to calculate the precise energy of the gamma decays. Using equation (3.11), the intensity of the transitions was calculated and corrected for detection efficiency. The energies and intensities of these gamma rays are shown in table (4.2).

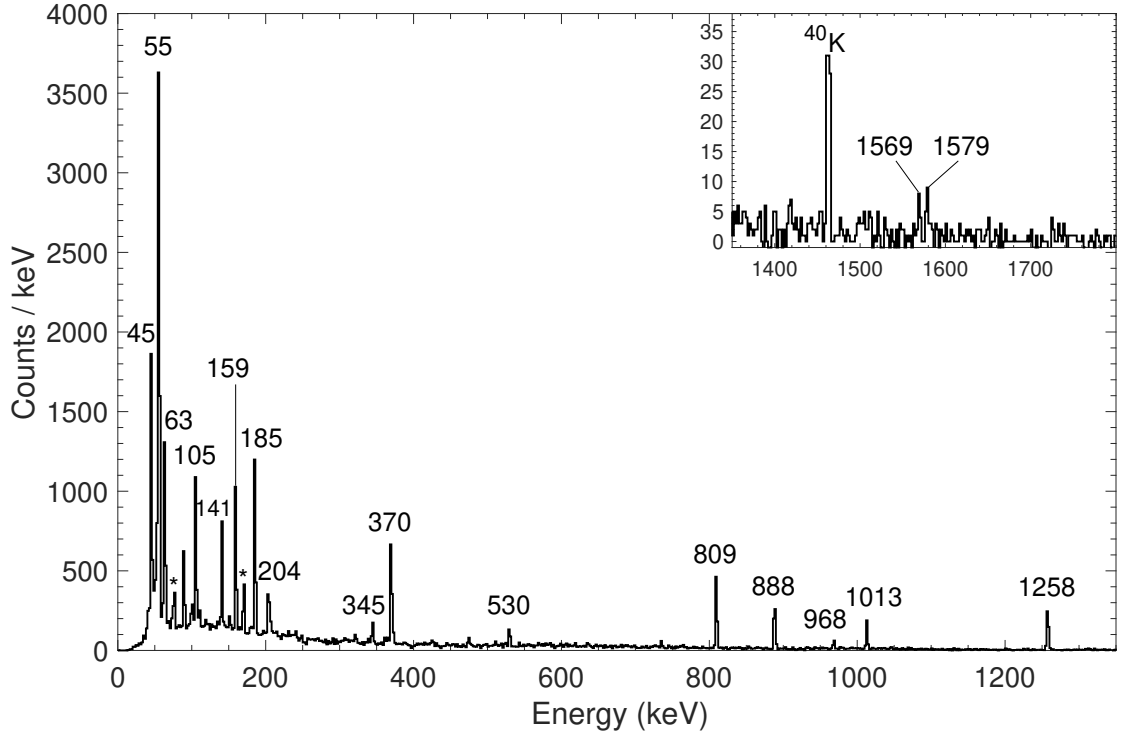

Fig. 4.5 Energy spectra of γ-rays obtained using the RDT technique tagging on alpha decays from the $11/2^-$ state of ^{155}Lu with a 4.5 *s* correlation time. The inset shows the high energy region of the spectrum. Peaks highlighted with stars belong to ^{158}Lu [35].

The situation is different when the alpha decay of the low spin isomer state in ^{155}Lu was used for correlation. Although at the high energy end of the spectrum one can observe the same peaks, 809, 888 and 1258 keV, with low intensity, it was not possible to eliminate the strong peaks that are shown in figure (4.6). These transitions belong to the ^{156}Lu isomer. The half-life reported for this isomer is $179(4)$ *ns*, while that for alpha decay is $198(2)$ *ms* [50, 56]. By comparing it with the 136 *ms* half-life for the decay of $1/2^+$ state, clearly, the two cannot be separated. Even if we used the advanced features of MARA separator and

JYUtube detector, it is still consider a challenging process to separate the two when the difference between the mass number and the number of evaporated particles is only one. The X distributions of ^{155}Hf and ^{156}Lu evaporation residues traveling through the MWPC before being implanted in the DSSD, identified through subsequent gamma decay measurements are shown in figure (4.7). This illustrates the difference in their masses (per charge). Since the statistic is much higher in alpha peaks, correlating recoils with alpha decay will provide a more accurate picture of the distribution. Accordingly, the alpha decays of ^{157}Hf, ^{156}Hf and ^{155}Lu, have been used as indicators of the distribution of masses 157, 156 and 155. The number of counts is sufficient to determine the centroid position of each of the four transmitted charge states. It can be observed that with a decrease in mass number, recoils shift to the left since they are more easily deflected by the magnetic field than heavier recoils. Despite this small shift, overlap cannot be avoided.

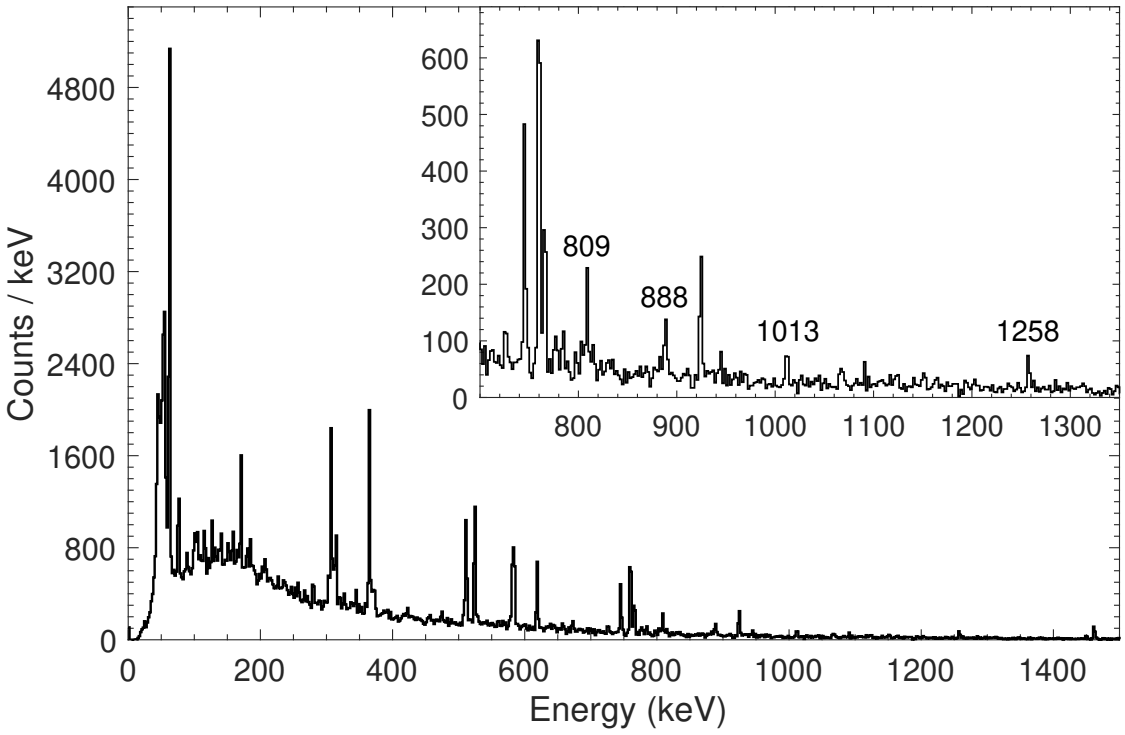

Fig. 4.6 Energy spectra of γ-rays obtained using the RDT technique tagging on a doublet alpha peak from the decay of $1/2^+$ state in ^{155}Lu and the 10^+ state of ^{156}Lu with a 4.5 s correlation time.The inset shows the high energy region of the spectrum where peaks from ^{155}Hf are labelled.

Further evidence that the detected gamma rays belong to the ^{155}Hf isomer was found by measuring the number of evaporated charged particles detected in JYUtube associated with the recoils. The results are plotted in figure (4.8) where the tube fold in correlation with gamma decay for ^{155}Hf and ^{158}Ta and with alpha decay for ^{155}Lu and ^{157}Hf. The distributions in each panel are consistent with the production channel. Furthermore, analysing the change of intensity for individual gamma when all sort parameters are fixed as a function of the number of evaporated particles confirms that the maximum counts occur in the corresponding evaporation channel. This method has been validated using transition from ^{158}Ta and ^{156}Lu isomers. The results are shown in figure (4.9). Additionally, the distribution of the alpha decay of the $11/2^+$ state following the fusion evaporation residue implantation, within the same pixel of the DSSD can be compared with the distribution other recoils having the same mass number. The x-y position within the DSSD is displayed for ^{155}Hf in figure (4.10) in comparison with the position of the high-spin $25/2^-$ isomer ^{155}Lu. The two are clearly in agreement with each other.

4.2.2 Gamma-ray coincidence analysis

In this work, transitions are considered to be coincident if they occur within $\sim 50\ ns$ of each other. A gamma-gamma coincidence analysis was used here in order to construct the decay level scheme shown in figure (4.11). Figures (4.12, 4.13 and 4.14) show examples of coincidence energy spectra of gamma rays observed in the focal plane germanium detectors. Three strong peaks appear on the left side of the spectra in coincidence with all observed gamma rays. Their energies are 45.3 keV, 55.3 keV, and 63.3 keV. The literature values of the Hf X rays are 55.7 keV and 54.6 keV for Kα1 and Kα2 respectively [67]. With a difference of less than one keV between the Kα X-rays energies, the peak at 55.3 keV can be attributed to the sum of the two. The value for the Kβ1 is 63.2 keV, which is consistent with the observed peak.

Figure(4.12) shows the energy spectrum of gamma rays observed in the focal plane detectors in coincidence with the 45 keV, 55 keV and 63 keV transitions. The width of the energy gate was only one keV to prevent any mismatches. In addition to being able to see all the observed

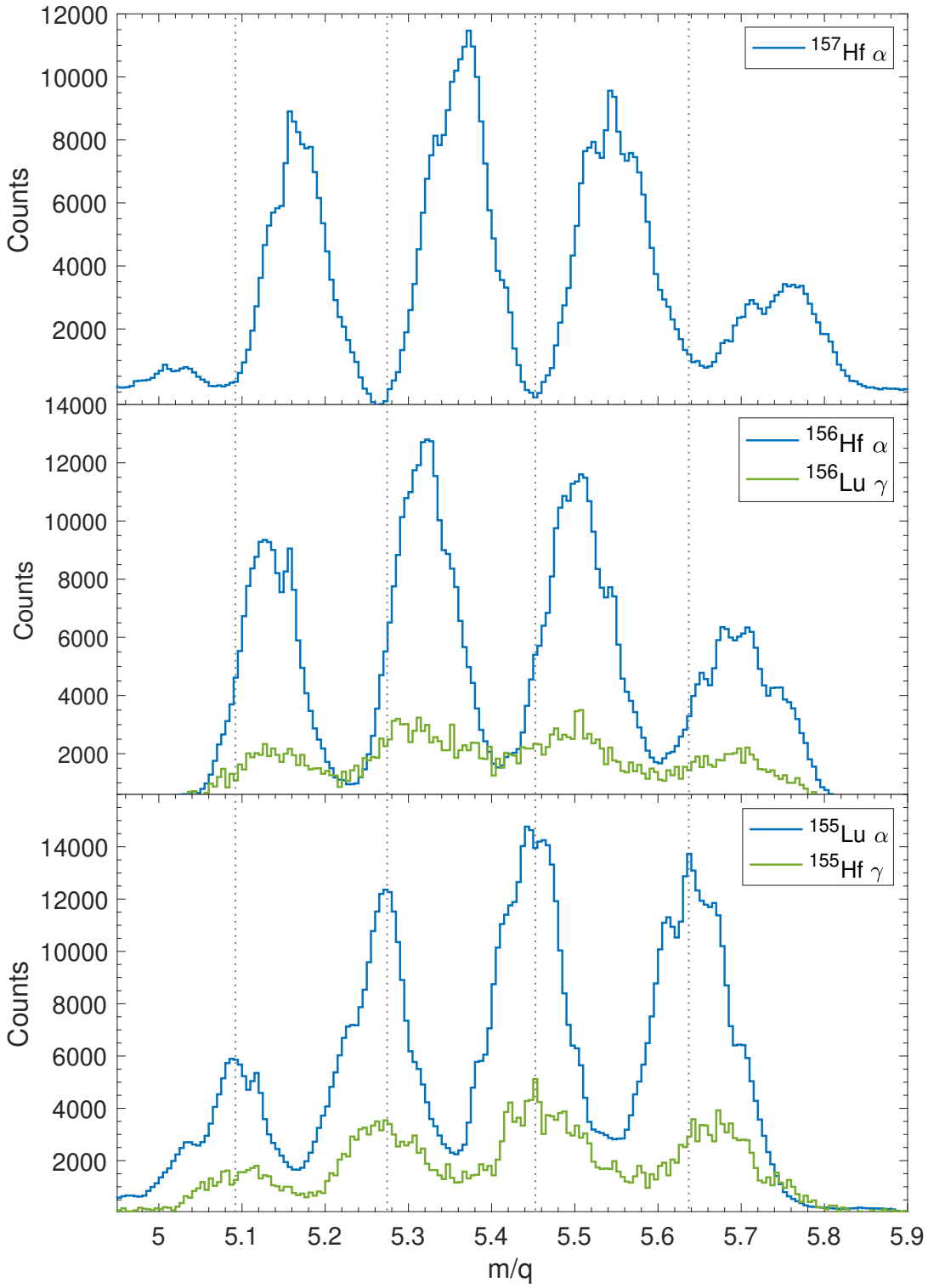

Fig. 4.7 The X position that ^{157}Hf, ^{156}Hf , ^{156}Lu, ^{155}Lu and ^{155}Hf evaporation residues travel through the MWPC before being implanted in the DSSD, determined by subsequent alpha and gamma decay measurements.

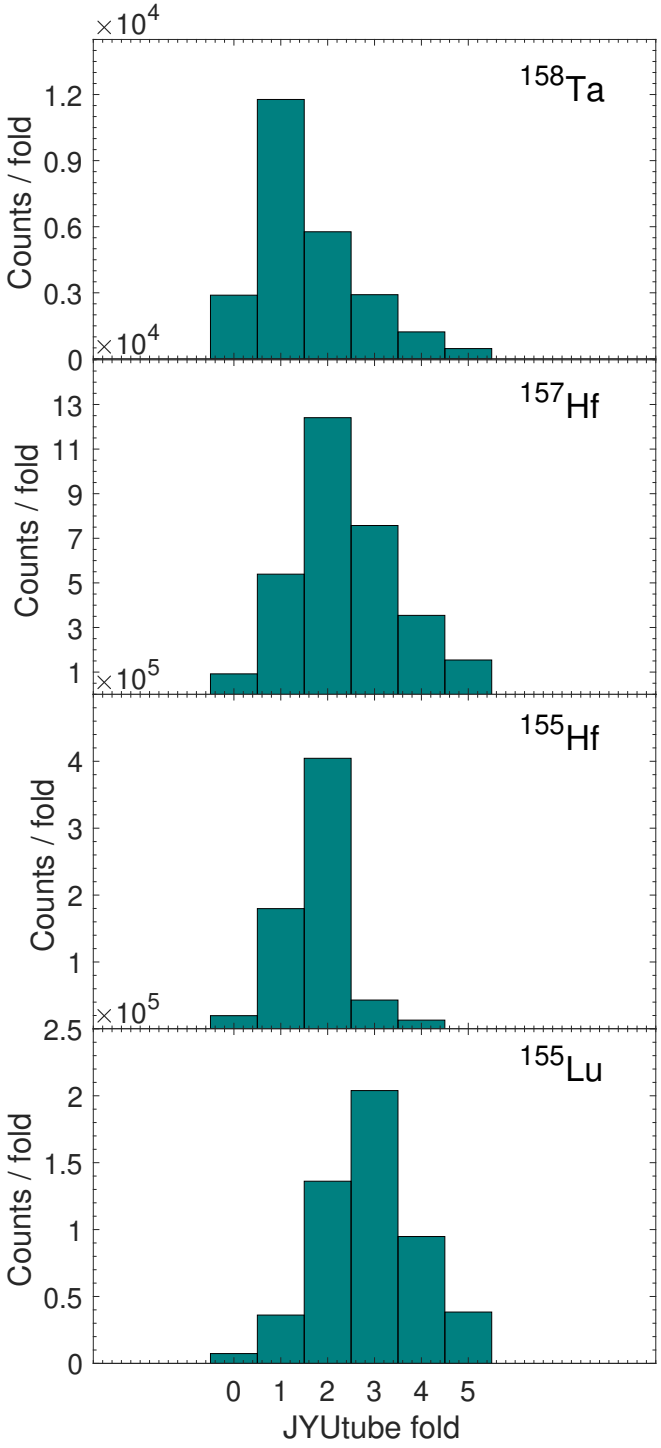

Fig. 4.8 Number of evaporated charged-particles detected in the JYU tube of recoils identified by alpha decay for ^{157}Hf and ^{155}Lu and by gamma transitions depopulating the isomers in ^{155}Hf, ^{158}Ta.

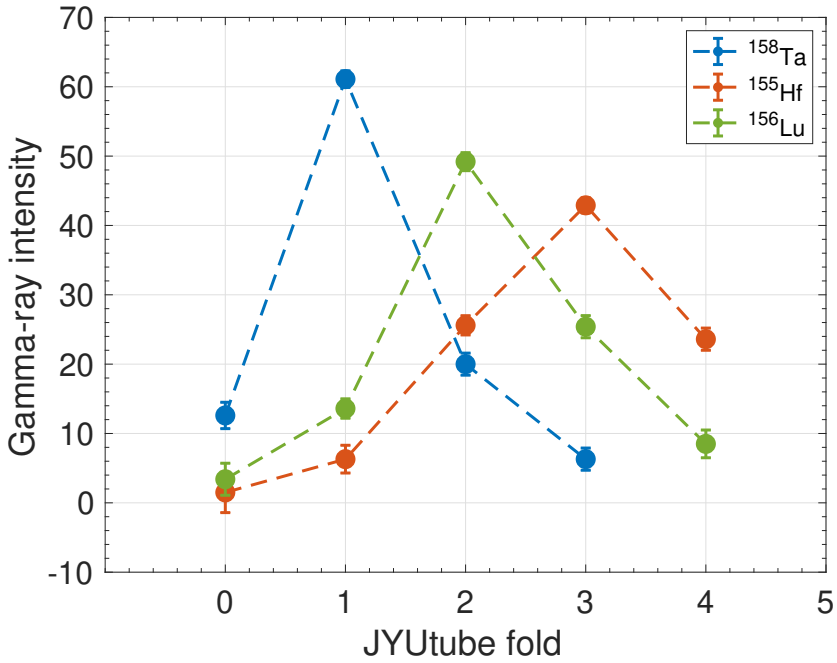

Fig. 4.9 A plot of the individual gamma intensity versus the number of evaporated particles detected by the JYUtube detector for transitions in ^{158}Ta $(1002\ keV)$, ^{155}Hf $(809\ keV)$ and ^{156}Lu $(524\ keV)$.

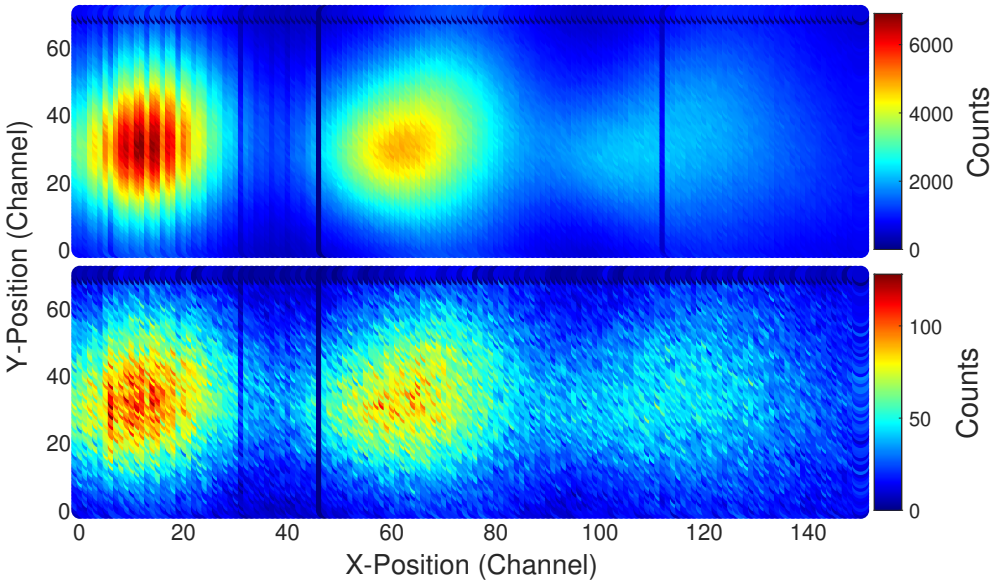

Fig. 4.10 The DSSD x-y position of ^{155}Hf recoils (bottom) in comparison with the distribution of ^{155}Lu (top). Recoils are identified by the alpha decay of the ground state in ^{155}Lu for ^{155}Hf and by the high-spin $25/2^-$ isomer state in ^{155}Lu.

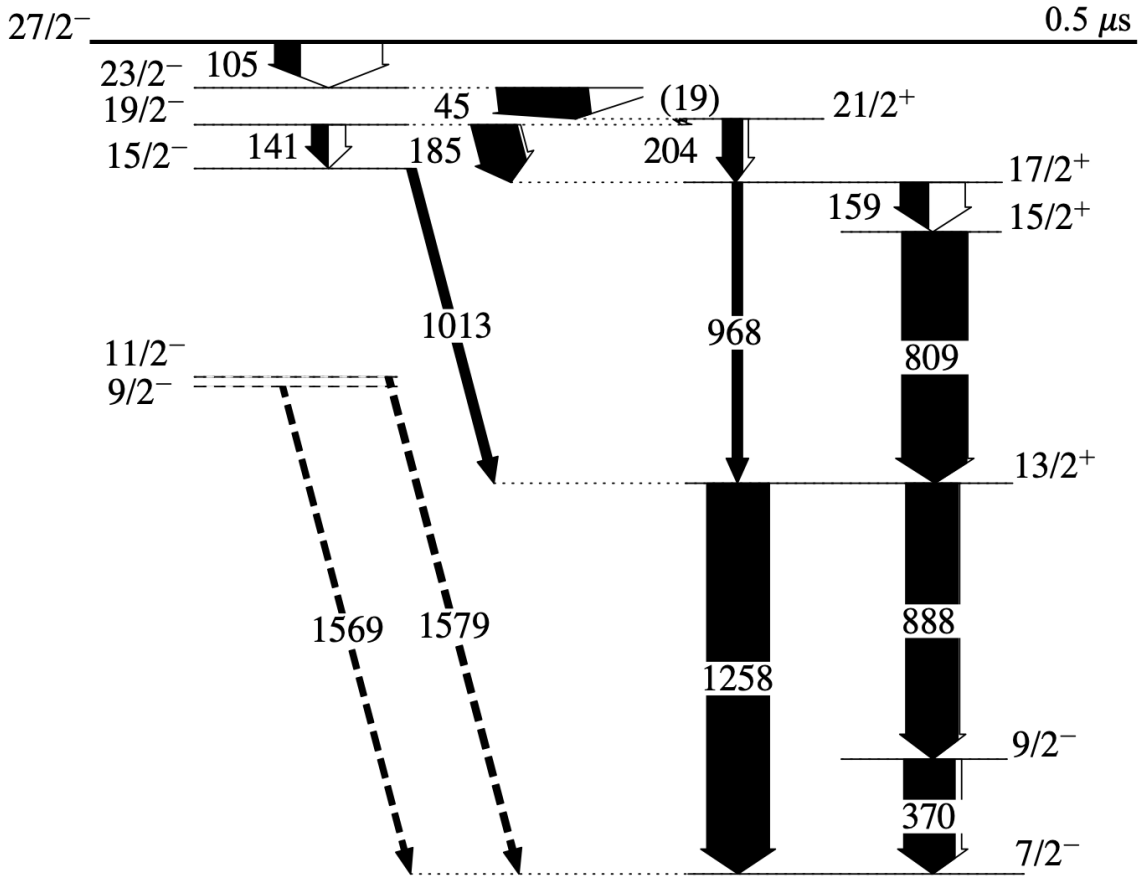

Fig. 4.11 The proposed decay scheme of the $27/2^-$ isomer state in ^{155}Hf. The unobserved 18.8 *keV* is presented in the level scheme as a tentative gamma ray. The $9/2^-$ and $11/2^-$ levels are indicated by dashed lines because they have been placed in the level scheme based on the systematics of $N = 83$ isotones alone and no coincidence information was available.

gamma rays, the X rays also detect their own emission. The ratio of the Kβ and Kα does not agree with the literature values which is about $0.088(0.004)$ [68]. It appears that some events from the 55 *keV* peak were lost. Therefore, a careful examination of the 45 *keV* transition has been conducted since this peak lies at about the same energy as the X-ray escape peak for a germanium detector.

By investigating the presence of an X-ray escape peak in the gamma ray spectra for different isomers produced in this study, such as ^{153}Yb and ^{156}Lu in figures (3.22) and (3.15), respectively, it can be concluded that this is not the origin of the 45 *keV* peak. Furthermore, as indicated in the figure, gating on the 45 *keV* peak does not return itself in contrast to the X-ray peaks. This confirms that the peak is from a gamma-ray transition and therefore part of the same cascade as the low-energy transitions. In all the coincidence panels, figure (4.13 and 4.14) except for the 105 *keV* coincidence window, the 45 *keV* peak appears to be more intense than the Kα X-ray peaks. It demonstrates how highly converted the 105 *keV* transition is. Table (4.1) presents the internal conversion coefficients for $E1$, $M1$, and $E2$ for all identified gamma ray energies.

From panels (A), (C) and (D) in figure (4.13) and the coincidence window of 45 *keV* it can be seen that the four transitions; 45, 105, 159 and 185 *keV* are in coincidence with each other. Additionally, figure (4.14.A) shows gamma rays correlated with the 809 *keV* transition. As can be seen, most of the transitions are visible in the spectrum. However, it misses the peak at 1013 *keV*. Therefore, it can be concluded that the two transitions are parallel. Taking into consideration panel (C), the placement of the transition in the level scheme was determined. As a result of the low statistics and the decrease in efficiency with increasing energy, the 1013 *keV* and 1258 *keV* transitions could not be detected in coincidence with one another. Additionally, although it was not possible to observe the 1013 *keV* peak in coincidence with the 888 *keV* transition, using the 370 *keV* combined with the 888 *keV* showed an increase in the intensity of 1013 *keV*, as shown in panel (E). Moreover, the coincidence windows do not indicate a peak at 968 *keV*, so this transition is placed in the level scheme on the basis that its energy is the sum of 159 *keV* and 809 *keV*.

One features of these coincidence spectra is that they demonstrate that there is no coincidence

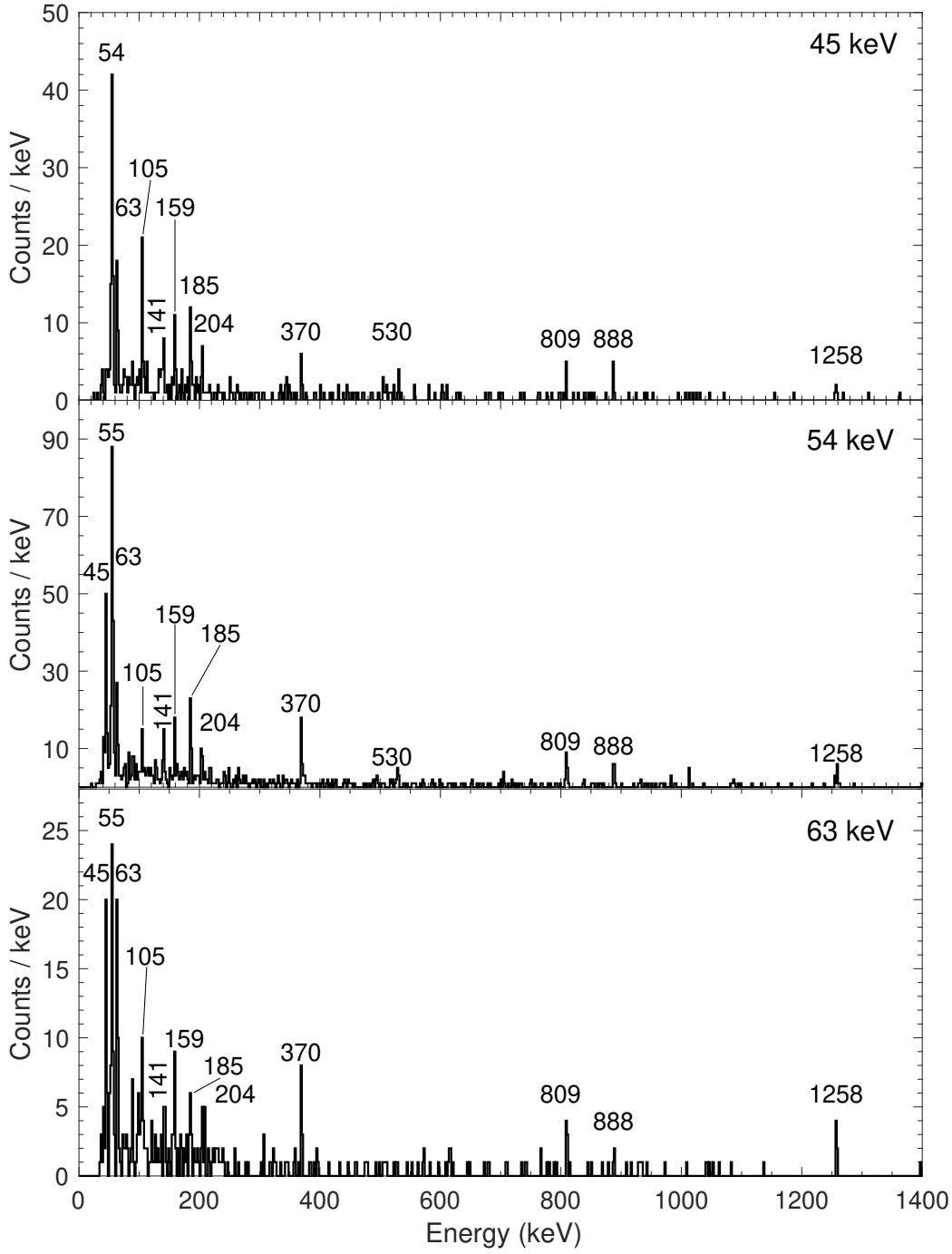

Fig. 4.12 Energy spectra of gamma rays observed in the focal-plane germanium detectors. All gamma rays were recorded within 8 μs of an evaporation-residue implantation into the DSSD that was followed in the same DSSD pixel by a 5655 keV ^{155}Lu alpha decay within 4.5 s. Gamma rays are detected in coincidence with the peaks at energy of 45 keV, 54 keV and 63 keV in each panel.

between the 370 *keV* and 1258 *keV* transitions. Therefore, they are placed in parallel with each other. This is shown in panel (E) in figure (4.13) and panel (D) in figure (4.14). Other transitions which also seem to be in parallel with the 1258 *keV* transition, indicated in panels (B) and (D) in figure (4.14), is the 888 *keV* transition, whose energy is summed with 370 *keV* to give 1258 *keV*.

The 204 *keV* connecting transition between the $21/2^+$ and $17/2^+$ levels, would indicate the presence of energy gap of 18.8 *keV* between the $21/2^+$ and the $19/2^-$ state. Even though it has not been observed, it must be present due to the coincidence between the 105 *keV* and 45 *keV* transitions with the 141 *keV* and 185 *keV* transitions. This gamma ray is likely to be absorbed by the materials due to its low energy. Another transition that could be expected is a 63.8 *keV* $E2$ gamma ray between the $23/2^-$ and the $19/2^-$ states, which has an analogous 97 *keV* weak gamma-ray transition in ^{153}Yb. It is, however, unlikely to compete with the 45 *keV* $(E1)$ transition on the basis of the Weisskopf estimate of its half-life of 10.86 μs.

Furthermore, despite the observation of weaker peaks at 530 *keV* and 345 *keV* in figure (4.5), it was not possible to place these two gamma rays in the proposed level scheme. The 530 *keV* transition was found to be in coincidence with 185 *keV*, 159 *keV* and 105 *keV* gamma rays while the 345 *keV* transition was observed in coincidence with then 888 *keV*, 809 *keV*, 370 *keV*, 204 *keV*, 185 *keV*, 530 *keV* gamma rays. Moreover, it is necessary to point out that the tentative 1569 *keV* and 1579 *keV* gamma rays have been placed in the level scheme based on the systematics of $N = 83$ isotones only and there was no coincidence information to support this assignment.

4.2.3 Half-life of the isomeric state

In order to determine the half-life of this state, time differences were measured between implanted recoil signals in the DSSD and detected ^{155}Hf gamma rays in the focal plane germanium detectors. Figure (4.15) illustrates the decay curve of the collected data. A measured half-life of $509(22)$ *ns* has been obtained following the fitting of the decay curve to these data after a background was subtracted. Data points between $7\mu s$ and $8\mu s$ were used to calculate an average background. The fit of this decay curve can be seen in figure (4.16).

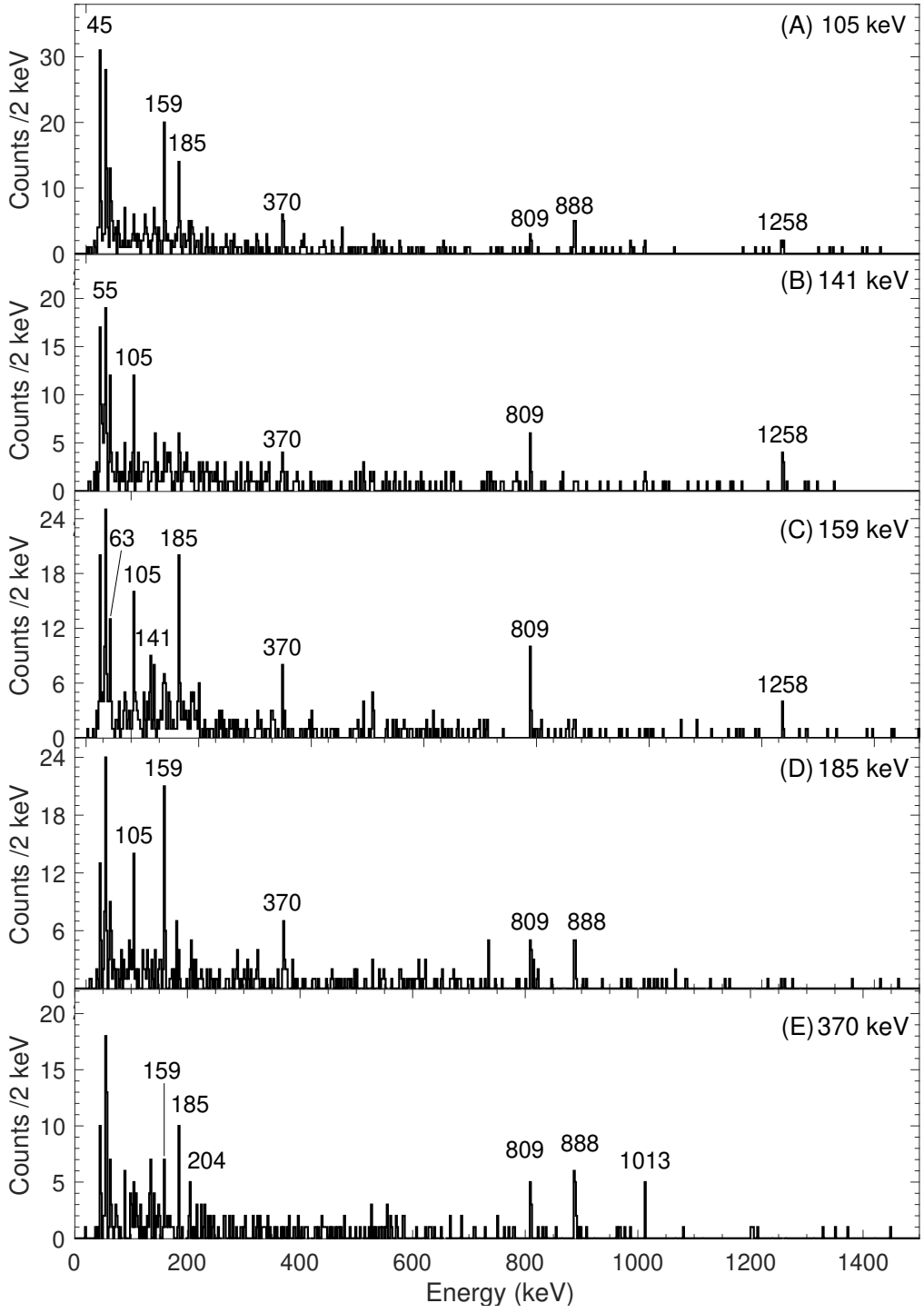

Fig. 4.13 Coincidence energy spectra of gamma rays observed in the focal plane germanium detectors. All gamma rays were recorded within 8 μs of an evaporation-residue implantation into the DSSD that was followed in the same DSSD pixel by a 5655 keV ^{155}Lu alpha decay within 4.5 s. Gamma rays are detected in coincidence with a gamma ray of energy (A) 105 keV, (B) 141 keV, (C) 159 keV, (D) 185 keV and (E) 370 keV.

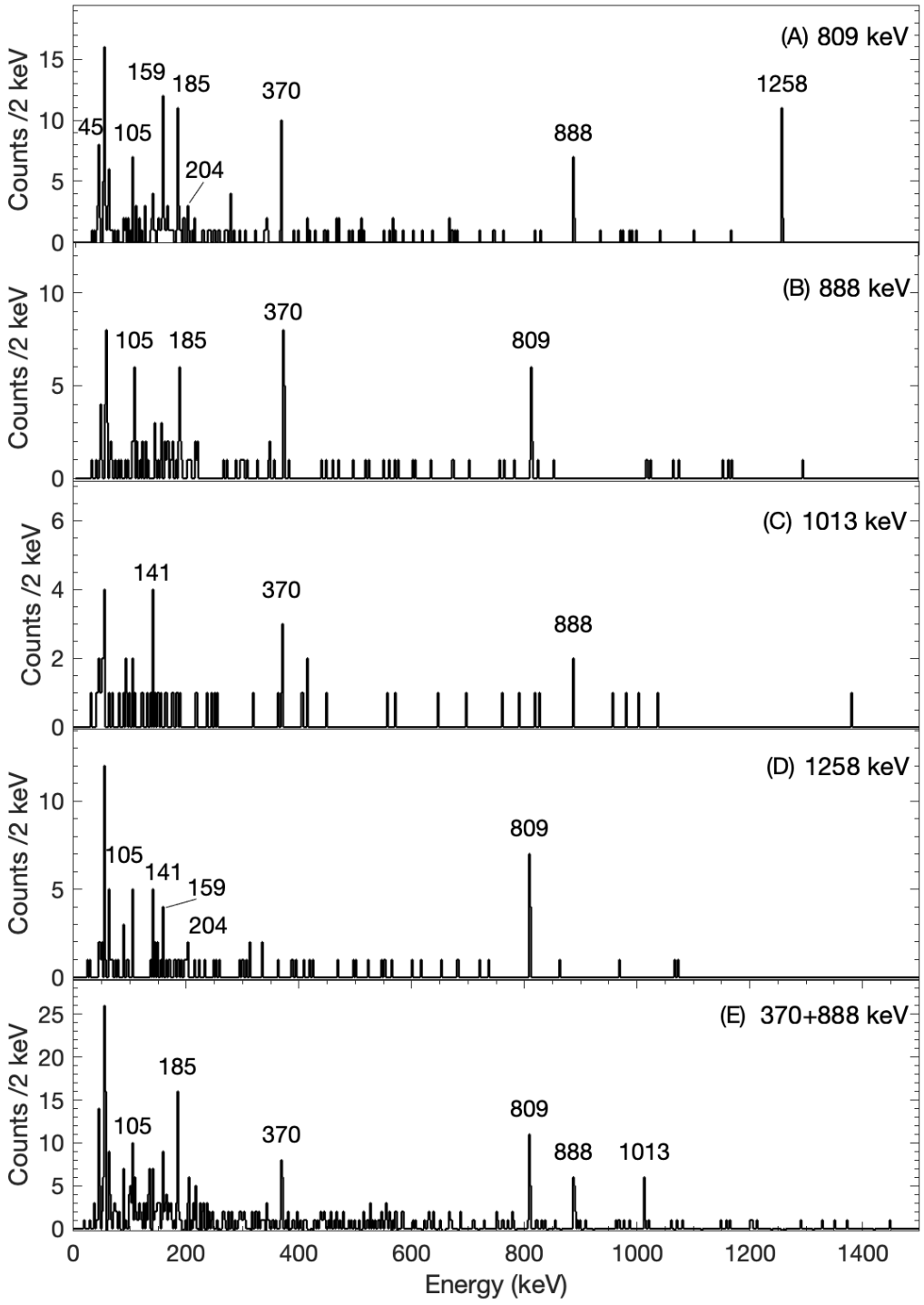

Fig. 4.14 Energy spectra of gamma rays observed in the focal-plane germanium detectors. All gamma rays were recorded within 8 μs of an evaporation-residue implantation into the DSSD that was followed in the same DSSD pixel by a 5655 keV ^{155}Lu alpha decay within 4.5 s. Gamma rays are detected in coincidence with a gamma ray of energy (A) 809 keV, (B) 888 keV, (C) 1013 keV, (D) 1258 keV and (E) both 370 and 888 keV.

Table 4.1 Internal conversion coefficients for E1, M1, and E2 detected gamma ray energies. The values were calculated using BrIcc [18].

Energy (keV)	Multipolarity		
	E1	M1	E2
45.3	0.573	6.759	114.0
105.4	0.312	3.445	2.875
140.9	0.146	1.505	0.971
159.5	0.1058	1.061	0.624
185.5	0.071	0.694	0.370
204.3	0.056	0.531	0.267
344.6	0.015	0.0128	0.052
369.6	0.013	0.106	0.043
529.8	0.006	0.041	0.017
809.5	0.002	0.014	0.006
888.3	0.002	0.011	0.005
968.5	0.002	0.009	0.004
1013.1	0.002	0.008	0.004
1257.7	0.001	0.005	0.003
1569.1	0.001	0.003	0.002
1578.9	0.001	0.003	0.003

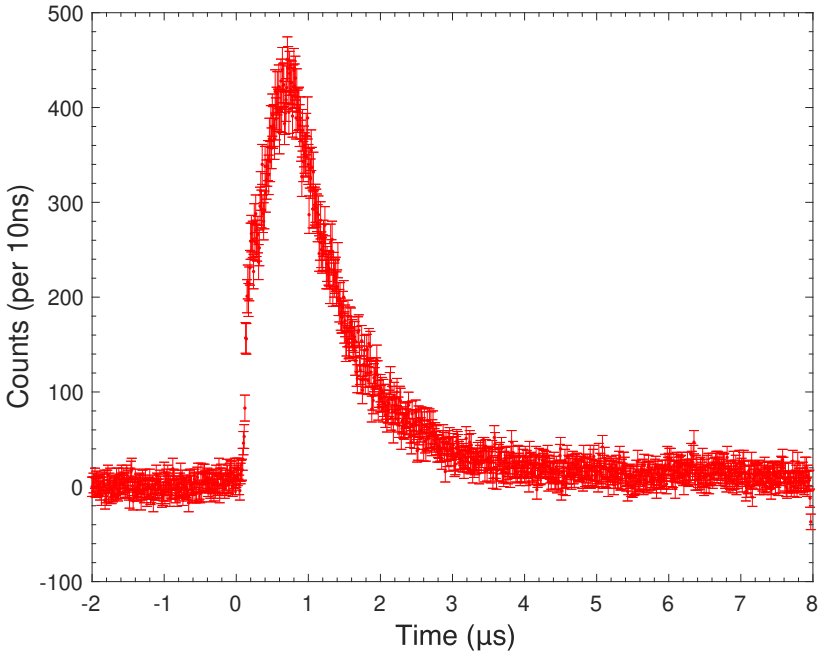

Fig. 4.15 Time between recoil implantation and gamma rays populated the isomer in ^{155}Hf detected at the focal plane. The fitted half-life is shown in figure (4.16).

It has been predicted that the isomer would have a long half-life, as in the isotones ^{149}Dy and ^{151}Er, where half-lives of 0.5 s and 0.6 s respectively were observed [69, 70]. Also, in ^{154}Lu, the nearest known isotone with an isomeric state, McNeill measured the half-life of the isomer to be 35μs [71]. Furthermore, the observed isomeric half-life in ^{153}Yb is 15 μs [57]. Generally, neighbouring nuclides have longer half-lives than the one found in ^{155}Hf. The half-life values of the isomer in Hf isotopes, were measured as 0.52 ms and 9 μs for the 8^+ state in ^{156}Hf and the 10^+ state in ^{154}Hf respectively [50, 66, 72].

It was possible to produce decay curves for some of the strongest transitions identified in figure (4.5). A weighted fit of an exponential plus a constant background was used to extract the half-life for each the decay curves of 141, 185 and 370 keV. The measured half-lives are 490(30), 493(35) and 510(29) ns of the ^{155}Hf recoil nuclei detected in correlation with the 141, 185 and 370 keV gamma rays respectively. The measured values are consistent with one another and they are in agreement with the value calculated for the isomeric state in figure (4.16).

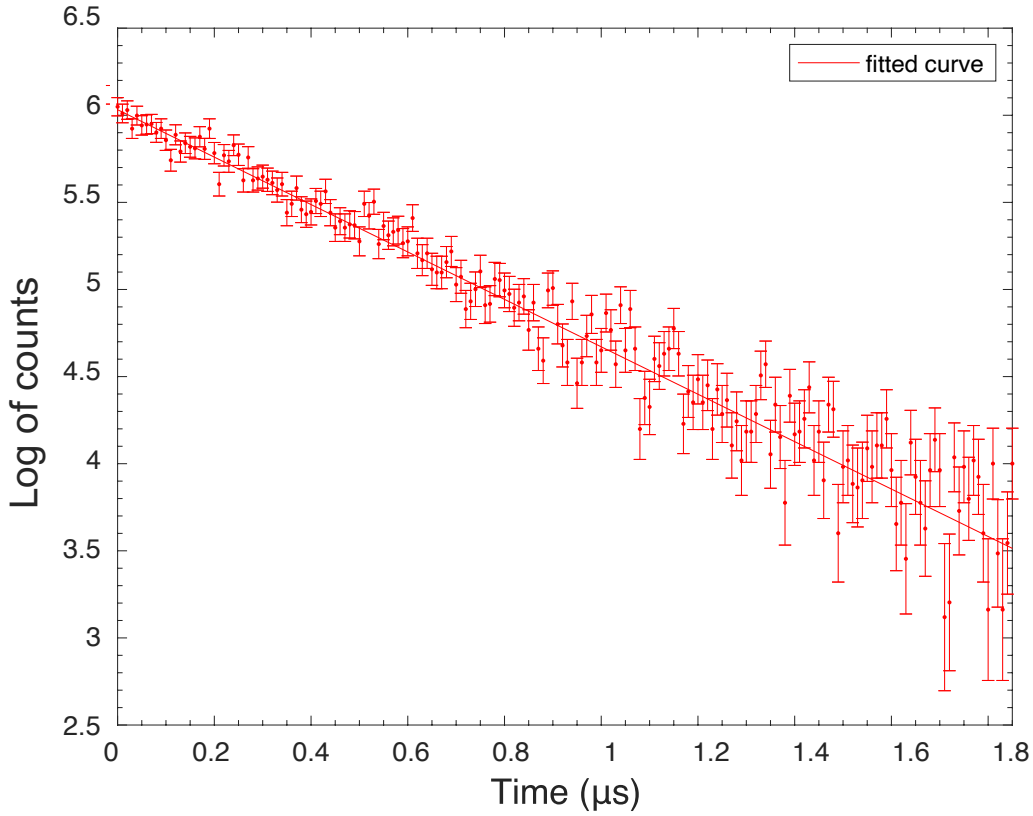

Fig. 4.16 Decay curve for all the transitions below the $27/2^-$ isomer measured in the focal plane detectors. A weighted least-squares fit was applied to the decay curve shown in figure (4.15) for data between 1 μs and 2.5 μs.

4.2.4 Spin-parity assignments

The ^{155}Hf nucleus has eight valence protons ($Z = 72$) and one valence neutron ($N = 83$) above the ^{146}Gd core which exhibits some characteristics of a doubly magical nucleus [61]. Low-lying states in ^{155}Hf originate from couplings between these valence particles. The available neutron orbitals for the valence neutron are $2f_{7/2}, 1h_{9/2}$ and $1i_{13/2}$. As of this work, there have been no previous studies on excited states in ^{155}Hf, except for one estimate of the excitation energy of the $9/2^-$ level by Seweryniak et al [66]. Accordingly, the spin and parity assignment of the ^{155}Hf states is guided by its isotones, in particular ^{153}Yb its nearest even Z isotone. It is expected that the neutron and proton excitation in ^{155}Hf will be the same as those in ^{153}Yb, allowing the structure of the lower-lying states to be determined. Therefore, ^{155}Hf level scheme had been constructed analogously to ^{153}Yb level scheme. The characterized 15 μs isomeric decay of ^{153}Yb was observed by McNeill et al [57]. The proposed level scheme, including the states' spins, parities, and multipolarities, can be seen in figure (4.17).

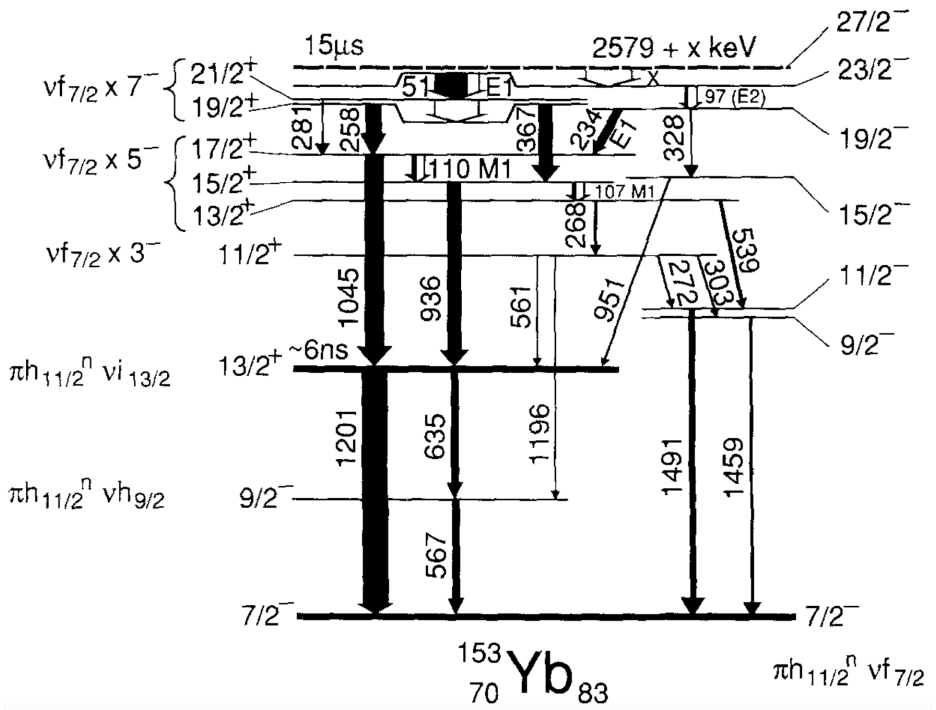

Fig. 4.17 The decay scheme of the $27/2^-$ isomer state in ^{153}Yb with a half-life of 15 μs [57].

In the event that an electromagnetic isomeric transition survives the flight of MARA separator, it is possible for it to either decay by gamma-ray emission or internal conversion. The multipolarity of transitions depopulating the isomer may identified by calculating the lifetimes using Weisskopf single-particle estimates and comparing them with the measured lifetimes. When assigning multipolarity, it is also necessary to take into account the intensity of the transitions between levels, which should be balanced from the isomeric state to the ground state.

The partial energy level scheme is shown in figure (4.11), consisting of transitions below the $27/2^-$ isomer, determined by coincidence analysis with spin and parity constructed from the systematics of $N = 83$ isotones. The isomeric state is a result of seniority $\upsilon = 3$ from the configuration $\pi {h_{11/2}}^n \otimes \nu f_{7/2}$. A highly converted electric transition with a multipole order of two has been assigned to the 105 keV isomeric transition. The internal conversion coefficient for the $E2$ transition is 2.875 which has been obtained from BrIcc [18]. The lifetime measured in the analysis is consistent with the Weisskopf estimate for an $E2$ transition of about $8.839x10^{-07}s$. Furthermore, the intensity balance analysis supports this assignment as well as the spin and parity assignments for the other gamma-ray transitions appearing in the level scheme.

Based on systematics in the $N = 83$ isotones, the 370 keV transition from $9/2^-$ to $7/2^-$ state has been interpreted as an $M1$ transition, where the $9/2^-$ is a result of a $\pi {h_{11/2}}^n \otimes \nu h_{9/2}$ single particle level. The state at 1258 keV is also understood as a single particle excitation $\pi {h_{11/2}}^n \otimes \nu i_{13/2}$ hence giving it a spin-parity of $13/2^+$. The intensity of gamma rays before and after internal conversion with the proposed spin and parity is presented in table (4.2). The isomeric decays also populate the $21/2^+$ and $17/2^+$ states. They result from the coupling of two protons in $(h_{11/2}\, d_{3/2})\ 7^-$ and $(h_{11/2}\, s_{1/2}\,)5^-$ to the $f_{7/2}$ neutron state. However, the $19/2^+$ was not populated here as opposed to in ^{153}Yb, where two gamma-ray transitions, 258 keV and 367 keV, were observed depopulating the state. This suggests that the $19/2^+$ level is closer in energy to the $21/2^+$ state in ^{155}Hf than in ^{153}Yb. Other than this, all of the strong transitions in ^{153}Yb have a counterpart that has been identified in ^{155}Hf.

Table 4.2 Gamma-ray energies and intensities relative to that of the 45 keV transition for transitions below the $27/2^{-}$ isomer in ^{155}Hf. Energies are accurate to $\pm 0.5\ keV$. A correction has been made for the efficiency of detection when calculating intensities. The internal conversion coefficients have been taken from BrIcc, listed in table (4.1), and considered in the corrected intensity column [18].

Energy (keV)	Peak Area	Multipolarity	Corrected intensity
45.3	615 (85)	$E1$	100 (20)
105.4	174 (26)	$E2$	70 (14)
140.9	113 (8)	$E2$	13 (2)
159.5	192 (8)	$M1$	41 (6)
185.5	304 (10)	$E1$	34 (5)
204.3	137 (10)	$E2$	18 (3)
344.6	64 (6)	...	...
369.6	345 (6)	$M1$	39 (6)
529.8	85 (8)	...	...
809.5	440 (9)	$M1$	46 (6)
888.3	351 (10)	$M2$	37 (5)
968.5	65 (10)	$E2$	7 (1)
1013.1	191 (10)	$E1$	20 (3)
1257.7	420 (11)	$E3$	44 (6)
1569.1	35 (12)	$M1$	4 (1)
1578.9	42 (12)	$E2$	4 (1)

4.2.5 The $27/2^-$ isomeric state

The reason for the formation of $27/2^-$ isomers in N=83 nuclei below Z=70 is the strongly attractive two-body interaction of the $(\pi h_{11/2} \otimes \nu f_{7/2})_{9^+}$ particles coupling which reduces the energy of the $[(\pi h^n{}_{11/2})_{10^+} \otimes \nu f_{7/2}]\ 27/2^-$ state below the $[(\pi h^n{}_{11/2})_{8^+} \otimes \nu f_{7/2}]\ 23/2^-$ level, resulting in the generation of E3 isomer [73]. The 9^+ attraction decreases however with filling of the $\pi h_{11/2}$ shell to the point where it could disappear at $Z \approx 70$ when half of the shell has been filled. As a consequence, the $27/2^-$ state may decay to the $23/2^-$ state through the $[(\pi h_{11/2})\ 10^+ \rightarrow 8^+ \otimes \nu f_{7/2}]\ E2$ transition. This has been observed in the neighbouring nucleus $^{154}Hf_{82}$ which has 9 μs half-life [72].

The $27/2^-$ isomer decay is well known among even-Z, $N = 83$ isotones. ^{149}Dy,^{151}Er and ^{153}Yb nuclei have a $27/2^-$ isomers with half-life of 0.5 s, 0.6 s and 15μs [74, 58, 57]. Prior to the observation of the isomer in ^{135}Yb, it was believed that all $N = 83$ isomers decayed via $E3$ gamma-ray emission to the $21/2^-$ as found in ^{149}Dy and ^{151}Er. However, as explained earlier for ^{153}Yb, the isomer in ^{155}Hf was found to decay by $E2$ transition.

B(E2) Systematics

The $B(E2)$ is a specific case of a more general quantity known as the reduced transition probability, which describes the strength of the transition. Its value reflects a change in the nuclear quadruple moment. This describes the deviation of the nuclear charge distribution from a spherical shape, and it is related to the deformation of the nucleus. It is often expressed in Weisskopf units (W.u.) which is for $B(E2)_W = 0.0594\ A^{4/3} e^2 fm^4$ [15]. The value of the $B(E2)$ is equal to the ratio between the half-life obtained from the Weisskopf estimate, corrected for internal conversion, and the half-life measured experimentally.

The 105.4 keV isomeric transition in ^{155}Hf was found to be consistent with $E2$ multipolarity only. Thus, the reduced $E2$ transition rate with a measured 509 (22) ns half-life is equal to:

$$B(E2) = 22.0\ \pm 2.0\ e^2 fm^4 = 0.44\ (4)\ W.u. \tag{4.3}$$

The $\sqrt{B(E2)}$ values for the $27/2^-$ isomeric transitions in the even and odd A, $N = 82$ and $N = 83$ isotones are shown in figure (4.18). The square root gives rise to uncertainty about the signs of a given $E2$ matrix element, however, since they must be opposite in the lower and upper halves of the subshell, it is possible to plot the data points with a negative sign. A negative value has been used for Hf isotopes and ^{153}Lu in the figure.

Although there are only two odd-A, $N = 83$ isotones, ^{153}Yb and ^{155}Hf, for which $B(E2)$ values have been measured for the $27/2^- \longrightarrow 23/2^-$ transition, the two data points are consistent with the observed trend of $B(E2)$. There is a shift observed between the even-A $N = 82, 83$ isotones lines in the figure can be attributed to the $(\pi h^n{}_{11/2})_{27/2} \otimes \nu f_{7/2}$ components of the 15^+ states, resulting in similar contributions to the $17^+ \longrightarrow 15^+$ transition amplitudes in each of the $N = 83$ odd-odd isotones [71]. Such a shift is not seen between the odd-A $N = 82, 83$ isotones lines.

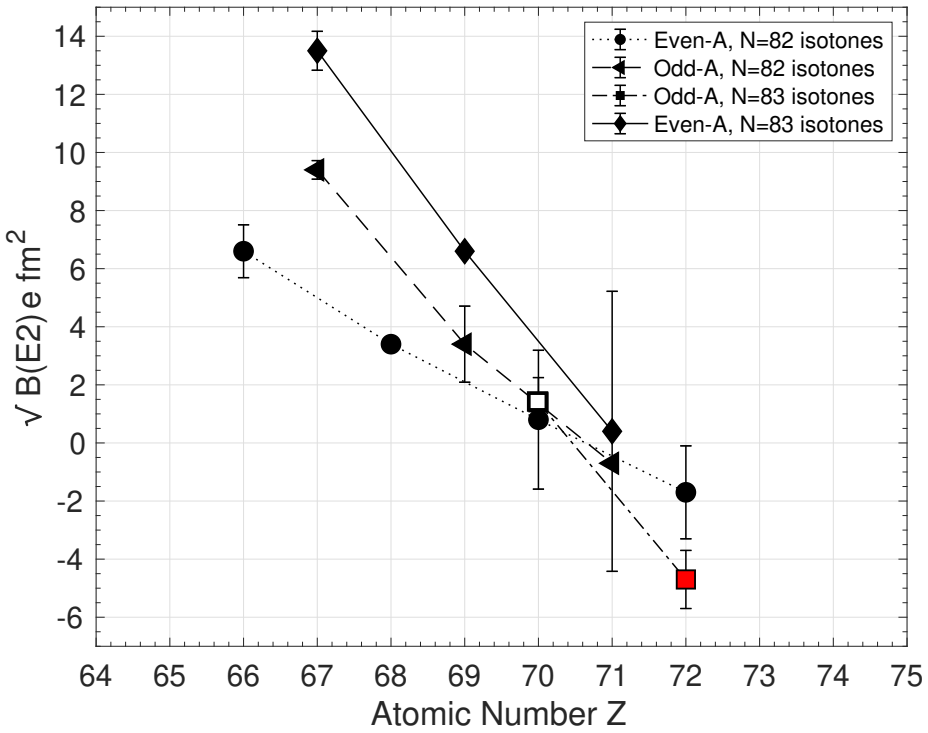

Fig. 4.18 The square root of $B(E2)$ values for even-A and odd-A isomeric transitions in $N = 82$ and $N = 83$ isotones are plotted as a function of atomic number.[1, 62, 64, 75, 76]. The red point represent the value calculated by this work for ^{155}Hf.

The filling of the $h_{11/2}$ subshell is responsible for the parabolic behaviour of $B(E2)$, which can be seen in figure(4.19), as function of Z for $N = 83$ isotones. However, for $N = 82$ isotones the data points do not provide much information regarding the filling of the $h_{11/2}$ subshell, particularly since the value for ^{154}Hf is only a limit without a precise determination of its energy. The fact that the ^{153}Yb value is an estimate meant that there remained a degree of uncertainty about the minimum in the plot for $N = 83$. The new data point for ^{155}Hf determined in this thesis confirms that there is indeed a minimum close to $Z = 71$. This hindrance makes the lifetimes around $Z = 71$ quite long. In this case, seniority isomerism serves as a stabilization mechanism. The values of the reduced $E2$ transition strengths have been obtained for proton-rich $N = 82$ isotones in a study of $Z = 64$ core stiffness within a shell-model framework [77]. The measured values are in good agreement with the theoretical calculations, which motivates extending the study to even heavier $N = 83$ isotones.

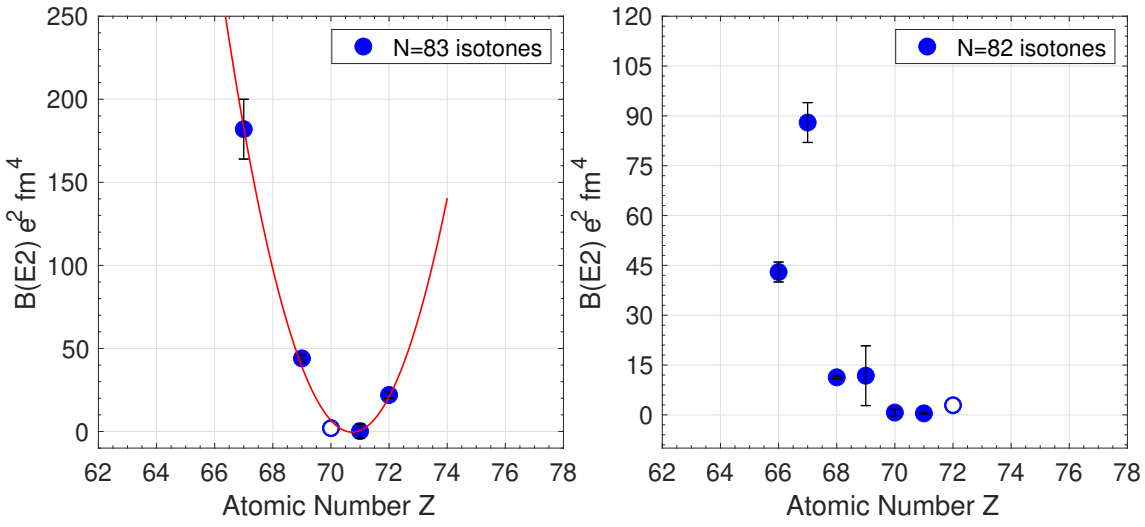

Fig. 4.19 The measured $B(E2)$ values for the isomeric transitions in $N = 82$ and $N = 83$ isotones are plotted as a function of the atomic number [1, 62, 64, 75, 76]. Hollow data points represent estimated values.

4.2.6 Systematic analysis of low-lying states across N = 83 isotones

It is possible to draw conclusions regarding the evolution of single-particle structures approaching the proton drip line through the analysis of the structure of odd A isotones ($N = 83$)

below $Z = 72$. The systematic study is conducted with four nuclei starting at ^{147}Gd $(Z = 64)$ up to ^{153}Yb $(Z = 70)$. Figure (4.20) displays the systematic excitation energy of most of the common levels among the isotones [78, 58, 74, 1]. The relatively constant excitation energies of states associated with the $\pi {h_{11/2}}^n \otimes \nu f_{7/2}$ configuration with increasing Z reflect the neutron dominance of single-particle structures as well as a very limited interaction between the $f_{7/2}$ neutrons and the $h_{11/2}$ protons.

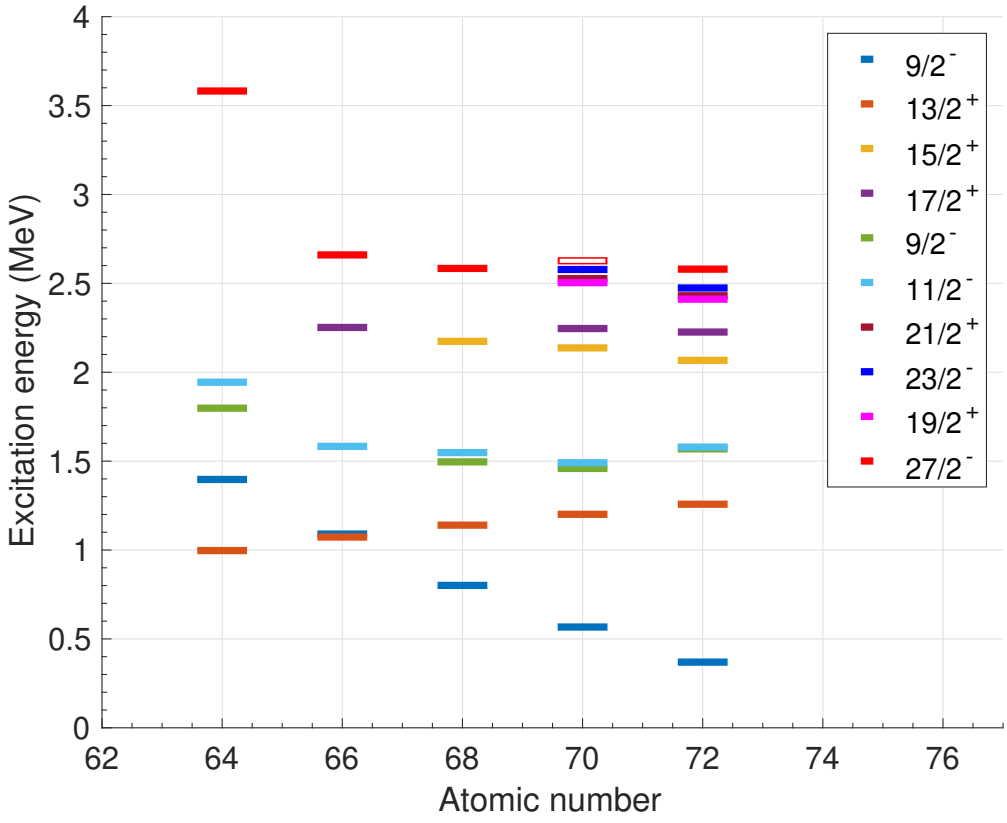

Fig. 4.20 Neutron single-particle states systematic in odd-A $N = 83$ isotones for Z from 64 up to 72. The data have been collected from [1, 58, 74, 78]. The data at $Z = 72$ are derived from this study. Hollow data points represent estimated values for the $27/2^-$ state in ^{153}Yb.

The reduction in energy of the $9/2^-$ state, in the $\pi {h_{11/2}}^n \otimes \nu h_{9/2}$ configuration, with increasing Z is directly related to the presence of additional protons into the system. Due to the fact that no proton pairs are broken to achieve this state, an interaction between the $9/2^-$ neutron and the $h_{11/2}$ protons is an appropriate mechanism to explain this lowering of excitation energy. A $\pi {h_{11/2}}^n \otimes \nu h_{9/2}$ interaction is proposed to explain the reduction of the states

energies in $N = 83$ isotones [66] and this interpretation has been adopted for $N = 84$ isotones [79, 80] to account for the lowering of the $25/2^-$ state as well. Figure (4.21) illustrates the decrease of the energy gap between the ground state and the $9/2^-$ with increasing the atomic number. Systematics of odd-A, $N = 85$ isotones above $Z = 64$ show the same behavior as in $N = 83$ isotones. A plot of the excitation energies of the $9/2$ state as a function of proton number is presented in figure (4.22). Since the wave functions of the $h_{9/2}$ neutron and the $h_{11/2}$ protons overlap, there is a strong interaction between them [81]. As the number of protons increases, this interaction becomes more likely.

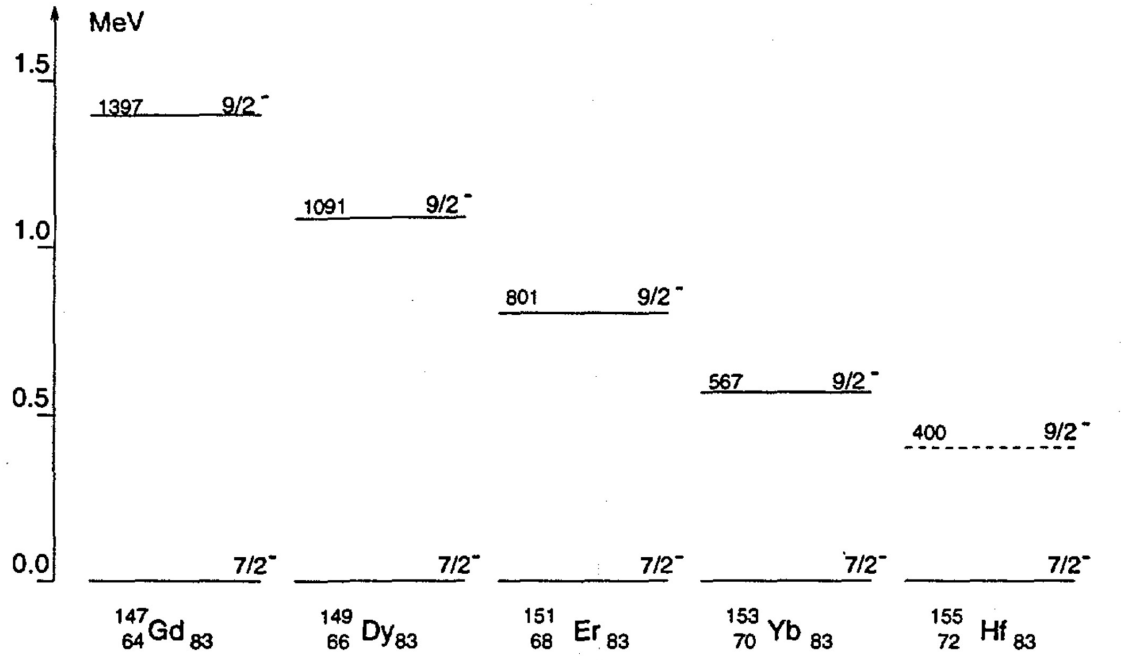

Fig. 4.21 Neutron single-particle state systematic of $9/2^-$ level in odd-A $N = 83$ isotones. The figure is taken from reference [66], where an extrapolation was made to the ^{155}Hf state.

4.2.7 Excited states above the isomer

The additional selectivity provided by the decay of the isomer allowed the study of transitions above the isomer. Gamma-ray spectroscopy at the focal plane allows us to place transitions

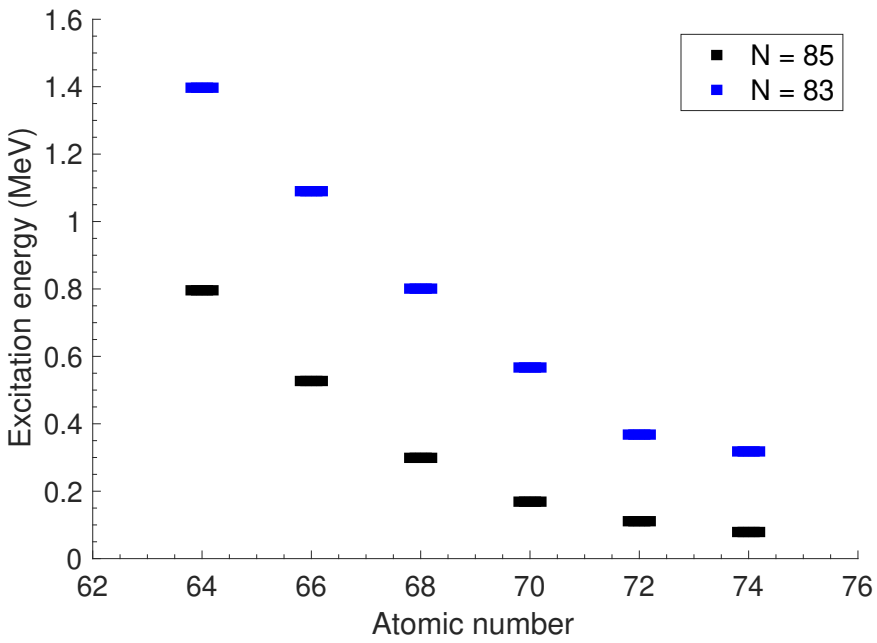

Fig. 4.22 Systematics of energy levels odd-A built upon $9/2^-$ in $N = 83$ and $N = 85$ isotones above $Z = 64$ in blue and black, respectively. Data other than ^{155}Hf are taken from references [1, 58, 74, 78, 65, 82, 83, 84, 85, 86, 87].

below the isomer at lower excitation energies. By tagging these gamma-ray transitions, it is possible to study the structure above the isomer using prompt gamma rays detected at the target position.

Figure (4.23.A) shows the energy spectrum measured by Jurogam array obtained by collecting gamma rays associated with recoils followed by alpha decay within a time window of up to 4.5 seconds. Most of the strong peaks are associated with ^{156}Lu and a few are associated with the decay of excited states in ^{158}Lu previously studied in [35]. Specifying the correlation to the alpha decay from the ground state in ^{155}Lu reduces the counts in the observed spectrum by a significant amount. This gamma-ray spectrum is shown in figure (4.23.B). In addition to the highly intense gamma peaks from ^{156}Lu, the three peaks representing the decay of the excited states feeding the $11/2^-$ state in ^{155}Lu namely $807, 685$ and $329\ keV$ are also visible in the spectrum [44]. Two spectra were produced using the characteristic half-life and energy of alpha decay for the gamma transitions in ^{156}Lu and ^{155}Lu in order to remove these peaks from the spectrum. Before the subtraction, the ^{156}Lu gamma spectrum has been normalised

Table 4.3 Energies and efficiency corrected relative intensities of gamma-ray transitions feeding the exited state detected at the focal plane below the $27/2^-$ ^{155}Hf isomer. Energies are accurate to $\pm 0.5 keV$.

Energy (keV)	Peak Area	Intensity
190.0	286 (47)	24.4 (4)
217.1	340 (36)	31.5 (3)
269.9	66 (26)	6.5 (3)
412.9	217 (48)	27.7 (6)
569.2	682 (67)	100 (10)
620.3	130 (36)	22.3 (6)
684.7	213 (39)	34.7 (6)
1305.8	319 (37)	67.9 (8)
1397.5	66 (18)	14.3 (4)
1749.4	23 (5)	6.2 (1)

to 313 keV peak in figure (4.23.B) while the ^{155}Lu spectrum is normalised to 807 keV peak. Despite the subtraction, it was not possible to determine whether there are any transitions from ^{155}Hf, as the background was not sufficiently removed.

To overcome this problem, an additional condition has been added to the sorting code. This is that the gamma rays detected by the Jurogam array must coincide with those from the ^{155}Hf isomer detected by the germanium detectors at the focal plane of MARA. Figure (4.23.C) presents the resulting spectrum. In the figure, new unidentified peaks can be seen at $217, 412, 570$ and 1306 keV along with less intense peaks from ^{156}Lu and ^{155}Lu. These transitions are tentatively assigned as gamma rays populating the $27/2^-$ isomer in ^{155}Hf. A gamma-gamma coincidence analysis was not possible due to low statistics. The energy and relative intensity values of the identified transitions are listed in table (4.3). Based on equation (3.10) and the coefficient from figure (3.27), the relative intensity of these transitions has been corrected for the Jurogam array efficiency. It is instructive to bear in mind that the yield of ^{153}Yb isomer decays observed in this work was substantially larger than that for ^{155}Hf factor of three, so this gives an indication of how challenging it will be to identify excited states above the isomer in ^{155}Hf.

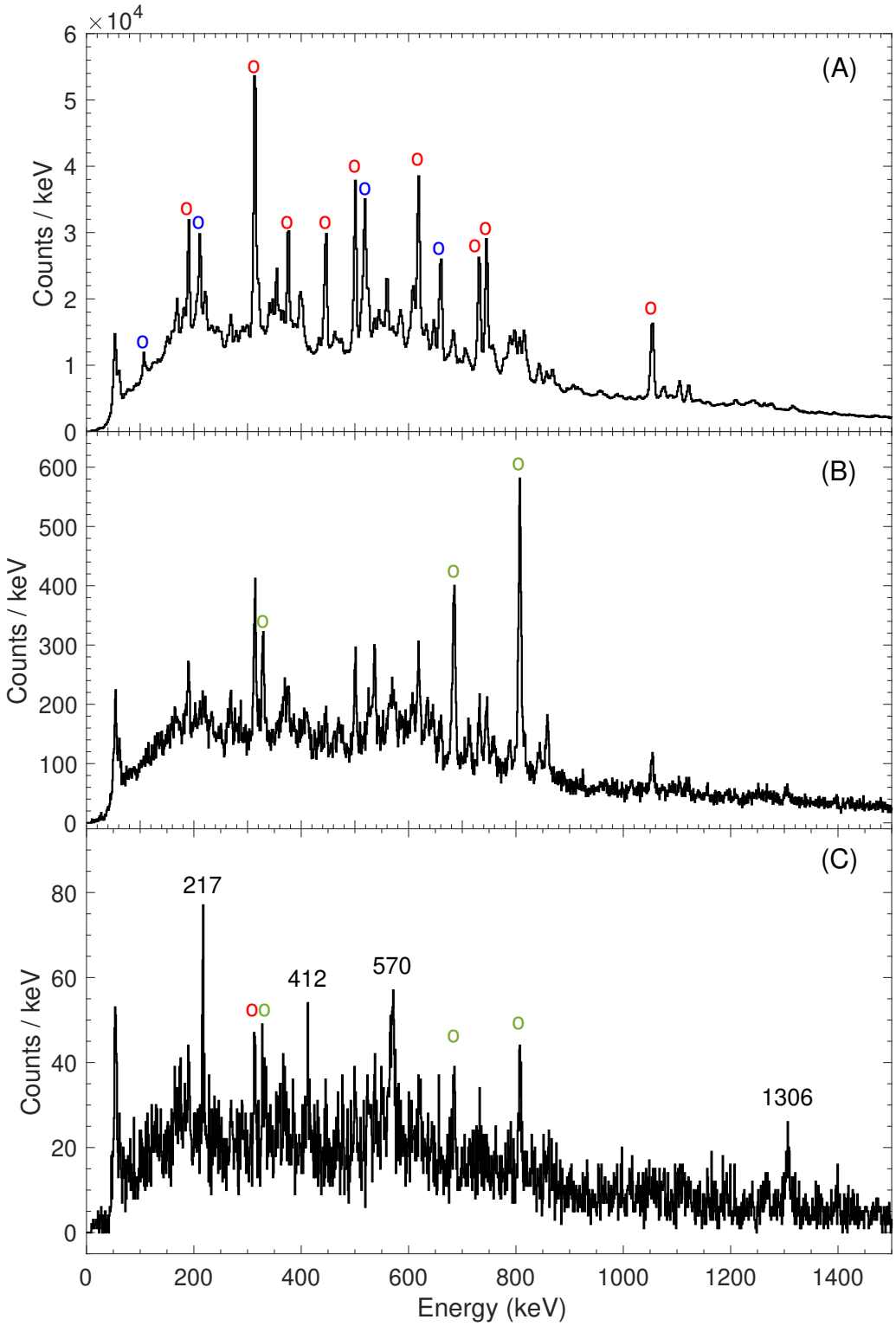

Fig. 4.23 Jurogam gamma-ray spectrum. (A) Pre-filtered spectrum of all gamma-ray data in Jurogam corresponding to any focal plane signal. We can see emission from the strongest reaction channels; red circles correspond to transitions in ^{156}Lu, blue circles to ^{158}Lu, and green circles to ^{155}Lu. (B) Recoil-alpha gated spectrum using the ^{155}Lu 5655 keV alpha decay as a tag with a correlation time between 400 ms and 4.5 s. (C) RDT spectrum using the ^{155}Lu 5655 keV alpha decay as a tag that is correlated with delayed gamma detected in a focal-plane germanium detector.

Chapter 5

Conclusions and Future Work

In this work, excited states have been investigated in a neutron-deficient nucleus that lies near the proton drip line and has one neutron above the $N = 82$ shell closure. The nucleus has been produced, identified, and studied with greater detail than previously possible at the Accelerator Laboratory of the University of Jyväskylä, using a vacuum-mode separator MARA, Jurogam, and a focal plane spectrometer.

This thesis presents the results of spectroscopic measurements of isomeric decay in ^{155}Hf. A high-spin isomeric state with a half-life of $0.509(0.022)\ \mu s$, which exhibits gamma-ray decay, has been observed for the first time. The half-life has been used to calculate the $B(E2)$ reduced transition probability of the transition depopulating the isomeric state. The excitation energy of the isomer has been measured as $2764\ (4)\ keV$ and has been assigned $(27/2^-)$ spin and parity based on systematics, reduced decay width and Weisskopf estimate arguments. Gamma-ray transitions linking the $27/2^-$ isomer to the $7/2^-$ ground state have been observed. Electromagnetic decay paths were determined based on a gamma-ray coincidence analysis. The level scheme has been deduced and spins and parities have been assigned for the levels.

Generally, the spin-parity assignments have been guided by the level systematics for the $N = 83$ nuclei above ^{147}Gd. The ground state has been given $7/2^-$ spin and parity based on a single-particle level resulted from $\pi h^n{}_{11/2} \otimes \nu h_{7/2}$ configuration. Further contributions to the levels assignment are provided by the single-particle levels from the $\pi h_{11/2} \otimes \nu h_{9/2}$ and

$\pi h_{11/2} \otimes \nu i_{13/2}$ configurations. Moreover, the isomer populates the $21/2^+$ and $17/2^+$ states which result from the coupling of protons with spins 7^- and 5^- to the $f_{7/2}$ neutron state. It has been observed that all of these configurations exist in its isotones ^{153}Yb, ^{151}Er and ^{149}Dy [57, 88, 89]. Additionally, the systematics of the odd-A $N = 83$ isotones show that the energy of the $9/2^-$ state decreases with increasing Z. The trend appears to be continuing for ^{155}Hf. This lowering of the excitation energy is explained by the interaction between the $h_{9/2}$ neutron and $h_{11/2}$ protons, since no proton pairs are broken [1].

The 105.4 keV $(27/2^- \longrightarrow 23/2^-)$ isomeric transition was found to be consistent with an $E2$ multipolarity. The reduced $E2$ transition rate was measured to be equal to $0.44(4)$ $W.u.$, confirming that isomer decays in $N = 83$ isotones appear to follow a parabolic pattern with Z. Calculations based on the shell model assuming a closed proton subshell at $Z = 64$ produced $B(E2)$ values for $N = 82$ isotones that are consistent with the measured values [77, 90]. It has been argued in the literature that such calculations are insufficient and further work is required to extend those shell model calculations to ^{153}Yb and ^{155}Hf [77]. Performing shell model calculations is beyond the scope of this thesis.

The structure above the isomer has been examined utilizing the additional selectivity provided by the gamma rays produced from the decay of the isomer and the JYU Tube detector. Consequently, ten transitions were observed by Jurogam array. The low level of statistics, however, prevented a gamma-gamma coincidence analysis. It will therefore be necessary in the future to revisit this nucleus with enhanced levels of statistics for a coincidence analysis in order to investigate how the states above the isomer are arranged. This is particularly interesting now because gamma transitions above the isomer were detected in its nearest even-Z isotone ^{153}Yb. The structure above the isomer has also been confirmed by a separate experiment which produced significantly higher statistics [47]. This will provide an opportunity to examine how adding two proton affects the structure.

The production of proton-rich nuclei far from the stability valley near the proton drip line is expected to be extremely low, and the short half-lives will present additional experimental challenges. MARA contributed significantly to the production of these nuclei with low cross sections and to the investigation of their nuclear structure in the medium-heavy ($150 \leq$

A) region. MARA's capabilities are illustrated by recent discoveries of nuclei. Several proton-emitting nuclei, including ^{158}Re, ^{176}Tl, ^{169}Au, and ^{165}Ir, have been observed and the beta decaying nucleus ^{156}W, the lightest of the tungsten isotopes, was also discovered [91, 92, 93, 94]. Furthermore, newly alpha decaying nuclei such as ^{160}Os, $^{176_m}TI$, ^{165}Pt, and ^{170}Hg have been identified [9, 29, 92].

An additional development was carried out by installing the JYUTube inside the target chamber. In this way, contamination could be minimized so that the Xn channels could be studied more effectively. When combined with germanium detectors placed at the focal plane, the detection of gamma-ray emission from isomeric states could be enhanced, especially when the production channel is weak. Evidence of an isomer has already been found in ^{155}Ta, for example [91]. As for $N = 83$ isotones, ^{155}Hf is the heaviest nucleus known with a $27/2^-$ isomeric state. ^{156}Ta is expected to have a 17^+ isomeric state; however, no gamma transitions have been observed although about 110 events of a 9^+ proton decaying state have been detected in experiment B. Therefore, it is worth trying to study the isomeric transition in this region in the context of internal conversion electrons. A particular point to be noted is that isomeric transitions in ^{153}Yb and ^{154}Hf have not been observed and the strength of the reduced $B(E2)$ values has been estimated [57, 72]. Another candidate to investigate its structure is ^{157}W, however, this is expected to be a challenging case due to its low yield.

References

[1] McNeill, J., Chishti, A., Daly, P., Gelletly, W., Hotchkis, M., Piiparinen, M., Varley, B., Woods, P., and Blomqvist, J. (1993) Isomeric decay studies using a recoil mass separator. *Zeitschrift für Physik A Hadrons and Nuclei,* **344**(4), 369–379.

[2] Binding energy. https://www.britannica.com/science/atom/Nuclear-shell-model Accessed: 2022-08-27.

[3] Krane, K. S. (1991) Introductory nuclear physics, John Wiley & Sons, .

[4] Briscoe, A. D. The Discovery of the Alpha Emitter 160 Os, the Beta Emitter 156 W and an Electromagnetic Decay Branch from the 25/2- Spin Gap Isomer in 155 Lu PhD thesis The University of Liverpool (United Kingdom) (2021).

[5] Kibedi, T., Burrows, T., Trzhaskovskaya, M. B., Davidson, P. M., and Nestor Jr, C. W. (2008) Evaluation of theoretical conversion coefficients using BrIcc. *Nuclear Instruments and Methods in Physics Research Section A: Accelerators, Spectrometers, Detectors and Associated Equipment,* **589**(2), 202–229.

[6] Ziegler, J. F., Ziegler, M. D., and Biersack, J. P. (2010) SRIM–The stopping and range of ions in matter (2010). *Nuclear Instruments and Methods in Physics Research Section B: Beam Interactions with Materials and Atoms,* **268**(11-12), 1818–1823.

[7] Knoll, G. F. (2010) Radiation detection and measurement, John Wiley & Sons, .

[8] Sarén, J. (2011) The ion-optical design of the MARA recoil separator and absolute transmission measurements of the RITU gas-filled recoil separator,. *Research report/Department of Physics, University of Jyväskylä,* (7/2011).

[9] Sottili, L. (2018) Test of JYUTube as a veto detector at MARA for background suppression in nuclear spectroscopy beyond the proton drip line.

[10] Carroll, R., Page, R., Joss, D., O'Donnell, D., Uusitalo, J., Darby, I., Andgren, K., Auranen, K., Bönig, S., Cederwall, B., et al. (2016) Excited states in the proton-unbound nuclide Ta 158. *Physical Review C,* **93**(3), 034307.

[11] McPeake, C. G. (2017) Excited states in the exotic nuclei 156 Lu and 158 Lu, The University of Liverpool (United Kingdom), .

[12] McNeill, J., Chisti, A., Daly, P., Hotchkis, M., Piiparinen, M., and Varley, B. (1989) A 15 μs isomer in thez= 70n= 83 nucleus153Yb. *Zeitschrift für Physik A Atomic Nuclei,* **332**(1), 105–106.

[13] Daly, P., Kleinheinz, P., Broda, R., Lunardi, S., Backe, H., and Blomqvist, J. (1980) Protonh 2 11/2 and octupole excitations in148 66Dy82 and149 66Dy83. *Zeitschrift für Physik A Atoms and Nuclei,* **298**(3), 173–185.

[14] McNeill, J., Broda, R., Chung, Y., Daly, P., Grabowski, Z., Helppi, H., Kortelahti, M., Janssens, R., Khoo, T., Lawson, R., et al. (1986) Level structure of proton-richN= 83 Nuclei150Ho and152Tm. *Zeitschrift für Physik A Atomic Nuclei,* **325**(1), 27–35.

[15] Broda, R., Daly, P., McNeill, J., Janssens, R., and Radford, D. (1987) Level structure of 68 149 Er 81 and high-spin isomerism in proton-rich N= 81, 82, 83 nuclei. *Zeitschrift für Physik A Atomic Nuclei,* **327**, 403–408.

[16] Helppi, H., Chung, Y., Daly, P., Faber, S., Pakkanen, A., Ahmad, I., Chowdhury, P., Grabowski, Z., Khoo, T., Lawson, R., et al. (1982) Yrast (πh112) n excitations in proton-rich N= 82nuclei. *Physics Letters B,* **115**(1), 11–14.

[17] Akovali, Y., Toth, K., Goodman, A., Nitschke, J., Wilmarth, P., Moltz, D., Rao, M., and Sousa, D. (1990) Single-particle states in Tm 151 and Er 151: Systematics of neutron states in N= 83 nuclei. *Physical Review C,* **41**(3), 1126.

[18] Stefanini, A., Daly, P., Kleinheinz, P., Maier, M., and Wagner, R. (1976) Isomers in the N= 83 nucleus 149Dy. *Nuclear Physics A,* **258**(1), 34–42.

[19] Komppa, T., Komu, R., Kortelahti, M., Muhonen, J., Pakkanen, A., Piiparinen, M., Prochazka, I., and Blomqvist, J. (1983) Medium-spin levels in the N= 83 nucleus147Gd. *Zeitschrift für Physik A Atoms and Nuclei,* **314**(1), 33–42.

[20] Seweryniak, D., Ahmad, H., and Amro, D., First in-beam observation of excited states in 156 72 Hf 84 using the recoul-decay tagging method. Technical report, Argonne National Lab. (1996).

[21] Lewis, M., Parr, E., Page, R., McPeake, C., Joss, D., Ali, F., Auranen, K., Briscoe, A., Capponi, L., Grahn, T., et al. (2018) Decay of a 19- isomeric state in Lu 156. *Physical Review C,* **98**(2), 024302.

[22] Nuclear chart. https://www.nndc.bnl.gov/ Accessed: 2022-08-21.

[23] Haxel, O., Jensen, J. H. D., and Suess, H. E. (1949) On the" magic numbers" in nuclear structure. *Physical Review,* **75**(11), 1766.

[24] Montet, G. L., Keller, S. P., and Mayer, J. E. (1952) Interactions of Closed Shell Ions. *The Journal of Chemical Physics,* **20**(7), 1057–1063.

[25] Mayer, M. G. (1949) On closed shells in nuclei. II. *Physical Review,* **75**(12), 1969.

[26] Mayer, M. G. (1948) On closed shells in nuclei. *Physical Review,* **74**(3), 235.

[27] Mayer, M. G. (1950) Nuclear configurations in the spin-orbit coupling model. i. empirical evidence. *Physical Review,* **78**(1), 16.

[28] Nilsson, S. G. and Ragnarsson, I. (1995) Shapes and Shells in Nuclear Physics, Cambridge University Press, .

[29] Casten, R. and Casten, R. F. (2000) Nuclear structure from a simple perspective, Vol. 23, Oxford University Press on Demand, .

[30] Huang, W. and Audi, G. (2017) Corrections of alpha-and proton-decay energies in implantation experiments. In *EPJ Web of Conferences* EDP Sciences Vol. 146, p. 10007.

[31] Giovinazzo, J., Blank, B., Chartier, M., Czajkowski, S., Fleury, A., Jimenez, M. L., Pravikoff, M., Thomas, J.-C., de Oliveira Santos, F., Lewitowicz, M., et al. (2002) Two-Proton Radioactivity of F 45 e. *Physical review letters,* **89**(10), 102501.

[32] JM, B. latt and VF W eissk o ρ f, Theoretical Nuclear Physics, Chapt VIII. (1952).

[33] Schoetzig, U. and Schrader, H. (1998) Half-life measurements and photon emission probabilities of frequently applied radioisotopes; Halbwertszeiten und Photonen-Emissionswahrscheinlichkeiten von haeufig verwendeten Radionukliden.

[34] Schrader, H. (2000) Calibration and consistency of results of an ionization-chamber secondary standard measuring system for activity. *Applied Radiation and Isotopes,* **52**(3), 325–334.

[35] Segre, E. and Helmholz, A. (1949) Nuclear isomerism. *Reviews of Modern Physics,* **21**(2), 271.

[36] Walker, P. M. and Podolyak, Z. (2022) Nuclear isomers. In *Handbook of Nuclear Physics* pp. 1–37 Springer.

[37] Bethe, H. and Ashkin, J. (1953) The passage of heavy particles through matter. *Experimental nuclear physics,* **1**, 166–201.

[38] Hodgson, P. E. (1978) Nuclear heavy-ion reactions. *La Rivista del Nuovo Cimento (1978-1999),* **1**(1), 1–56.

[39] Accelerators and ion sources,. https://www.jyu.fi/science/en/physics/research/infrastructures/accelerator-laboratory/accelerators-and-ion-sources Accessed: 2022-07-04.

[40] Recoil separators,. https://www.jyu.fi/science/en/physics/research/infrastructures/accelerator-laboratory/nuclear-physics-facilities/recoil-separators Accessed: 2022-02-24.

[41] MARA vacuum mode recoil separator,. https://www-jyu-fi.translate.goog/science/en/physics/research/infrastructures/accelerator-laboratory/nuclear-physics-facilities/recoil-separators/mara-mass-analysing-recoil-apparatus?_x_tr_sl=en&_x_tr_tl=ar&_x_tr_hl=ar&_x_tr_pto=op,sc Accessed: 2022-02-10.

[42] Hilton, J., Uusitalo, J., Sarén, J., Page, R., Joss, D., AlAqeel, M., Badran, H., Briscoe, A., Calverley, T., Cox, D., et al. (2019) α-spectroscopy studies of the new nuclides Pt 165 and Hg 170. *Physical Review C,* **100**(1), 014305.

[43] Gilmore, G. (2008) Practical gamma-ray spectroscopy, John Wiley & Sons, .

[44] Micron Semiconductor Ltd,BB20 DSSD Specifications,. http://www.micronsemiconductor.co.uk/product/bb20/ Accessed: 2021-03-20.

[45] Beausang, C. and Simpson, J. (1996) Large arrays of escape suppressed spectrometers for nuclear structure experiments. *Journal of Physics G: Nuclear and Particle Physics,* **22**(5), 527.

[46] Page, R., Andreyev, A., Appelbe, D., Butler, P., Freeman, S., Greenlees, P., Herzberg, R.-D., Jenkins, D., Jones, G., Jones, P., et al. (2003) The GREAT spectrometer. *Nuclear Instruments and Methods in Physics Research Section B: Beam Interactions with Materials and Atoms,* **204**, 634–637.

[47] mirion,Clover detector super spec. https://mirion.s3.amazonaws.com/cms4_mirion/files/pdf/spec-sheets/c39840_clover_detector_super_spec_3.pdf?1557861105 Accessed: 2021-09-14.

[48] Bege Detector. https:https://mirion.s3.amazonaws.com/cms4_mirion/files/pdf/spec-sheets/ops-1424_bege_spec_sheet.pdf?1579456901 Accessed: 2022-08-20.

[49] Zeng, Z., Mi, Y.-H., Zeng, M., Ma, H., Yue, Q., Cheng, J.-P., Li, J.-L., Qiu, R., and Zhang, H. (2016) Characterization study of a broad-energy germanium detector at CJPL. *arXiv preprint arXiv:1603.01782,*.

[50] Eljen Technology,Plastic-scintillators,. https://eljentechnology.com/products/plastic-scintillators/ej-200-ej-204-ej-208-ej-212 Accessed: 2021-07-23.

[51] Rahkila, P. (2008) Grain—A java data analysis system for total data readout. *Nuclear Instruments and Methods in Physics Research Section A: Accelerators, Spectrometers, Detectors and Associated Equipment,* **595**(3), 637–642.

[52] Lazarus, I., Appelbe, E., Butler, P., Coleman-Smith, P., Cresswell, J., Freeman, S., Herzberg, R., Hibbert, I., Joss, D., Letts, S., et al. (2001) The GREAT triggerless total data readout method. *IEEE Transactions on Nuclear Science,* **48**(3), 567–569.

[53] ROOT: analyzing petabytes of data, scientifically.. https://root.cern Accessed: 2021-08-27.

[54] Paul, E., Woods, P., Davinson, T., Page, R., Sellin, P., Beausang, C., Clark, R., Cunningham, R., Forbes, S., Fossan, D., et al. (1995) In-beam γ-ray spectroscopy above Sn 100 using the new technique of recoil decay tagging. *Physical Review C,* **51**(1), 78.

[55] Kortelahti, M., Toth, K., Vierinen, K., Nitschke, J., Wilmarth, P., Firestone, R., Chasteler, R., and Shihab-Eldin, A. (1989) Decay properties of Yb 153 and Tm 153; Excitation energies of the s 1/2 and h 1 1/2 proton states in Tm 153. *Physical Review C,* **39**(2), 636.

[56] Wilmarth, P., Nitschke, J., Vierinen, K., Toth, K., and Kortelahti, M. (1988) Beta-delayed proton decay of theN= 83 precursor153Yb. *Zeitschrift für Physik A Atomic Nuclei,* **329**(4), 503–504.

[57] David O'Donnell, Private communication. https://orcid.org/0000-0002-4710-3803.

[58] Rytz, A. (1991) Recommended energy and intensity values of alpha particles from radioactive decay. *Atomic Data and Nuclear Data Tables,* **47**(2), 205–239.

[59] Trzaska, W. (1990) Recommended data on selected gamma-ray and conversion-electron calibration sources. *Nuclear Instruments and Methods in Physics Research Section A: Accelerators, Spectrometers, Detectors and Associated Equipment,* **297**(1-2), 223–229.

[60] Page, R., Woods, P., Cunningham, R., Davinson, T., Davis, N., James, A., Livingston, K., Sellin, P., and Shotter, A. (1996) Radioactivity of neutron deficient isotopes in the region N> 82> Z. *Physical Review C,* **53**(2), 660.

[61] Yoshizawa, Y., Iwata, Y., and Iinuma, Y. (1980) Precision measurements of gamma-ray intensities. II. 152Eu, 154Eu and 192Ir. *Nuclear Instruments and Methods,* **174**(1-2), 133–139.

[62] Kim, I., Park, C., and Choi, H. (2003) Absolute calibration of 60Co by using sum-peak method and an HPGe detector. *Applied Radiation and Isotopes,* **58**(2), 227–233.

[63] Brinkman, G. and Aten Jr, A. (1963) Absolute standardization with a NaI (Tl) crystal—III: Calibration of β+-emitters. *The International Journal of Applied Radiation and Isotopes,* **14**(10), 503–510.

[64] Agostinelli, S., Allison, J., Amako, K. a., Apostolakis, J., Araujo, H., Arce, P., Asai, M., Axen, D., Banerjee, S., Barrand, G., et al. (2003) GEANT4—a simulation toolkit. *Nuclear instruments and methods in physics research section A: Accelerators, Spectrometers, Detectors and Associated Equipment,* **506**(3), 250–303.

[65] Radford, D. RadWare: A Software Package for Interactive Graphical Analysis of Gamma-ray Coincidence Data.,. https://radware.phy.ornl.gov/gf3/#3.40. Accessed: 2022-010-31.

[66] Barden, R., Gabelmann, H., Grant, I., Kirchner, R., Klepper, O., Nyman, G., Plochocki, A., Rathke, G.-E., Roeckl, E., Rykaczewski, R., et al. (1988) Gamow-Teller beta decay of even nuclides near 100 Sn. In *Nuclear Structure of the Zirconium Region* pp. 403–408 Springer.

[67] Dracoulis, G., Walker, P., and Kondev, F. (2016) Review of metastable states in heavy nuclei. *Reports on Progress in Physics,* **79**(7), 076301.

[68] Kleinheinz, P., Broda, R., Daly, P., Lunardi, S., Ogawa, M., and Blomqvist, J. (1979) Particle hole yrast states in146Gd and147Gd and the Z= 64 shell closure. *Zeitschrift für Physik A Atoms and Nuclei,* **290**(3), 279–295.

[69] Häusser, O., Mahnke, H., Alexander, T., Andrews, H., Sharpey-Schafer, J., Swanson, M., Ward, D., Taras, P., and Keinonen, J. (1982) Quadrupole moments of yrast isomers in 144, 147, 148Gd. *Nuclear Physics A,* **379**(2), 287–312.

[70] Ding, K., Cizewski, J., Seweryniak, D., Amro, H., Carpenter, M., Davids, C., Fotiades, N., Janssens, R., Lauritsen, T., Lister, C., et al. (2001) Excited states in 155 Yb and 1 5 5, 1 5 6, 1 5 7 Lu from recoil-decay tagging. *Physical Review C,* **64**(3), 034315.

[71] Thompson, A. C., Vaughan, D., et al. (2001) X-ray data booklet, Vol. 8, Lawrence Berkeley National Laboratory, University of California Berkeley, CA, .

[72] Apaydın, G., Aylıkcı, V., Cengiz, E., Kaya, N., Kobya, Y., and Tıraşoğlu, E. (2008) Determination of K shell X-ray intensity ratios for some heavy elements. *Radiation Physics and Chemistry,* **77**(8), 923–927.

[73] Stefanini, A., Kleinheinz, P., and Maier, M. (1976) A 500 ms three-particle isomer in 14966Dy83. *Physics Letters B,* **62**(4), 405–406.

[74] Jastrzbski, J., Kossakowski, R., Łukasiak, J., Moszyński, M., Preibisz, Z., André, S., Genevey, J., Gizon, A., and Gizon, J. (1980) Unambiguous identification and properties of high spin isomers in nuclei close to N= 82. *Physics Letters B,* **97**(1), 50–54.

[75] McNeill, J., Blomqvist, J., Chishti, A., Daly, P., Gelletly, W., Hotchkis, M., Piiparinen, M., Varley, B., and Woods, P. (1990) A 35 μs isomer in the exoticN= 83 Nucleus154Lu. *Zeitschrift für Physik A Atomic Nuclei,* **335**(2), 241–242.

[76] McNeill, J., Blomqvist, J., Chishti, A., Daly, P., Gelletly, W., Hotchkis, M. A., Piiparinen, M., Varley, B., and Woods, P. (1989) Exotic N= 82 nuclei sup 153 Lu and sup 154 Hf and filling of the. pi. h sub 11/2 subshell. *Physical Review Letters;(USA),* **63**(8).

[77] Barden, R., Plochocki, A., Schardt, D., Rubio, B., Ogawa, M., Kleinheinz, P., Kirchner, R., Klepper, O., and Blomqvist, J. (1988) Beta-decay of 27/2- isomers inN= 83 nuclei. *Zeitschrift für Physik A Atomic Nuclei,* **329**(1), 11–20.

[78] Matsuzawa, T., Nakada, H., Ogawa, K., and Momoki, G. (2000) Seniority isomerism in proton-rich N= 82 isotones and its indication to stiffness of the Z= 64 core. *Physical Review C,* **62**(5), 054304.

[79] Zhang, C., Kleinheinz, P., Piiparinen, M., Collatz, R., Lönnroth, T., Sletten, G., and Blomqvist, J. (1994) Shell model high-spin states in 67 151 Ho84. *Zeitschrift für Physik A Hadrons and Nuclei,* **348**(1), 65–66.

[80] Zhang, C., Kleinheinz, P., Piiparinen, M., Collatz, R., Lönnroth, T., Sletten, G., and Blomqvist, J. (1994) Seniority inverted yrast states observed in 69 153 Tm84. *Zeitschrift für Physik A Hadrons and Nuclei,* **348**(4), 249–250.

[81] Federman, P. and Pittel, S. (1979) Unified shell-model description of nuclear deformation. *Physical Review C,* **20**(2), 820.

[82] Piiparinen, M., Pengo, R., Nagai, Y., Hammarén, E., Kleinheinz, P., Roy, N., Carlén, L., Ryde, H., Lindblad, T., Johnson, A., et al. (1981) High spin shell model excitations in149Gd. *Zeitschrift für Physik A Atoms and Nuclei,* **300**(2), 133–142.

[83] Sapple, P., Page, R., Joss, D., Bianco, L., Grahn, T., Pakarinen, J., Thomson, J., Simpson, J., O'Donnell, D., Ertürk, S., et al. (2011) In-beam γ-ray spectroscopy of the N= 85 isotones 159 W and 160 Re. *Physical Review C,* **84**(5), 054303.

[84] Bianco, L., Page, R., Darby, I., Joss, D., Simpson, J., Al-Khalili, J., Cannon, A., Cederwall, B., Eeckhaudt, S., Ertürk, S., et al. (2010) Discovery of 157W and 161Os. *Physics Letters B,* **690**(1), 15–18.

[85] Piiparinen, M., Lunardi, S., Kleinheinz, P., Backe, H., and Blomqvist, J. (1979) High spin isomers in151Dy+. *Zeitschrift für Physik A Atoms and Nuclei,* **290**(3), 337–338.

[86] Carlén, L., Jonsson, S., Krumlinde, J., Lyttkens, J., Roy, N., Ryde, H., Strömberg, S., Waluś, W., Hagemann, G., and Herskind, B. (1982) High-spin states and yrast isomerism in 153Er. *Nuclear Physics A,* **381**(1), 155–172.

[87] Saad, A., Zhang, C., and Collatz, R., Shell model states in the 157 Hf 85 nucleons. Technical report, (1995).

[88] Foin, C., Gizon, A., Barnéoud, D., Genevey, J., Gizon, J., Santos, D., Farget, F., Paris, P., Liang, C., Bucurescu, D., et al. (2000) New investigation of the decay of the high-spin isomer in 151 Er. *The European Physical Journal A,* **8**, 451–454.

[89] Gupta, M., Das, P., Patel, S., Bhowmik, R., Werner, T., and Akovali, Y. (1996) Single-particle states in Dy 83 66 149 at high spin. *Physical Review C,* **54**(4), 1610.

[90] Wilson, J., Chung, Y., Faber, S., Pakkanen, A., Daly, P., Ahmad, I., Chowdhury, P., Khoo, T., Lawson, R., and Smither, R. (1981) Shell model yrast states of the N= 83 nucleus 150Ho. *Physics Letters B,* **103**(6), 413–416.

[91] Adam McCarter, Private communication. https://www.liverpool.ac.uk/physics/research/nuclear-physics/people/.

[92] Al-Aqeel, M. A. M. (2020) Decay Spectroscopy of the Thallium Isotopes 176,177 TL, The University of Liverpool (United Kingdom), .

[93] Hilton, J. B. (2019) Decays of new nuclides 169 Au, 170 Hg, 165 Pt and the ground state of 165 Ir discovered using MARA, The University of Liverpool (United Kingdom), .

[94] Andy Briscoe, Private communication. https://www.liverpool.ac.uk/physics/research/nuclear-physics/people/.